UNIVERSITY OF OKLAHOMA
GRADUATE COLLEGE

BACTERIOPHAGE-BASED BIOMATERIALS FOR MANIPULATING DERIVATION AND DIFFERENTIATION OF HUMAN INDUCED PLURIPOTENT STEM CELLS

A DISSERTATION
SUBMITTED TO THE GRADUATE FACULTY
in partial fulfillment of the requirements for the
Degree of
DOCTOR OF PHILOSOPHY

By
NINGYUN ZHOU
Norman, Oklahoma
2020

BACTERIOPHAGE-BASED BIOMATERIALS FOR MANIPULATING DERIVATION AND DIFFERENTIATION OF HUMAN INDUCED PLURIPOTENT STEM CELLS

A DISSERTATION APPROVED FOR THE
DEPARTMENT OF CHEMISTRY AND BIOCHEMISTRY

By THE COMMITTEE CONSISTING OF

Dr. Rakhi Rajan, Chair

Dr. Anthony W. Burgett

Dr. Randall S. Hewes

Dr. Si Wu

Acknowledgments

Perusing a Ph.D. is like climbing a mountain. Though it's full of twists and turns, I never regretted keeping climbing and felt happy about seeing the most beautiful sunrise at the top of the mountain. Along the road, many people have supported and encouraged me when I was suffering from failures and stresses.

I would like first to give thanks to my advisor Dr. Chuanbin Mao. Though he is not listed in the committee numbers due to his medical leave, I really appreciate his support and guidance. During my Ph.D. years, I learned how to think critically and work independently from him. He not only trained me experimental skills, but also taught me how to write scientific articles. I would never be what I am right now without his help.

My thanks would also go to my committee numbers: Dr. Rakhi Rajan, Dr. Anthony W. Burgett, Dr. Randall S. Hewes, and Dr. Si Wu. Thank you for your time and valuable suggestions both in my research and in my life. I would also express my appreciation to Dr. Wai Tak Yip, who gave me the chance to be a teaching assistant in my senior years and to Dr. Ronald L. Halterman, who gave me a lot of suggestions and guidance during Dr. Mao's leave.

I would also thank all the present and former members in Dr. Mao's lab, especially Dr. Yan Li, Dr. Penghe Qiu, and Dr. Binrui Cao, and the members in the Samuel Roberts Noble Microscopy Laboratory.

Finally, my appreciations go to my family, my fiancé, the girls' night team, and all my friends. Your understanding and encouragement played an important role in supporting me during this journey.

Table of Contents

List of Tables

List of Figures

Abstract

Induced pluripotent stem cells (iPSCs), which are derived from somatic cells, can differentiate into any cell type. They are promising tools in medical applications including regenerative medicine, personalized cell therapy, disease modeling, and drug discovery. The current stem cell research faces at least the following two major challenges: how to improve the reprogramming efficiency in iPSCs derivation; and how to control the differentiation of stem cells into certain cell types. The works in this dissertation attempt to find solutions to tackle the above two challenges.

To enhance the reprogramming efficiency of somatic cells into iPSCs (Chapter 2), human dermal fibroblasts (HDFs)-internalizing peptides were selected using Ph.D.™-12 Phage Display Peptide Library. After 3-4 rounds of the selection, 3 HDF-binding peptides with high occurrences were selected for further screening. Finally, the HDF-binding peptide with the strongest affinity and high specificity was chemically conjugated to the surface of a nanoparticle plasmid carrier to improve the endocytosis efficiency and further help with the reprogramming process.

To induce directional differentiation of iPSCs or iPSC-derived stem cells (Chapter 3), a novel 2D virus-based substrate with unique self-assembled hierarchical nano- and micro-topographies was developed. This substrate can direct the bidirectional differentiation of iPSC-derived neural progenitor cells (NPCs) into neurons and astrocytes without the use of costly growth

factors, which also provide a new approach for studying the interaction between neurons and astrocytes.

Chapter 1. Introduction

1.1 History and current research status of iPSCs

Human induced pluripotent stem cells (hiPSCs) and human embryonic stem cells (hESCs) are the most widely used pluripotent cells in tissue regeneration research. They have almost the same differentiation ability but derived from different origins. HiPSCs and hESCs are both pluripotent stem cells, which can divide continuously and have the potential to differentiate into any type of cells in the 3 germ layers.

1.1.1 History

The history of pluripotent stem cells was dated back to the 1960s, John Gurdon[1] transplanted a matured cell nucleus into a frog egg without nucleus and this new "combined" cell grew into a healthy tadpole (Figure 1). This famous experiment revealed a new concept that the fully specialized nucleus has the potential to grow into an entire organism under specific conditions. While the nuclear transfer let us understand the capability of a matured nucleus, it also limited further study due to the high technical skills required. In 1981, mouse embryonic stem cells (mESCs) were first generated by Evans et al.[2] and Martin[3]. They isolated mESCs from mouse embryo inner cell mass and managed to culture these cells in a dish. Later in 1998, human embryonic stem cells (hESCs) were successfully isolated by Thomson et al. [4] This work shed light on regenerative medicine with a potential problem that hESCs are extracted from human embryo, which have potential ethical issues. To solve this problem, two main solutions were developed by

scientists. The first solution was inspired by the cloning sheep Dolly with the nuclear transplantation method.[1, 5] Scentists use the sampe method to transferred the nucleus of a patient's somatic cell into an oocyte to generate more personalized stem cells. However, this method faces ethical issues because of the use of oocytes. The second solution was inspired by transcription factors. In 1987, Schneuwly et al.[6] found that ectopically expressed Antennapedia, a drosophila transcription factor, induced leg formation instead of antennae. This inspired us that some transcription factors had the ability to tune the stem cell fate. Another research group also showed that transcription factor MyoD converted fibroblasts into myocytes.[7] Later in the ESCs studies, Smith et al. found leukemia inhibitory factor (LIF) helped mouse ESCs maintain a pluripotent stage.[8] In 2006, Takahashi et al. [9] managed to transfer mouse fibroblasts into mouse induced pluripotent stem cells (miPSCs) by co-expression of four reprogramming factors: OCT4, SOX2, KLF4, and c-Myc. This discovery aroused worldwide attention in cell reprogramming. The following studies in the field successfully converted the human fibroblasts into human induced pluripotent stem cells (hiPSCs) using the above four reprogramming factors[10]. IPSCs are very similar to ESCs. They expressed almost the same genes as ESCs and could differentiate into 3 germ layers. However, there was no research reported that scientist can inject iPSCs into mouse blastocysts to create a new born mouse.[11] The discovery of hiPSCs is a milestone in tissue engineering field. It allows us to explore the possibility of getting any type of cells we want without ethical issues.

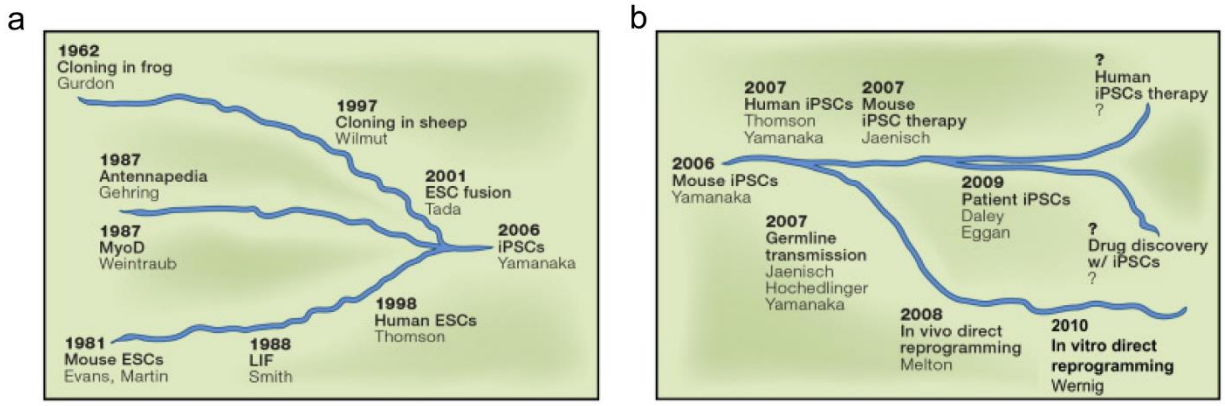

Figure 1. History of iPSCs derivation and current status.[11] (From "Induced pluripotent stem cells: past, present, and future." by Yamanaka, S., 2012, *Cell Stem Cell***,** *10* (6), 678-684.Copyright by 2020 Elsevier)

1.1.2 Current status

In addition to the challenge described above, another major problem in the current pluripotent stem cell research is whether hiPSCs are functionally and genetically equivalent to ESCs? Investigations were conducted by comparing both the gene expression and functionality of these two types of cells. Human iPSCs and hESCs are highly alike in gene expression, including global gene expression, DNA methylation, and transcriptome analyses. However, there are some studies that reported that reprogrammed hiPSCs have a greater chance in genomic mutation compared to hESCs[12]. Though both hiPSCs and hESCs could differentiate into cells in the three layers, some researches claim that hESCs are more efficient in differentiation.[13, 14]

Though hiPSCS has a lower differentiation efficiency, they are easy to access, free of ethical issues and can be used in drug testing or patient-specific treatment with a low immune response risk in transplantation. When clinical transplantation is needed, there is a very limited chance to get a good match to use hESCs. Human iPSCs were developed from patient mature cells, which can avoid the immune response. The animal model of anemia has been successfully cured by using the skin cell derived iPSCs by gene editing to repair the single point mutation.[15] HiPSCs also shed light to the treatment of degenerative diseases, which were always diagnosed in a very late stage. The patient-derived hiPSCs can help us to diagnose diseases at an early stage.[16]

As new information became available for iPSCs, we realized that iPSCs have huge potential in medical applications (Figure 1.1) including regenerative medicine, personalized cell therapy, disease modeling and drug discovery,[16] especially in neurogenic disease.[16, 17] Neurons are the type of cells that cannot reproduce. Once the neurons are damaged or lost, the chance of repairing the nerve damage is very little. Thus, there is a pressing need in developing neuron repairing strategy. IPSCs, a new cell source containing all the genetic material from the patients, not only can help us study the pathology of neurogenic disease but also shed lights to the neurogenic disease treatment.

1.2 Reprogramming of somatic cells into iPSCs

The most common classification of the iPSC derivation method is based on whether the external genes can be integrated into the genome of targeting cells. If the method involves the change of host chromosome by inserting the reprogramming genes, it's called integrating reprogramming. Otherwise, it's non-integrating reprogramming. The advantage of integrating method is that it has a higher reprogramming efficiency and long-lasting effect compared to the non-integrating method. The drawback is that there is a higher chance that it would interrupt the genome integrity and activate oncogenes.[18] For non-integrating method, it's more environment friendly, because it would not change the information of genome, but it suffers from a lower reprogramming efficiency. In non-integrating reprogramming process, a large amount of the external reprogramming factors goes into the cytoplasm. With the cell division going on, the copies of these reprogramming factors would keep decreasing in the daughter cells and will eventually lose the reprogramming information.

Instead of integrating and non-integrating methods in iPSC generation, we will discuss the reprogramming methods based on viral and non-viral methods. The viral method usually involves the use of exogenous gene packed into viral particles. The original virus DNA plays the leading role in reprogramming process and arranges virus packaging. It involves less manual work, but it's more expensive and always has the risk of re-activate oncogenes. Though the non-viral method is laborious, it's easier to control and has less tumor generation effects. In the non-viral method, there are several important steps that need to be taken care of separately, such as endocytosis,

endosome escape, entry into the nucleus, transcription, and translation.[19] In each step, we can improve the gene delivery efficiency by adding different chemicals or nanoparticles. In the following chapter, we emphasize on the nanotechnologies in non-viral reprogramming method, which contributes to improvements .

1.2.1 Viral vectors for cell reprogramming

Viral particles consist of two important parts: capsid proteins and nucleic acid. For the infectious viruses, it may also contain an envelop structure, which includes lipids and glycoproteins from the host cells. The advantage of viral vectors is that they usually have a strong promoter which can maximize the transgene expression in the host cells. The disadvantage of viral vectors is it may damage the host cells. Thus, in the viral gene editing system, the viral genes are partially deleted to control the toxicity on the host cells.[20] A few example of the common viral vectors are described below.

Retrovirus

Retrovirus is one of the most widely used integrative viral vectors in cell reprogramming. Yamanaka's group used it to deliver the four reprogramming genes (*OCT4, SOX2, KLF4*, and *c-Myc*) into somatic cells and successfully generated iPSCs.[9] Retrovirus vector can be used to deliver large inserts with high efficiency. The inserted reprogramming genes are usually been naturally silenced by the generated iPSCs later.[21] However, there are cases showing that the c-Myc gene

was re-activated after the silencing which caused tumor formation in the iPSC derivation process[22] and it can only infect the dividing cells.[23,24]

Lentivirus

Lentivirus can infect both dividing cells and non-dividing cells, which benefits a larger group of somatic cells for reprogramming. The insertion site for lentivirus is random. This may affect the gene integration on the host cell chromosome and has a potential risk in activating the oncogenes. It has been reported that the lentivirus method has a lower tumor genesis rate,[25] but sacrificed the reprogramming efficiency compared to retroviral method. [26]

Adenovirus

Adenovirus vector involved gene delivery is a non-integrating gene delivery method. The advantages for using adenoviruses are that they can infect both dividing and non-dividing cells, don't interupt the host genome and can stay in the episomal format after infection.[23, 24, 27] On the other hand, adenovirus can initiate strong immune responses in human body,[27] and has a lower reprogramming efficiency compared to the integrating virus vectors.[23] Adenovirus would be better used in *in vitro* model rather than *in vivo* model for gene delivery.

Sendai Virus

Sendai virus is also a non-integrating virus, which exists in the cytoplasm for the whole life circle. It has a high infection rate and a high exogenous gene expression level. Sendai virus is originated from rodents. Therefore, they are less toxic to humans.[28] Compared to adenovirus, Sendai virus takes less time to infect the host cells and can quickly reach to a maximum gene transduction level.[29] However, the adjustment of exogenous gene expression after Sendai virus transduction is not very easy and it might need multiple constructions to achieve the controllable reprogramming.[30]

1.2.2 Non-viral vectors for cell reprogramming

The mostly used non-viral vectors are plasmids, RNAs and transposons. For these non-viral vectors, some extra approaches (electroporation), carriers (liposome, cationic polymers, etc.) or chemicals (polyethylene glycols, nuclear location sequence, etc.) are needed to help the delivery of nucleic acids. Electroporation is simply using electron shots to perforate the cell membrane and let the exogenous genes enter the membrane.[31] The function of the nanoparticle carriers are more complicated. The exogenous genes need to be uptaken by cells, escape from endosome, enter the nucleus, and be transcribed and translated to express the corresponding proteins.[19] Each of these steps can be manipulated by different nanoparticle carriers to enhance reprogramming efficiency. In the first step, positively charged liposomes or cationic polymers are used to help endocytosis due to the negative charge of cell membrane. PEI (polyethylenimine) -based nanoparticles are usually used to buffer the acid environment in endosome and help endosomal escape in the second

step.[32] After the exogenous nucleic acids escape from endosome, the DNase in cytoplasm can also be a threaten. Polyethylene glycols (PEGs) are one of the chemical protectors that can condense the DNA to reduce contact with DNase and its hydrophobic tail can further protect the genes from digestion.[33] For nuclear translocation, nuclear location sequence (NLS) is frequently used to improve the transfection rate.[34] The last transcription and translation steps depend on the vectors themselves.

Episomal Plasmid

Episomal plasmid-based gene delivery is a non-integrating reprogramming method. Most of the plasmids can't replicate themselves after being transfected into the mammalian cells, but episomal plasmids can replicate themselves once per cell cycle within the nucleus in the presence of oriP/EBNA1 (Epstein–Barr nuclear antigen-1).[35] Episomal plasmids are easy to construct and less expensive compared to the viral vectors.[36] Thus, it would be a promising way for cell reprogramming. However, the transfection efficiency of the episomal plasmid based-gene delivery is very low. Thus, scientists usually use nanoparticles such as liposomes, polymersomes, magnetic nanoparticles, etc. to improve the transfection and gene expression efficiencies.[24]

RNA

There are mainly two types of RNAs involved in cell reprogramming and gene delivery studies: mRNA and miRNA. RNA delivery can overcome transgene effects. The synthetic mRNA manipulated cell reprogramming was first published by Warren et al.[37] using Yamanaka factors

and shows the advantages of high transfection efficiency, completely transgene-free and can be applyed on a wide varity of cells.[38] The drawbacks of this mRNA reprogramming methods are: 1. It needs multiple times of delivery process which is labor intensive;[39] 2. It initiates the immune response;[31] 3. It can only be used on specific sample types.[38] miRNA induced cell reprogramming is different from mRNA induced reprogramming. It doesn't require any of the reprogramming factors, instead, there are some novel micro RNAs, such as mir-200c, mir-302s, and mir-369s reported to successfully induce iPSCs derivation via viral vectors or non-viral vectors.[39] Although the reprogramming efficiency is low,[40] if there is a solid set of miRNAs that can reprogram the somatic cells into iPSCs, it's still a promising reprogramming method.

Transposon

Transposons-based reprogramming belongs to integrating reprogramming methods. The transposons are genetic elements which move from one position to another position on the cell genome in the presence of specific DNA sequences. PiggyBac is one of the transposons that is commonly used in the reprogramming process. It is simple to construct and can transfect genes into a wide range of cell lines. The PiggyBac has a higher reprogramming efficiency than plasmid and RNAs and can be easily cleared from cell chromosomes.[39] Despite those advantages, transposons have off-target effects, which might still leave footprints on cell genome and not all the transposons can be deleted completely as PiggyBac.[23] The function of clustered regularly interspaced short palindromic repeats (CRISPR)/CRISPR-associated (Cas) system is similar to transposons. It can integrate exogenous genes into chromosome. Instead of jumping around,

CRISPR/CAS system would insert genes into a specific site in cell genome with the guidance of gRNA. There will be more details about CRISPR/Cas system in Chapter 2.

1.3 Biophysical cues induced iPSCs neural differentiation

In order to treat neurogenic diseases, neural differentiation of iPSCs needs to be achieved. The traditional way of iPSCs/ESCs neural differentiation is to add growth factors into the cell culture medium to initiate the differentiation process by activating neural related signaling pathways. However, this method took about a month to generate the mature neuron cells.[41] Scientists are now seeking new methods to improve the neural differentiation percentage and shorten the differentiation time. Nanomaterials are becoming more widely used in medical applications and tissue engineering. Nanomaterials include a variety of structures. These structures provide us diverse physical properties in mimicking stem cell niche. The nanomaterials can also be surface modified, which is another advantage in the stem cell niche study.

Stem cell niche is the microenvironment in which stem cells grow. It contains extracellular matrix (ECM), adjacent cells, proteins and chemicals in the surroundings. The growth and differentiation of stem cells rely on the stem cell niche. The change of topography and components of the stem cell niche can affect stem cell fate. In material related neural differentiation, we can classify them into two categories: 1. Using the biophysical cue, such as topography and stiffness to directly interfere with the differentiation of iPSCs. 2. Employing the biochemical cue, such as

chemical molecules or protein to induce the differentiation of iPSCs. Here, we mainly focus on the biophysical cue induced neural differentiation.

Synthetic topography cues have a huge influence on stem cell fate. In some cases, cells respond to the surface change of the material and stretch along the same direction as nanostructured patterns on the substrate. There are two types of biophysical cues: 2D membrane substrates and 3D scaffolds. The following discussion is more focusing on the 2D membrane substrates.

Five parameters of membrane topography (shape, size, roughness, height, and stiffness) have been studied in inducing stem cell differentiation. Micro- and nanolithography techniques have been widely adopted to manipulate the surface topography of the 2D membrane substrates. This includes both masked lithography, such as photolithography, soft lithography nanoimprint, etc. and maskless lithography, such as electron beam lithography, ion beam lithography, scanning probe lithography, etc.[42] Multi-architectural chip built by nanolithography is one of the powerful tools to study the effect of substrate morphology change on controlling stem cell behavior. Besides lithography, reactive-ion etching has also been used in substrate fabrication.

Compared to other four characters discussed above, which can be adjusted through fabrication, the stiffness of the substrates depend more on the inherit mechanical properties of the materials, from which the substrates are made. Thus, stiffness can be manipulated through selection of different materials. In some applications, tuning of stiffness is desired for the same type of material, which is common in polymeric substrates. In these cases, stiffness control can be

achieved through controlling the degree of cross-linking as well as the concentration of the polymer precursors.

Here, we will expand in details the impact of the 5 characters (shape, size, roughness, height, and stiffness) of the 2D membrane substrate on the neural differentiation induction.

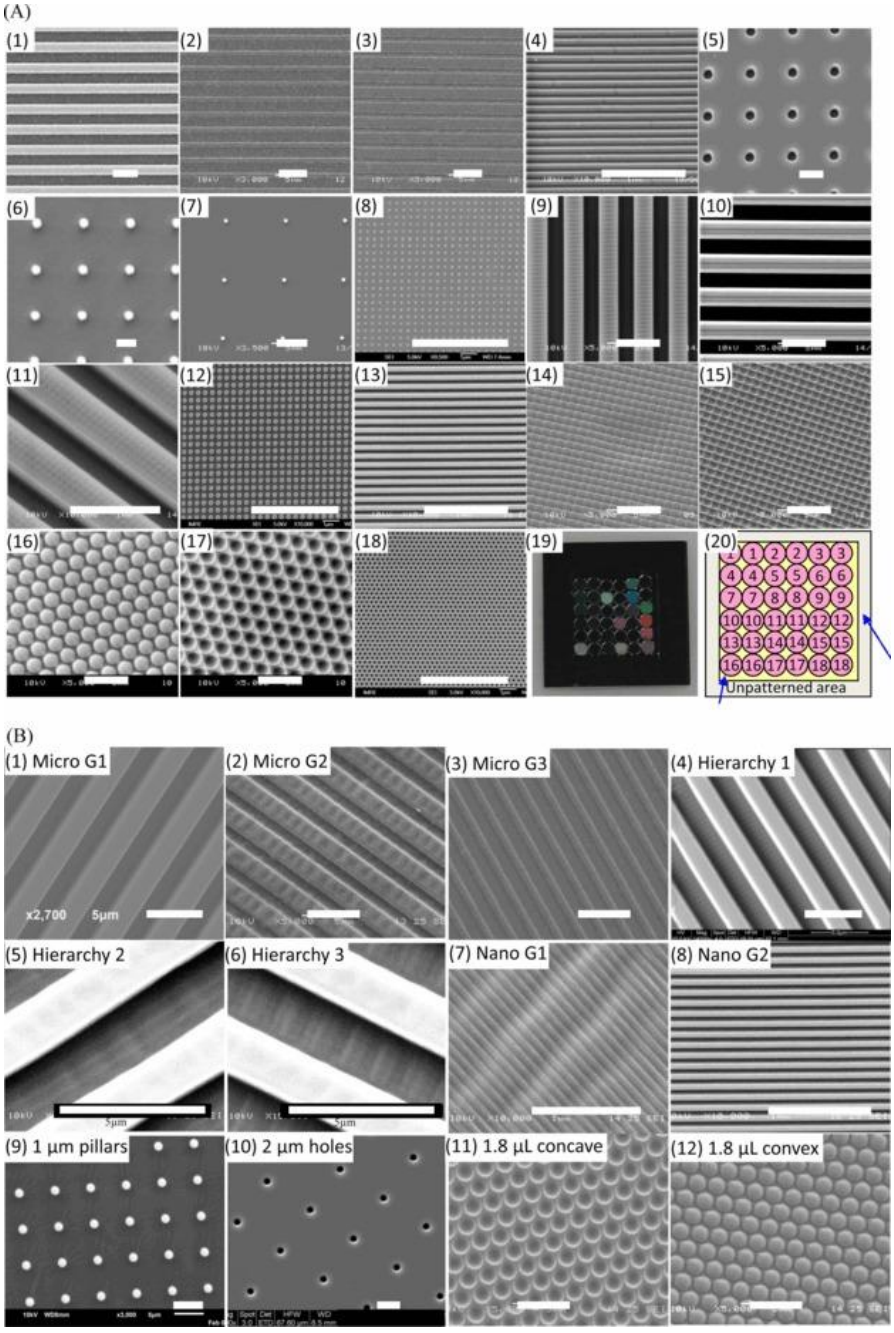

Figure 2. Different architectural patterns on the MARC (A) and PDMS substrate (B).[43] (From "Microarray with micro- and nano-topographies enables identification of the optimal topography

for directing the differentiation of primary murine neural progenitor cells." by Moe, A. A.; Suryana, M.; Marcy, G.; Lim, S. K.; Ankam, S.; Goh, J. Z.; Jin, J.; Teo, B. K.; Law, J. B.; Low, H. Y.; Goh, E. L.; Sheetz, M. P.; Yim, E. K., 2012, *Small, 8* (19), 3050-3061.Copyright by 2020 the John Wiley and Sons)

1.3.1 Shape

The shape of the topography can manipulate the stem cell behavior.[44] The mostly discussed shapes in neural differentiation are anisotropic patterns (such as gratings and grooves) and isotropic patterns (such as pillars and wells). Groove pattern was first found to improve the neurite growth.[45-47] This structure altered the number, length, and angle of neurites,[47] helped the axonal extension,[48] formed larger nerve bundles[48] and reported to have different inducing functions in different cells.[48, 49] Compared to the non-patterned substrate, the groove structure guide cells to grow aligned with the direction of grooves (within the angle of 20°).[50] After co-culture with astrocytes, the stem cells on the groove pattern showed a higher (35.3%) rate in Tuj1 expression than non-pattern group.[50] The grooved structure was even claimed to de-differentiate the glial cells into radial glia-like cell progenitors.[49] Besides the comparison between anisotropic patterns and non-pattern groups, isotropically patterned substrates were also discussed. Multi-architectural chip (MARC) was mostly used to study the shape effect on stem cell fate (Figure 2). The anisotropic and isotropic patterns were found to have different effects on stem cell differentiation. Human

ESCs trended to differentiate into neurons on anisotropic patterns, while the cells differentiated into glial cells on isotropic patterns.[43, 51-54] Though most of the isotropic patterns were considered to induce the glial differentiation, it doesn't mean that they can't induce neuron differentiation. Pillars with 1 μm diameter were also proved to have comparable neuronal induction effect on mNPCs to the gratings.[43, 54] The reason for higher neural differentiation on anisotropic pattern, but not on isotropic pattern could be that the anisotropic structures, such as gratings, provided hPSCs a stronger support in connecting with adjacent cells, promoted the neurite growth, and induced the expression of cytoplasm Yes-associated protein (YAP), which is a key factor in neural differentiation related pathway, and neuronal cell polarization.[55] A combination of anisotropic and isotropic pattern was also used in the stem cell neural differentiation study.[56] The hierarchical structure was found to induce the hNSCs to differentiate into only neurons, not astrocytes. The possible mechanism involved the activation of FAK pathway and focal adhesion.

1.3.2 Size

The size of the matrix structure significantly influences stem cell growth. Most of the studies reporting size induction are based on anisotropic patterns. When the heights of the gratings are the same, the variables can be the size of the grating and spacing. In most studies, they used the same sizes for grooves and ridges.[57-59] The reported neural induction size ranged between hundreds (250-300) of nanometers to a few (2) micrometers.[51, 54, 57-59] However, comparing to micrograting, more studies showed that nanogratings seemed to have a higher induction rate in

neuronal differentiation.[51, 54, 57] For example, iPSCs on the 350 nm nanostructures showed a stronger neuronal differentiation response (including higher neuronal marker expression) than 2 μm and 5 μm.[57] However, the test in another group showed that among the size of 250 nm, 2 μm, and 10 μm, the 2 μm grating had the strongest neuronal differentiation induction.[58] Besides, the anisotropic patterns were also reported to shorten the hESCs neuronal differentiation duration into 5 days without inducers.[59] Regarding the substrate size, another speculated way to control the stem cell differentiation direction is dependent on the initial hiPSCs/ESCs cluster sizes. The larger EBs cultured in 450 nm hydrogel microwells have higher activity in cardiogenesis, while the EBs in 150 nm size tend to differentiate towards endothelial cells.[60]

1.3.3 Roughness

The roughness of the substrates was found to influence the stem cell morphology, proliferation, adhesion and differentiation as well. hESCs seeded on a substrate with different root-mean-square roughness (Rq) from 1 nm to 150 nm, tended to adhere to smooth surfaces rather than rough surfaces. Also, the substrate with higher Rq tended to induce the differentiation of hESCs while the smooth surface maintained the highest pluripotency of the cells.[61] Similar conclusions were also proved by mESC culture on surface with varying roughness .[62] Compared to the substrate with roughness Rq= 1 nm, the pluripotency related gene expression of hPSCs dropped on substrates with roughness of 100 nm and 200 nm.[63] It indicated that the early neuroepithelial formation and motor neuron differentiation were accelerated by glass surfaces with higher Rq.

Two signaling pathway activities were involved in this process: TGF-β/BMP/SMAD signaling pathway and Hippo signaling pathway. The nanotopography directly affected the activity of β1 integrin resulting in the inhibition of Smad1,5,8 in TGF-β/BMP/SMAD signaling and it regulated the TGF-β/BMP/SMAD signaling through Hippo pathway. YAP bound to phosphorylated Smads and prevented them from entering into the nucleus. The downregulation of YAP and Smads nuclear accumulation resulted in the lack of pluripotency and neural differentiation of hPSCs.[64]

1.3.4 Height

The height of the nanotopography not only manipulate the proliferation of the stem cells, but also influence the stem cell neural differentiation. The depth of the gratings controlled the alignment, elongation, and differentiation of the stem cells.[55, 65] Cells on a shallower structure bent their cell body and reached to the bottom of the structure, while cells on the structure with a larger height more often chose to bridge over the structure to reach on the other side[55, 65]. The increasing depth of the gratings can promote cell lateral elongation, alignment, differentiation rate and even control the differentiation direction. However, when it's too deep, it reduced the cell proliferation[55] and prevented perpendicular extension of the neurites.[65] The possible mechanism for this is that when cells grow on an anisotropic structure with a higher depth: width ratio, the bending angle for the neurites to attach the bottom of the grooves become larger, which necessitates a higher energy cost and more filopodia along the horizontal direction to fill the gap. In this case, instead of filling the gap, neurites are more likely to bridge the gap.[65, 66] In another study, hPSCs were seeded on

the same linewidth nanograting with two different heights.[55] The one with 560 nm height experienced an increase of ~35-40% βIII-tubulin$^+$ cells when compared to the 150 nm height group and has been shown to promote the cell attachment and alignment after seeding. This discovery achieved a high neural induction efficiency (reached to ~60% βIII-tubulin$^+$ cells) with a short time duration (~14 days). A similar study was done on pillars with different heights, which showed that taller structures promoted neuronal differentiation of ES-derived precursors and initiated the differentiation within 6 h.[66]

There are two proposed explanations to this nanotopography controlled neural differentiation behavior. The first assumption is that changing the height on the 2D topography influences the expression of Matrix metalloproteinases (MMPs), which is essential in responding to brain ECM remodeling and in brain development.[55] The change of MMPs expression affects the stem cell differentiation. Another explanation is that the YAP expressing location is manipulated by nanotopography and its stiffness, height, and structures.[40, 55] YAP is an important factor in Hippo pathway. Giulio Abagnale et al.[40] claimed that when using the topography of materials to induce iPSC differentiation, the TAZ, a paralog of YAP, is localized in filament of the iPSCs during differentiation process. The topography changes induced cell cytoskeleton change while the TAZ responded to the actin protein. This indicated that TAZ is indirectly manipulated by topography change. They also suggested that the location of YAP is related to stem cell differentiation by interacting with BMP signaling pathway. The larger height group (560 nm) was detected with a higher cytoplasmic YAP expression comparing to the flat control and

smaller height group (150 nm). The above facts show that stem cell fate can be changed by nanotopography.

1.3.5 Stiffness

In our body, each organ has different mechanical properties, for example, brain elasticity is about 0.1–1 kPa; muscle elasticity is about 8-17 kPa; and osteo elasticity is about 25-40 kPa.[67] Over the decades, scientists have tried to use the mechanical properties of various materials to mimic the *in vivo* elasticity of different tissue microenvironment to modulate the stem cell behavior and differentiation activities. It has been proved that materials with different stiffness could modulate stem cells to achieve osteogenesis differentiation,[68, 69] myoblasts formation,[70] neurite growth,[67] and neuronal differentiation.[71, 72] Although the actual stiffness of matrixes would be varied, some basic finding is similar: softer substrates increase the neural lineage formation at an early stage, while stiffer substrates enhance the later stage neuron formation. When mESCs were seeded on to gelatin-based substrates with different stiffness, the cells tended to attach better to the softer matrix with Young's modulus similar to brain and spinal cord microenvironment than the one with higher stiffness. The effect of stiffness on neuronal differentiation of the stem cells is also related to the maturity of the cells. It had a higher impact on the late stage of differntiation especially on phenotype changes.[73] A similar result has been found on hiPSCs and hiPSCs-derived cells. The softer electrospun substrates initiated the early stage neural lineage development, whereas the stiffer substrate promoted neuronal differentiation from hiPSC-derived neural

progenitors and late stage motor neuron formation.[74] Stiff substrates were also proven to enhance the synaptic connectivity and current transmission in mature neuron network.[75] Besides the above function, neuronal, astrocyte and oligodendrocyte differentiation can also be manipulated by stiffnesses of the matrix. Each differentiation direction falls in an optimal Young's modulus range. Neurons prefer soft matrix; oligodendrocytes prefer stiffer matrix and astrocytes lay in-between.[76] The neuronal differentiation of ESCs and ESCs-derived neural cells was increased on the softer substrate with 2 kPa, while a decrease of astrocyte formation was found on the same substrate.[73] NSCs on stiff graphene scaffold were more likely to differentiate towards astrocytes, and those stiff matrix resulted in neuron suppression.[77] The possible mechanism of stiffness induced neural differentiation was studied by Samira et al. [78] They found that the stiffness change of the substrate material manipulated the YAP protein localization and phosphorylation, and then affected the neuronal differentiation of hPSCs/hESCs. The hard hydrogel substrate (~10 kPa) increased the F-actin amount in the cytoplasm and the YAP protein and its cofactor trended to go into the nucleus, which promoted the self-renewal[79] of hPSCs. While on a soft substrate (~0.7 kPa), F-actin formation was decreased, which made enough room for YAP phosphorylation in the cytoplasm. The phosphorylated YAP blocked the Hippo pathway to improved the neuronal differentiation.

Table 1. Stem cell differentiation based on substrate characters.

Manipulated substrate characters	Initial stem cell type				Final differentiated cell type			Induction factors/medium during differentiation
	iPSCs /ESCs	EBs	iPSC/ ESC-derived cells	NSCs / NPCs	neuron	astrocyte	oligodendrocyte	
Shape	51, 52, 55		48	43, 50, 52-54, 56, 80, 81	43, 48, 50-56, 80, 81	43, 51-54, 80	43, 51, 80	43, 48, 50-53, 55, 80, 81

Size	51, 57-59	57		54, 80	51, 54, 57-59, 80	51, 54, 80	51, 80	51, 57, 58, 80
Roughness	61, 63, 82				61, 63, 82			63, 82
Height	55		66	65	55, 65, 66	65		55, 65, 66
Stiffness	73, 74, 78, 79		73, 74	76, 77	73, 74, 76-79	73, 76, 77	76	73, 74, 76, 77

1.4 M13 filamentous bacteriophage

M13 phage is a type of filamentous bacteriophage. It's a lysogenic phage, which doesn't kill host cells. M13 phage uses the pIII coating protein to interact with F-pilus on *E. coli* to insert the phage genome into the bacterial cells. Then, the phage genome works as a template and use the supplements instead of bacteria to complete the DNA replication, transcription, translation and virus packaging.[83]

1.4.1 Structure of M13 phage

M13 phage is a human-safe nanofiber-like virus (~900 nm long and ~7 nm wide) that specifically infects bacteria.[84] Its cylindrical structure is composed of ~3000 copies of the major coat protein (called pVIII) surrounding a circular single-stranded (ss) DNA genome.[85] The ssDNA

encodes the major coat protein (pVIII) and four other structural proteins (pIII, pVI, pVII, and pIX) at two ends. Each of these tail proteins has about 5 copies. M13 phage can be genetically modified to express foreign peptides on its surface and also can self-assemble into different structures.[86]

1.4.2 Phage display and phage library

Phage display was first developed by George Smith in 1985.[87] He managed to genetically modify the surface protein of the filamentous bacteriophages and let foreign peptides fuse onto the N-terminus of the coat proteins. All five M13 coating proteins were proved to be able to display the foreign peptides on their termini.[88-92] The most widely used display is on pVIII major protein and PIII protein. A phagemid is usually used in the display process. The phagemid has the characters of both plasmid and M13 virus components. It can replicate itself as plasmids and can be packed into viral coat proteins as virus DNAs. Phagemid usually encodes only one type of coating protein. It doesn't have the ability to finish the whole life cycle of bacteriophages by itself. Thus, helper phages are applied to provide the other coat proteins and help their package.[93] The external peptides are displayed on the termini of pVIII major protein as a mosaic display. The phagemid produces pVIII fusion protein, while the helper phage provides the wild type (WT) pVIII protein to ensure the normal phage packaging. The fusion pVIII protein and WT pVIII protein are randomly packed into phage coating shell, thus, the fusion protein was decorated on the major coats in a mosaic pattern. Instead of mosaic patterns, all the copies of the pIII protein are fusion

protein in the pIII display. Because pIII is a minor coat protein, modifications on this protein wouldn't disturb the packaging.

Phage libraries are built based on the phage display technique to present random peptides or different antibodies on the phage particles. These libraries can be used to biopan against various targets, such as cells, proteins, animal organs or even nanoparticles, to select the target-specific peptides or antibodies.[94] They are powerful tools for both basic research and biomedical applications.[95]

1.4.3 Potential applications

Phages have applications in multiple fields including chemistry, materials, and medicine (Figure 3).[96] They can self-assemble into different 2D films to induce the differentiation of stem cells and can be used to study the biophysical and biochemical effects on stem cells.[97-99] Besides, phages could also act as templates to direct the assembly and growth of various nano-/micromaterials, such as gold nanoparticles,[100] silica fibers,[101] and hydroxyapatite (HAP) crystals.[102] Phages also serve as powerful tools enabling early disease diagnosis by capturing biomarkers[103] and in disease treatments by providing gene delivery methods.[104]

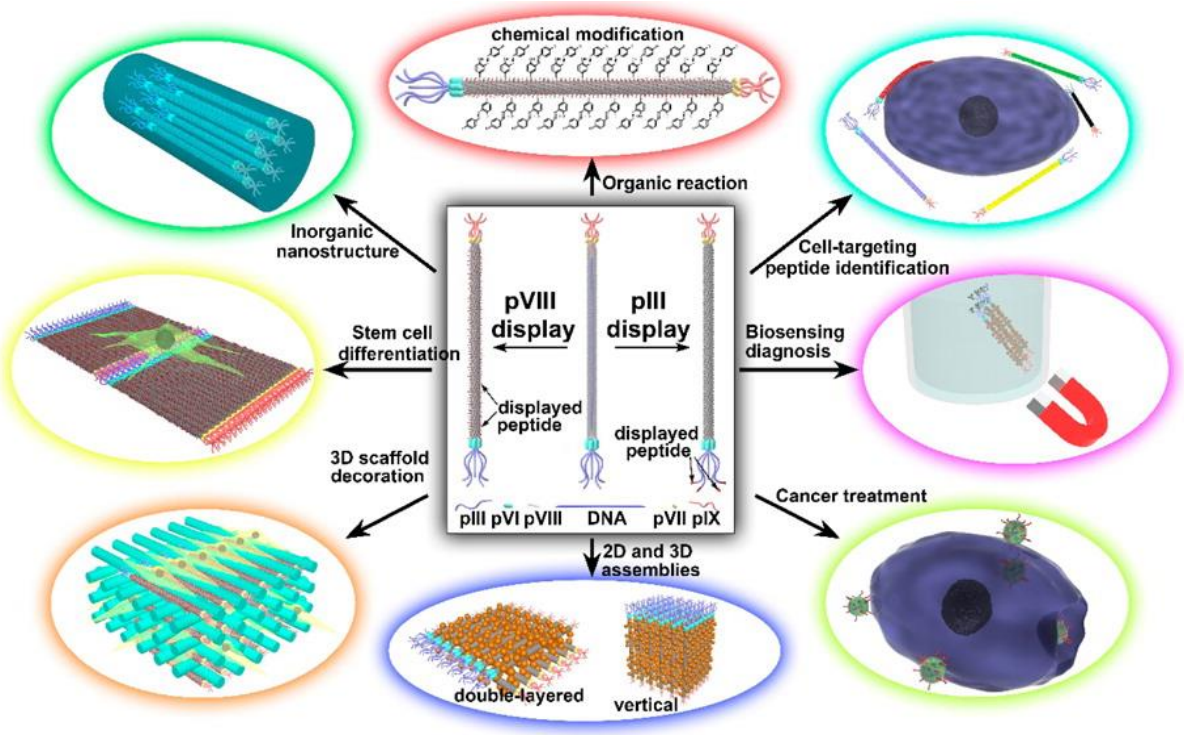

Figure 3. Potential applications of filamentous phages.[96] (From "Phage as a Genetically Modifiable Supramacromolecule in Chemistry, Materials and Medicine." by Cao, B. R.; Yang, M. Y.; Mao, C. B., 2016, *Acc. Chem. Res.*, , 49 (6), 1111-1120. Copyright by 2020 the ACS publications)

Chapter 2. Highly Efficient Reprogramming of Human Fibroblasts into HiPSCs by Cell-targeting Nanoparticles

2.1 Abstract

Human induced pluripotent stem cells (hiPSCs) have the ability to differentiate into any type of cells, which have a huge potential in stem cell therapy and tissue regeneration applications. HiPSCs are reprogrammed from mature cells, such as human dermal fibroblasts (HDFs), coming from the patient. It avoids the immune rejection and also overpasses the ethical issues that other human stem cells have. Thus, there is a huge need of hiPSCs. However, the reprograming efficiency is low. Here, we selected a 12-mer HDF-internalizing peptide (AHNHTPIKQKYL) from phage library via biopanning, which has a strong binding affinity and specificity to the HDFs. Later, we will use this peptide decorated lipid-based nanoparticles to achieve enhanced delivery of four reprogramming genes (*Oct4, Sox2, Klf4, and c-Myc*) into HDFs.

2.2 Introduction

Human induced pluripotent stem cells (hiPSCs) and human embryonic stem cells (hESCs) are powerful tools in disease modeling and cell therapy.[105] They have the potential to differentiate into any other cell types in human body.[106, 107] The patient-specific hiPSCs can be derived and differentiated into different cell types with the same genetic information as the donor patient[108-110]

which is called “disease in a dish” model. Disorders affecting neurons, blood, liver, heart, lung, and immunosystem as well as cancer have been studied using these hiPSCs disease models.[111-114] They benefit scientists to study the pathogenesis of human diseases,[111-113, 115, 116] especially neurological disorders with the high complexity of neuronal system and challenges in culturing neurons *in vitro*.[108] Stem cell-based therapy can also serve as an alternative way of tissue transplantation.[117] The differentiation potential of hiPSCs and hESCs sheds light on the treatments of damaged organs, which is otherwise relying on donor organs.[15, 118-120] hESCs have been used in rebuilding the retinal pigment epithelial (RPE) cells to treat macular degeneration (MD).[108, 119, 120] hiPSCs have the similar function as hESCs but bypass the ethical issues of hESCs. Thus, it’s a better cell source for the stem cell-based therapy.

HiPSCs are derived from somatic cells through a reprogramming process. *Oct4, Sox2, Klf4, and c-Myc* are four reprogramming genes first reported by Yamanaka et. al. that can efficiently reprogram somatic cells into hiPSCs.[10] *Oct4, Sox2, Klf4, and c-Myc* genes have different functions in the reprogramming process. *c-Myc* is a protooncogene, which enhances cell proliferation and involves activating chromatin environment during the early stage of reprogramming.[121, 122] *Klf4* together with *c-Myc* increases the efficiency and kinetics of reprogramming process, contributing to the opening of chromatin, which is essential for the reactivation of pluripotency.[122] *Oct4* and *Sox2* function together to activate the Oct-Sox enhancer and initiate the expression of downstream pluripotent-related genes, including *Nanog, Fgf4* and themselves.[123] These two factors work in auto-regulatory positive feedback loops to reinforce the stem cell pluripotency.

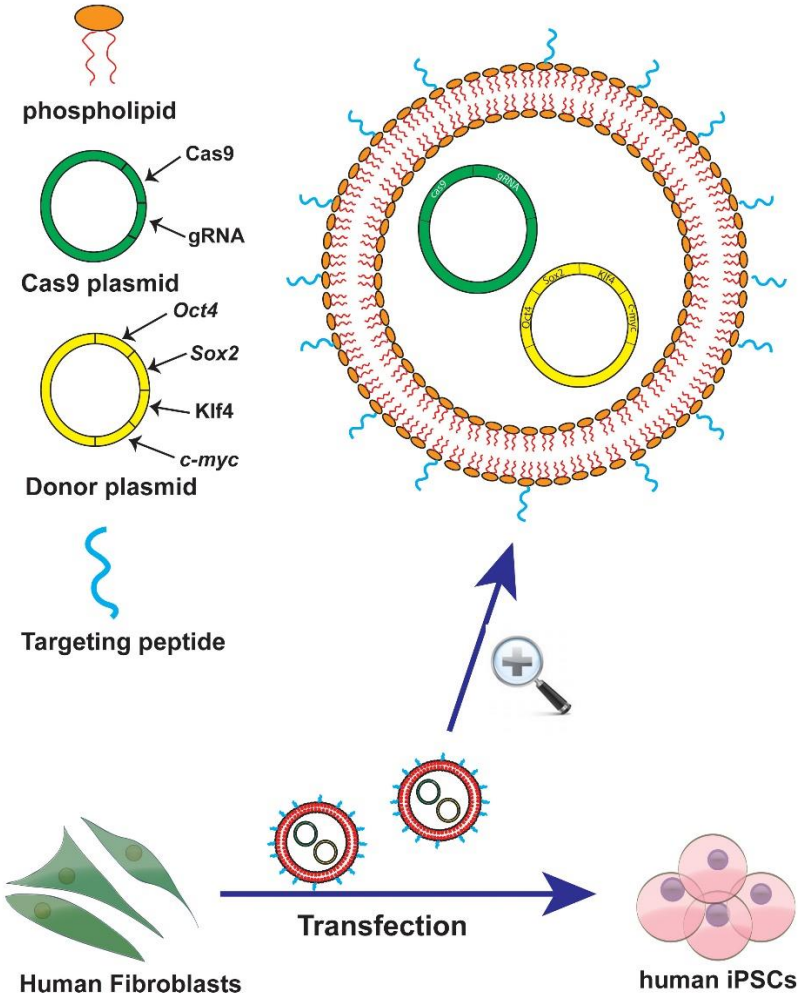

Figure 4. Delivery of the reprogramming genes into human fibroblasts to convert them into human iPSCs. Lipid-based nanoparticle (LBN) is composed of two lipid layers decorated with fibroblast-targeting peptides on the surface. Cas9 plasmid and donor plasmid (containing *Oct4, Sox2, Klf4,* and *c-Myc*) is encapsulated in the LBN. The Cas9 plasmid will produce Cas9 endonuclease and gRNA for gene cutting, while the donor plasmid will serve as a template in homologous

recombination. The peptide-modified non-viral LBNs carrying both Cas9 plasmid and donor plasmid will be delivered into human fibroblasts for reprogramming fibroblasts into hiPSCs.

Many commercial reprogramming kits are built upon these four genes. In a typical reprogramming process, *Oct4, Sox2, Klf4, and c-Myc* are sent into the somatic cells, either non-integrating or integrating into the chromosomes. Then, the corresponding reprogramming proteins are translated and function in the somatic cells to initiate the expression of pluripotent genes. Finally, the reprogramed cells were confirmed to be hiPSCs with pluripotency.[121, 124] There are also other ways of reprogramming, for example, by using microRNA[125] or small molecules.[126] However, the efficiency of these methods is usually lower than that of using the four reprogramming factors (*Oct4, Sox2, Klf4, and c-Myc*) method. It has been reported that using five reprogramming genes (*Oct4, Sox2, Klf4, c-Myc, and Lin28*) can reach a higher efficiency compared to four genes (*Oct4, Sox2, Klf4, and c-Myc*)[37] method. However, the five-gene method requires much more time and effort in the plasmid construction step. In this work, we chose the reliable approach of using the four reprogramming genes (*Oct4, Sox2, Klf4, and c-Myc*) to achieve the hiPSCs derivation (Figure 4).

Several types of cells have been used in the reprogramming process, for example, human dermal fibroblasts (HDFs), blood cells, human adipose stromal cells, human foreskin fibroblasts, and human mesenchymal stem cells.[39] Because of the easy access, we chose HDFs as our primary cell source to achieve this reprogramming process.

As was mentioned above, many approachess have been applied to achieve the derivation of hiPSCs. In the current status, both viral and non-viral methods suffer from a low reprogramming rate (usually 0.1-1%) and a long duration (usually from 15 days to one month).[39] The viral method of overexpressing specific transcription factors in somatic cells[10, 127, 128] still has biosafety concerns. Compared to the viral method, non-viral is safer. A new non-viral genome editing approach called clustered regularly interspaced short palindromic repeats (CRISPR)/CRISPR-associated (Cas) system (CRISPR/Cas system) has been used as a powerful gene editing tool in building stable expression cell lines with simple manipulation and high specificity, especially type II CRISPR/Cas 9 system. This typeII CRISPR/CAS9 system is derived from *Streptococcus pyogenes* bacterial immune defense. It works based on RNA-DNA binding, which only needs a design of 20 nts of RNA-DNA base pairing to achieve precise cleavage. CRISPR/Cas9 system contains 2 important parts: Cas9 protein and single-guide RNA (sgRNA). Cas9 protein is an RNA-guided nuclease, which has two functional cleavage domains: HNH and RuvC. They function as scissors to cleave the targeting sequence on the chromosome.[129] sgRNA also has 2 components: CRISPR–derived RNA (crRNA) and trans-activating RNA (tracrRNA). CrRNA includes a specific sequence, which is complementary to targeting sequence on the chromosome. TracrRNA, base-pairs with part of the crRNA, which then recruits Cas9 protein to form a sgRNA-Cas9 protein complex. The

targeting sequence on the chromosome is composed of protospacer (complementary to crRNA) and protospacer adjacent motif (PAM). A five-prime NGG PAM is needed immediately flanking the protospacer. Thus, the whole targeting sequence is coded as $GN_{20}GG$, pairing with sgRNA-Cas9 protein complex. Eventually, the sgRNA-Cas9 protein complex cuts the targeting sequence, resulting in double-stranded breaks (DSBs).[129, 130] A donor plasmid including reprogramming genes (Oct4, Sox2, Klf4, and c-Myc) will be served as a template during the process of homology-direct repair (HDR), forming a stable hiPS cell line. However, the drawback of the non-viral method is that it has a very low delivery efficiency and has limitations in *in vivo* gene delivery.[131]

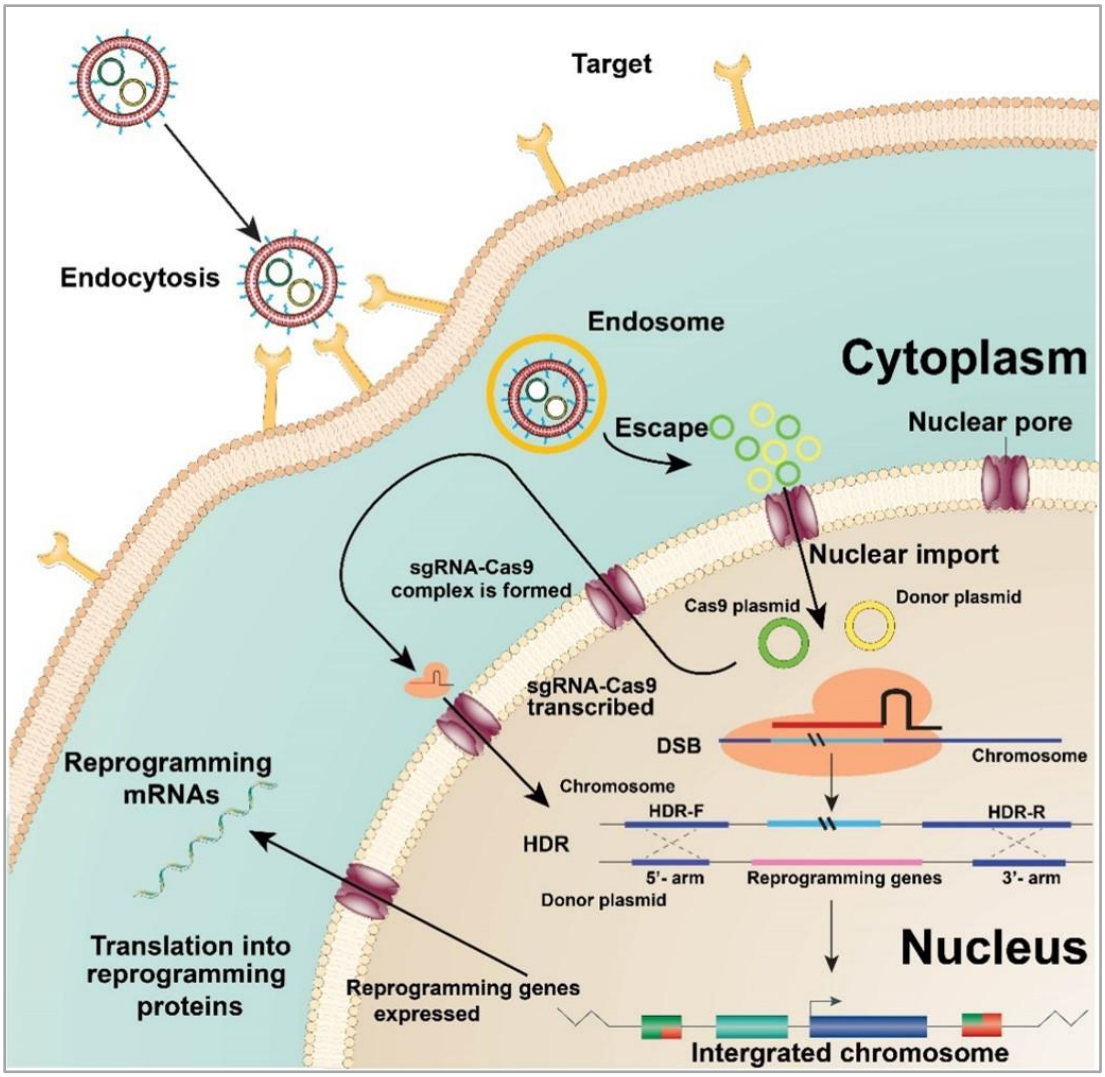

Figure 5. The targeting peptide decorated LBNs deliver reprogramming genes into fibroblast cells and the cells are reprogramed with the help of CRISPR/Cas9 system. The CRISPR/Cas9 system (including Cas9 plasmid and donor plasmid) is encapsulated inside the targeting peptide decorated LBNs and delivered into the fibroblast cells. Then, the Cas9 plasmid and donor plasmid go into the nucleus to reprogram the cells. The Cas9 plasmid is transcribed and translated into sgRNA-Cas9 complex, which binds to the specific site on the chromosome and perform the double-stranded break (DSB). The donor plasmid serves as a template for the DSB region in homology-

direct repair (HDR) process. The reprogramming genes are integrated on to the chromosome and then translated into proteins to initiate reprogramming.

Hence, we proposed to develop a new non-viral targeting-peptide decorated lipid-based nanoparticles (LBNs) to deliver the reprogramming genes and CRISPR/CAS9 system with a higher reprogramming efficiency as well as to shorten the duration (Figure 5). Nanoparticles have been serving as powerful carriers in gene delivery system. It has been reported that the LBNs can achieve reprogramming in less than 8 days.[132] Targeting peptides has been found to improve the gene delivery efficiency.[133, 134] Biopanning selection, which has been proven to successfully identify cell-specific peptides,[135-139] was used to select specific internalizing peptides to decorate on the LBNs. A combinatorial Ph.D.™-12 Phage Display Peptide Library of 12 random dodecapeptides on pIII minor coat protein was used as the selection library in biopanning process (Figure 6). These12-mer displayed peptides are exposed on the N-terminal of the pIII protein to interact with cells. After 4 rounds of biopanning, we successfully selected 3 promising targeting peptides with the highest HDF internalizing efficiency and identified the strongest one for gene delivery use.

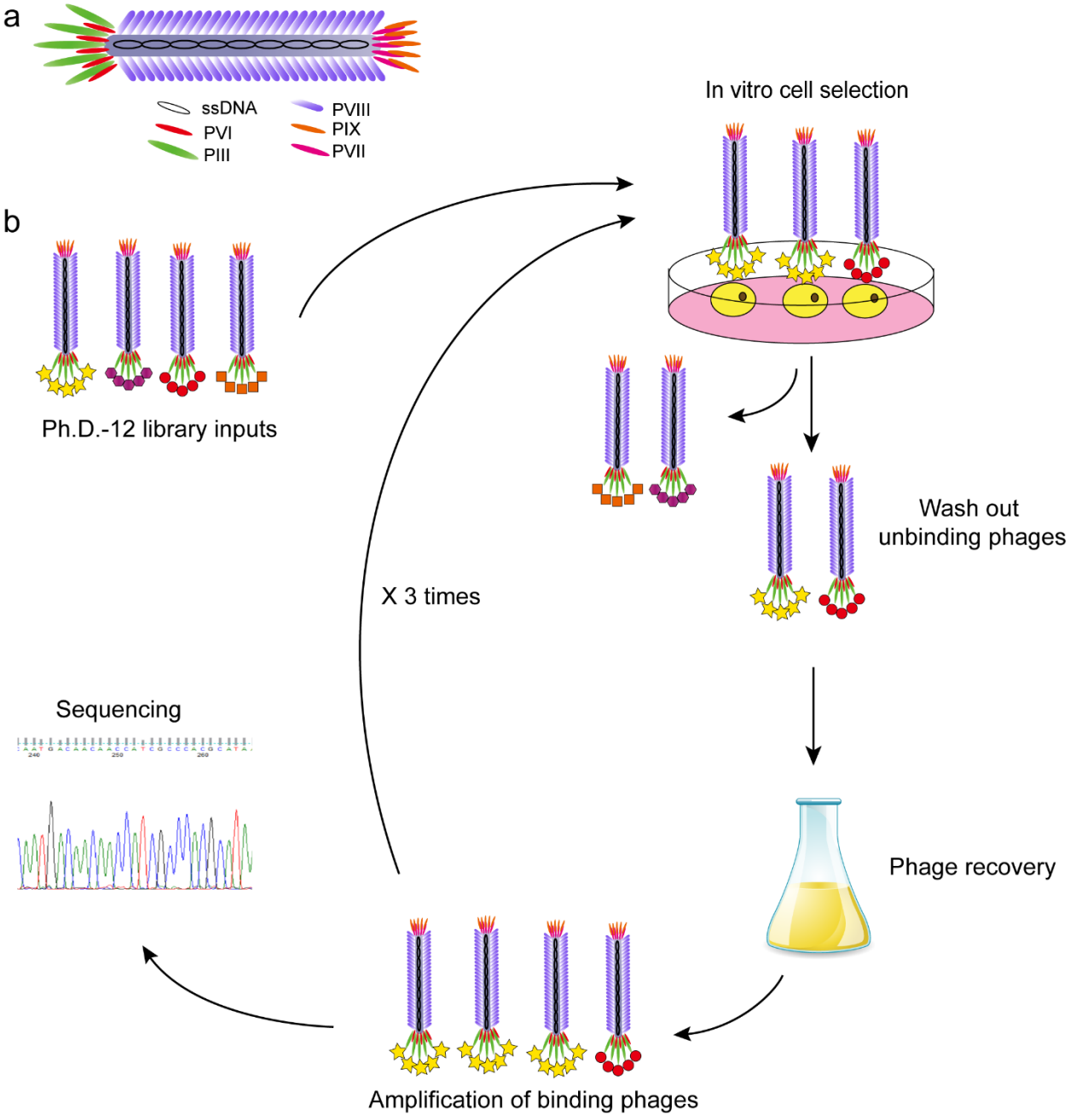

Figure 6. Biopanning procedure of selecting human dermal fibroblast cells (HDFs)-targeting peptides from phage library. a) Wild type M13 bacteriophage. M13 phage was composed of a single strand DNA (ssDNA) and a protein shell, which included ~3000 copies of PVIII protein and

4 minor proteins (PVI, PIII, PIX and PVII). b) Ph.D.™-12 phage display library (pIII display) was added as first round input into HDFs. The HDF-targeting peptides were collected and amplified, while the unbound phages were washed out. The output of the previous round served as an input in the next round. This process was repeated for 3 more times.

2.3 Materials and Methods

2.3.1 Cell culture

Cryopreserved adult human dermal fibroblasts (HDFs) (Cell Application Inc.) were defreezed in 37 ˚C water bath. Cells were centrifuged and resuspended in basal medium with adult HDFs growth factor (Cell Applications.). The full medium was changed every other day for HDF growth.

2.3.2 Phage biopanning

HDFs were seeded on a 60 mm well plate until they reached 80-90% confluency. The basal cell culture medium was used to incubate with HDFs for 1 hour at 37˚C before incubating with phage library. To remove the phages that bound to the container, blocking buffer (0.5%(w/v) bovine serum albumin (BSA) in basal medium) with primary phage library (NEB) was added to an empty 60 mm dish, which was incubated at room temperature for 1 hour. The depleted phage library was then transferred directly to the HDFs and incubated at room temperature for 1 hour with gentle agitation every 5-10 min.

After the 1-hour incubation, the blocking buffer with unbound phage was removed from the HDFs. The cells were washed carefully with 4 ml of cold washing buffer (0.5%(w/v) BSA and 0.1%(v/v) Tween 20 in basal medium) for 7 times to remove the non-specific binding phages. Then, the cells were incubated on ice for 10 min with 1 ml elution buffer. The eluate containing HDF-membrane-binding phages was neutralized with 187.5 µl of 1 M Tris-Cl (pH 9.1) and removed from the cell culture dish. After that, the cells were washed 2 times and treated with lysis buffer to release the HDF-internalizing phages. The lysate was transferred into 20 ml LB medium with 200 µl overnight-incubated *E. coli* K12 ER2738 (NEB). The above mixture was incubated at 37˚C with vigorous shaking for 4.5-6 hours to allow the selected phage amplification.

After the incubation, the mixture was centrifuged to separate phages from bacteria. The supernatant containing phages was transferred into a fresh tube and 1/6 volume of 16.7% Polyethylene glycol (PEG)/ 3.3M NaCl solution was added to the supernatant at 4 ˚C overnight to allow phage precipitation. After the overnight incubation, centrifugation was performed to collect the precipitate. The precipitate was then resuspended in PBS solution. These precipitation, centrifugation and resuspension steps were repeated for another time to purify the phages. A nano photo thermometer was used to identify the concentration of this output phage solution, which served as an input for the next round ($1x10^{10}$ pfu/ml) biopanning selection. After 3-4 rounds of the selection, the final output was tittered on IPTG-Xgal plates and sent for sequencing. RELIC software was used to analyze the sequencing results.

2.3.3 Internalizing peptides specificity and affinity test

The HDF-binding peptides selected by biopanning (Table 2) and one control peptide (GLHTSATNLYLH) were synthesized with GGGGK linker and a FITC tag on their C terminus. HDFs were seeded on to the laminin-coated culture plates to reach to a 90% confluency. Basal medium was used to treat the cells at 37°C for 1 h. The peptides were added into blocking buffer to reach two different concentrations 5 µM and 10 µM. Next, the HDFs were separately incubated with these peptides at RT for 1h. After the incubation, the cells were washed with PBS for 3 times to remove the unbound peptides and treated with CellMask™ Plasma Membrane Stains (Life technology) at 37°C, 5% CO_2 for 8 min. The cells were then washed with PBS to remove the extra stains and fixed with 4% Paraformaldehyde (PFA) at room temperature for 10 min. VECTASHIELD® Hardset Antifade Mounting Medium with DAPI was used at the last step to prepare microscope slides. The slides were characterized by a confocal microscope (Leica SP8). The fluorescence image preparation steps were similar to microscope slide preparation. After incubating cells with FITC labeled peptides, the cells were fixed with 4% PFA and penetrated with 0.3% Triton X-100. CytoPainter F-actin Staining Kit (Abcam) was used to stain the cytoskeleton and DAPI was used to stain the cell nucleus. The stained cells were imaged by fluorescent microscope (Nikon)

2.3.4 Fluorescence intensity quantification analysis

ImageJ was used to quantify the mean fluorescent intensity of the HDFs. Two different peptide fluorescent intensities (slide section intensity and single cell intensity) were characterized and compared between experiment peptide groups, control peptide group and non-peptide group. For slide section intensity quantification, 6 cells were randomly selected by square tool according to their nucleus position in DAPI channel, then the mean fluorescent intensity of this area in the peptide-FITC channel was measured by ImageJ (3-5 images were used for each group). For single cell intensity quantification, the freedom tool was used to draw the cell shape based on the plasma membrane channel and the mean fluorescent intensity of this cell in the peptide-FITC channel was measured by ImageJ (4 images were used for each group). Background autofluorescent from laminin was tested and subtracted in the measurement.

One-way ANOVA and Tukey's test were applied to perform statistical analysis in fluorescent intensity quantification experiment. Different groups were compared with a p-value less than 0.05, or 0.01 considered significantly different.

2.4 Results and discussion

2.4.1 Phage library Biopanning selected fibroblast-internalizing peptides

Biopanning was carried out using a Ph.D.-12 phage display peptide library to discover the HDFs-internalizing peptides with the highest frequencies (Figure 6). Sixty random plaques on the 3rd round IPTG-Xgal plate were sent for sequencing. Three promising peptides were found with high frequencies in the sequencing result (Table 2). There are two reasons that could result in high frequencies in sequencing: 1. high binding affinity to the target; 2. high growth advantages. Here, RELIC software[140] was used to analyze the sequencing result based on the sequencing diversity and amino acid frequency distribution. INFO program in RELIC mathematically measured the chance of collecting a nonspecific binding peptide versus the chance of collecting a specific binding peptide. This program can automatically subtract the noise from phage amplification life cycle and provide us with the that result only due to the binding affinity. It can determine the success of biopanning process in each round by rating the information content of the outputs. A high information content of the output means the corresponding biopanning selection result in that round is based on the affinity of the peptides rather than growth advantages. This indicates the selection of the corresponding round is reliable. It can also rate each peptide sequence to determine whether it's selected based on affinity or growth advantage.

Table 2. Frequency of HDF internalized peptides.

Peptide sequence	Frequency (X out of 60 sequences)
SYPSNALSLHKY	5/60
AHNHTPIKQKYL	5/60
WSFGLPHSPQHL	3/60

The overall information content of the 3rd and 4th round output was compared to the starting Ph.D.-12 phage library information content (Figure 7). The low information peptide sequences were presented on the left of figure 2.4 and the ones with high information content were presented on the right of the figure. The higher the information content is, the lower the growth advantage the outputs have. Compared to the starting Ph.D.-12 phage library, 3rd round output and 4th round output have 2 peaks instead of 1 peak. The first peak in round 3 and 4 overlapped with the starting library, which showed that the output kept some of the randomness as the starting library. The second peak had a higher information content score than the starting library, which indicated the outputs in these 2 rounds were selected on affinity binding rather than growth advantages. Compared to the 3rd round, 4th round had a higher occurrence in the second peak. This showed that the resultant output from the 4th round is reliable. The output information hasn't been affected by growth advantages.

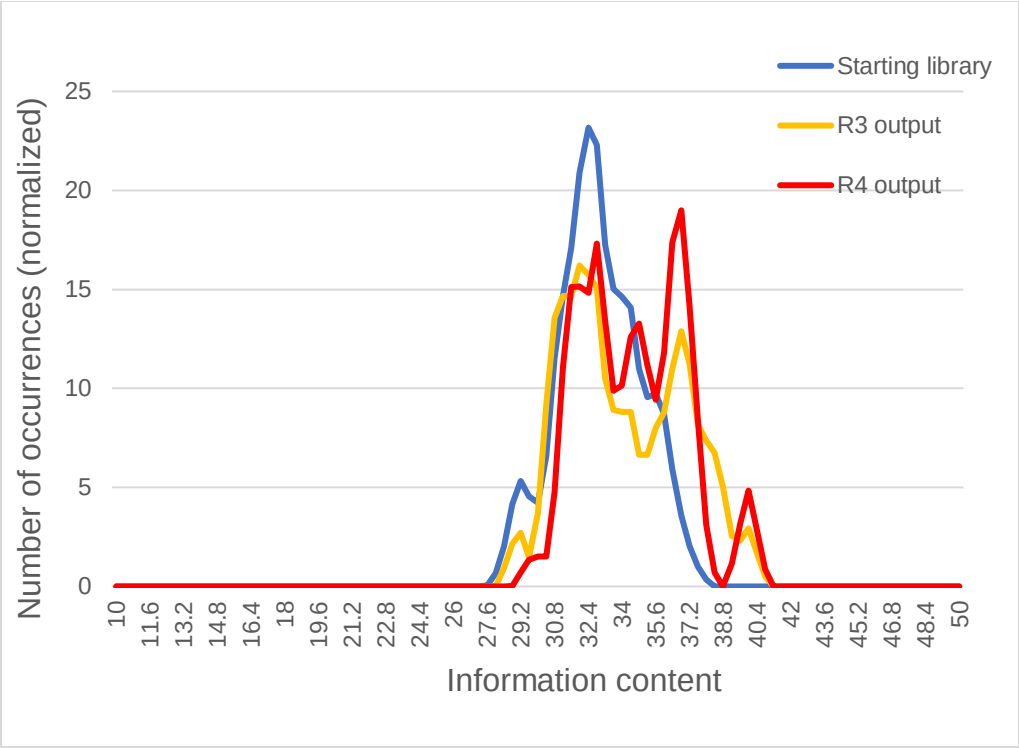

Figure 7. Information content changing in each selection round. The blue line, yellow line, and red line represent the starting Ph.D.-12 library input, 3rd round selection output, and 4th round selection output, respectively. The higher information content the output had, the higher specificity and efficiency the output showed. The 4th round selection had a relatively higher information content than 3rd round selection and starting library. This indicated the output from 4th round was more reliable, and the selection was more based on the binding affinity rather than growth advantages.

The INFO program was also used to calculate the information content for the selected 3 peptides. The INFO value of HDF-targeting peptides was compared to the average INFO value in the round 4 selection (Table 3). The higher value indicated a lower random occurrence and less

favored in viral growth, which also showed a greater chance of selection based on the binding affinity. Compared to the average INFO value, the selected HDF-internalizing peptides all had a greater information content value, which indicates that these peptides truly bound to the HDFs with high affinity rather than phage amplification advantages.

Table 3. INFO value of each selected peptides.

Peptide sequence	INFO value
SYPSNALSLHKY	34.272
AHNHTPIKQKYL	36.303
WSFGLPHSPQHL	36.706
Average INFO value	34.53

2.4.2 Verification of the affinity and specificity of the selected peptides

In order to find out the best HDF-binding peptide among the selected peptides, the FITC labeled peptides were incubated with cells. SYP, AHN, and WSF were the beginning 3 amino acid sequences for SYPSNALSLHKY, AHNHTPIKQKYL, and WSFGLPHSPQHL, which were used to refer to those 3 different peptides in this project. We first tested the binding affinity of each peptide under 2 different concentrations (Figure 8). The concentration of 5 μM and 10 μM of FITC label peptides were incubated with HDFs. The results of these two conditions were consistent.

Compared to the control peptide (GLHTSATNLYLH), which can be barely detected, the selected HDF-targeting peptides showed good binding to the cells. Because the cell density in those images was the same (Figure 8), the AHN and SYP groups had more target binding sites than the WSF group under both 5 μM and 10 μM. AHN among the 3 selected peptides has the highest fluorescence intensity in the image, which indicated that the AHN had the most abundant binding sites on the cells or it had the highest affinity among these peptides. Because the 10 μM images had a better contrast and stronger signal, we chose 10 μM as the optimal concentration in the following experiments.

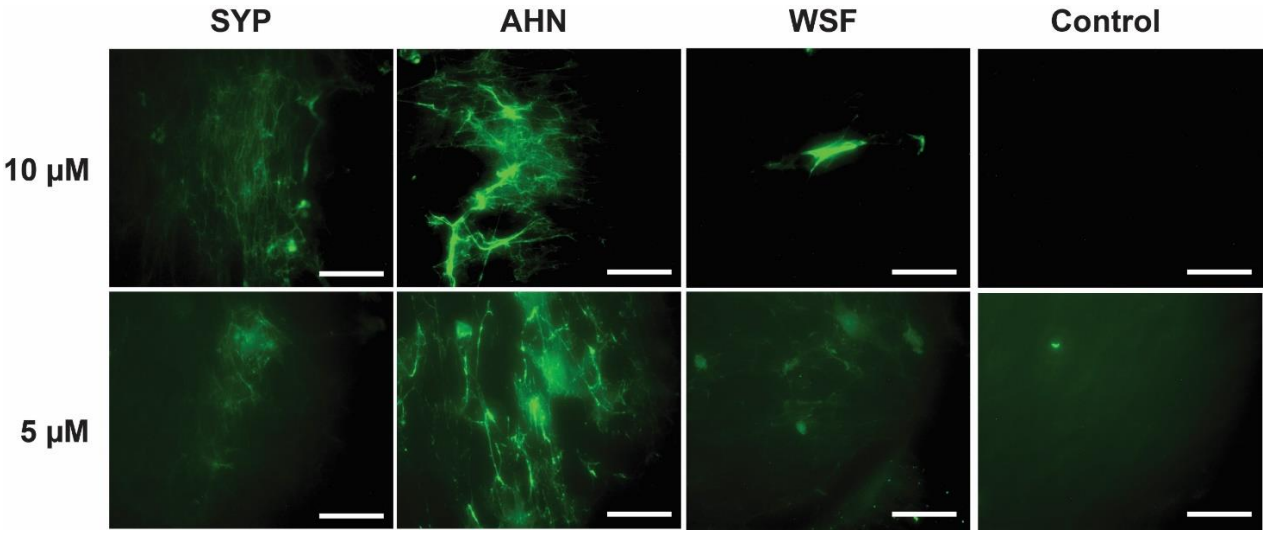

Figure 8. Peptide incubation test with different peptide concentrations (5 μM and 10 μM). Compared to the control peptide group, all the selected peptides showed specific binding to the

HDFs. ANH group had a higher fluorescence intensity than SYP and WSF groups under different concentrations, which indicated a stronger binding. Scale bar: 100 μm.

The images in Figure 8 showed no obvious individual cells. To further confirm that the selected peptides were bound to the cells, not the cell substrate, the cytoskeleton F-actin and nucleus were co-stained after the peptide incubation (Figure 9). The F-actin staining did inform some of the signal cell morphology, but not obvious with high cell density. Non-peptide group was used to eliminate the autofluorescence of the cells. The WSF showed a very weak binding affinity. The SYP and AHN groups had better binding compared to the WSF, control peptide and non-peptide group. They also showed a comparable overlap with F-actin, which indicated that they specifically bound to the cells. According to figure 9, we found that the F-actin existed both in intracellular cytoskeleton and extracellular matrix. Fibroblasts are highly involved in the extracellular matrix formation.[141] Thus, it drew our curiosity that where those peptides bind to, inside or outside of the cells?

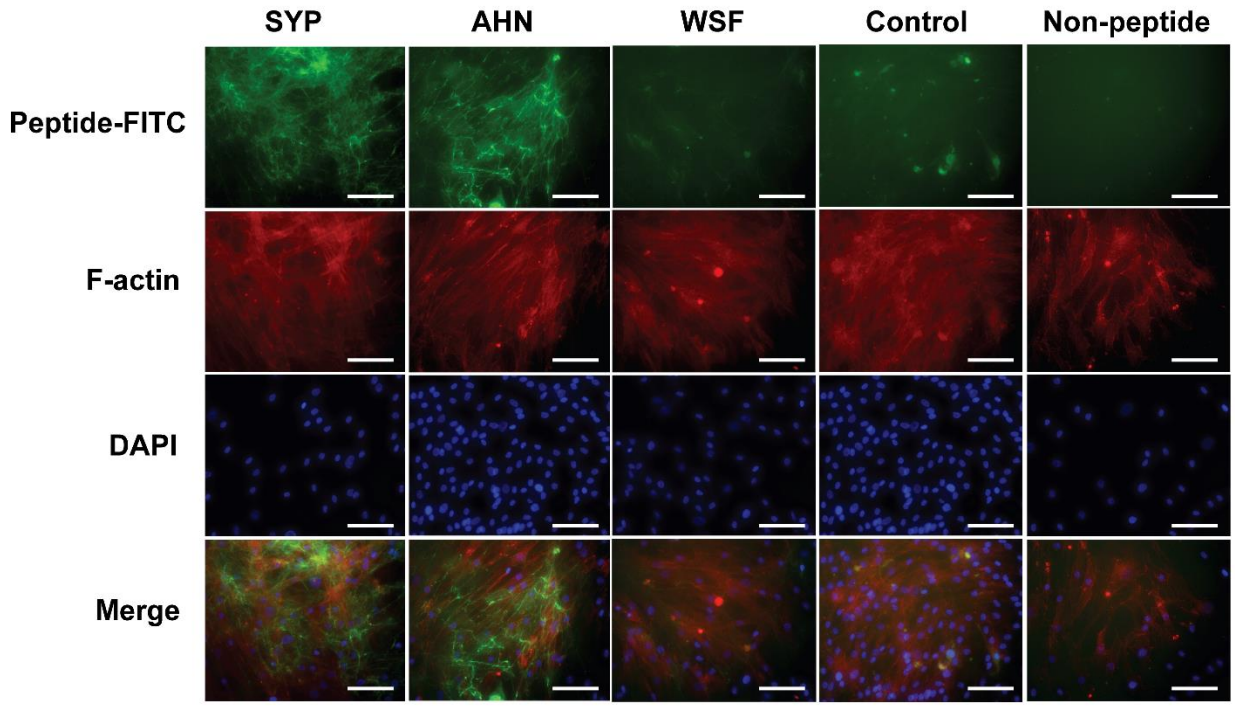

Figure 9. Fluorescent images of peptide incubation test. The SYP and AHN group had a stronger binding affinity compared to the WSF and control peptide group. The Green fluorescence overlapped with red fluorescence suggesting specific binding of these peptides. The non-peptide group was a negative control. Scale bar: 100 μm.

To answer this question, confocal microscopy (Leica) was employed to observe the cell-peptide binding location. CellMask™ Plasma Membrane Stains was applied to mark the cell plasma location. The section images (multiple cells) of the HDFs (Figure 10) and the single cell images (Figure 11) with a higher magnification were taken to qualify and quantify the binding affinity of the peptides as well as to observe the cell-peptide binding sites. To minimize signal

interference from neighboring cells, a lower cell density was used during the incubation. The green fluorescence was barely observed in the control peptide group, suggesting that the control peptide did not bind the HDFs. The AHN peptide showed the highest fluorescence intensity among the 3 binding peptides. The SYP and WSF have almost the same fluorescence intensity and both are weaker than the AHN group. When merged to cytoplasm staining, the AHN and SYP peptides were present both inside and outside the cells, and they aligned into a fibrous shape. However, the WSF group only showed an intracellular binding. According to the biopanning process, the phage displayed peptides could bind to the surface of the cells and then enter the cells by endocytosis. With the observed binding site differences on the cells, we believe that the targets for AHN and SYP existed both inside and outside of the cells. They first bound to the same component in extracellular matrix to land to the cells. Then, they were internalized into the cells and specifically bound to their own targets. The WSF may not have extracellular target and could have been randomly endocytosed by HDFs, so that it has lower intensity.

A fluorescence intensity quantification was performed to compare the affinity of HDF-binding peptides based on the section images. The average fluorescence intensity from multiple cells and the corresponding p-value were calculated by one-way ANOVA (Figure 12). The non-peptide group served as a negative control. The fluorescence intensity of AHN group was more than 2.5-fold higher than the SYP, WSF and control group, which were all higher than the non-peptide group (Figure 12a). This quantitative result is consistent with the fluorescence image data in Figure 10.

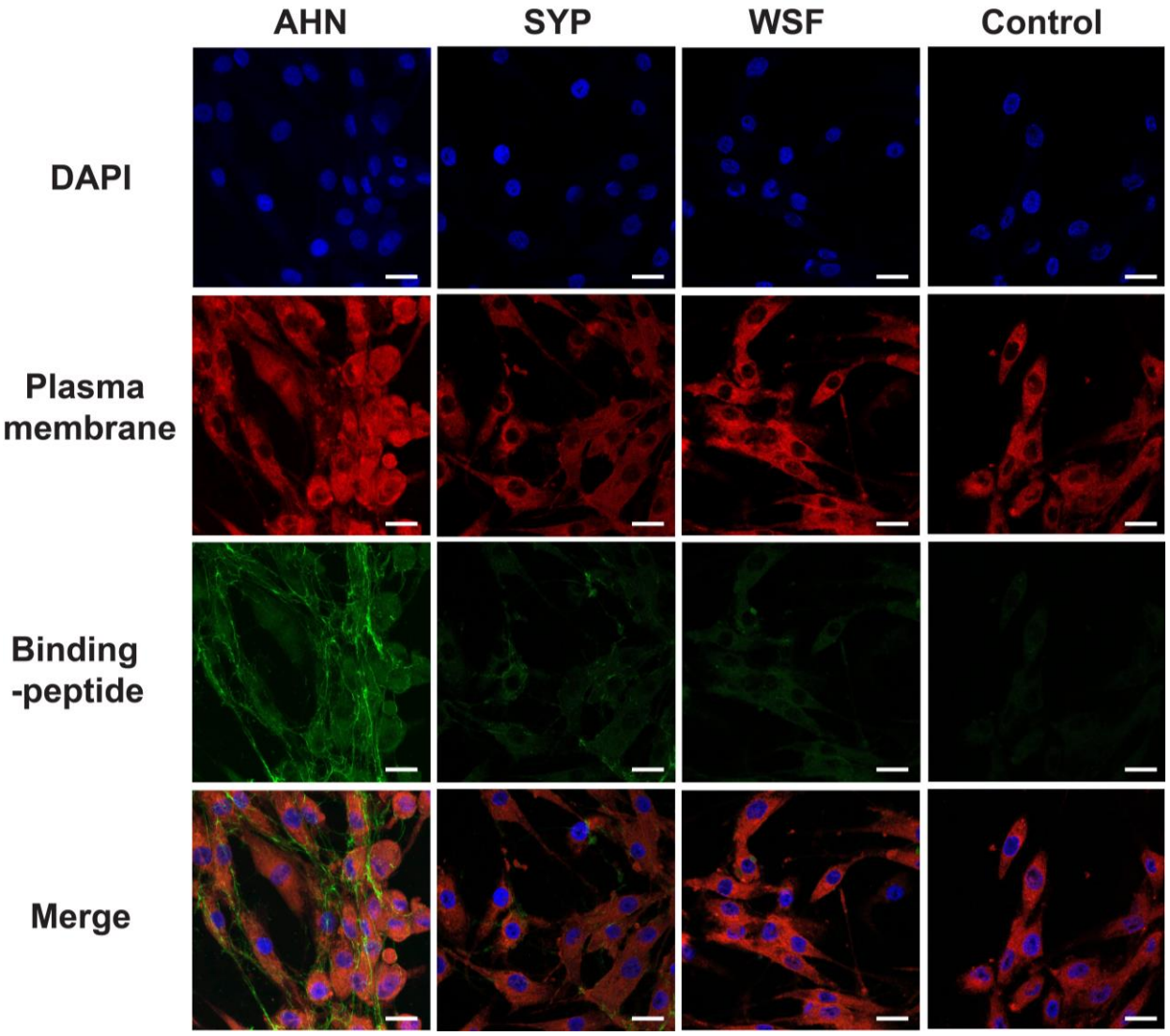

Figure 10. Confocal section images of the HDF-binding peptides. The AHN had the strongest fluorescence intensity among the 3 selected peptides. The SYP and WSF had a low binding affinity to the HDFs. Control peptide group barely showed the fluorescence signal. Scale bar: 25 μm.

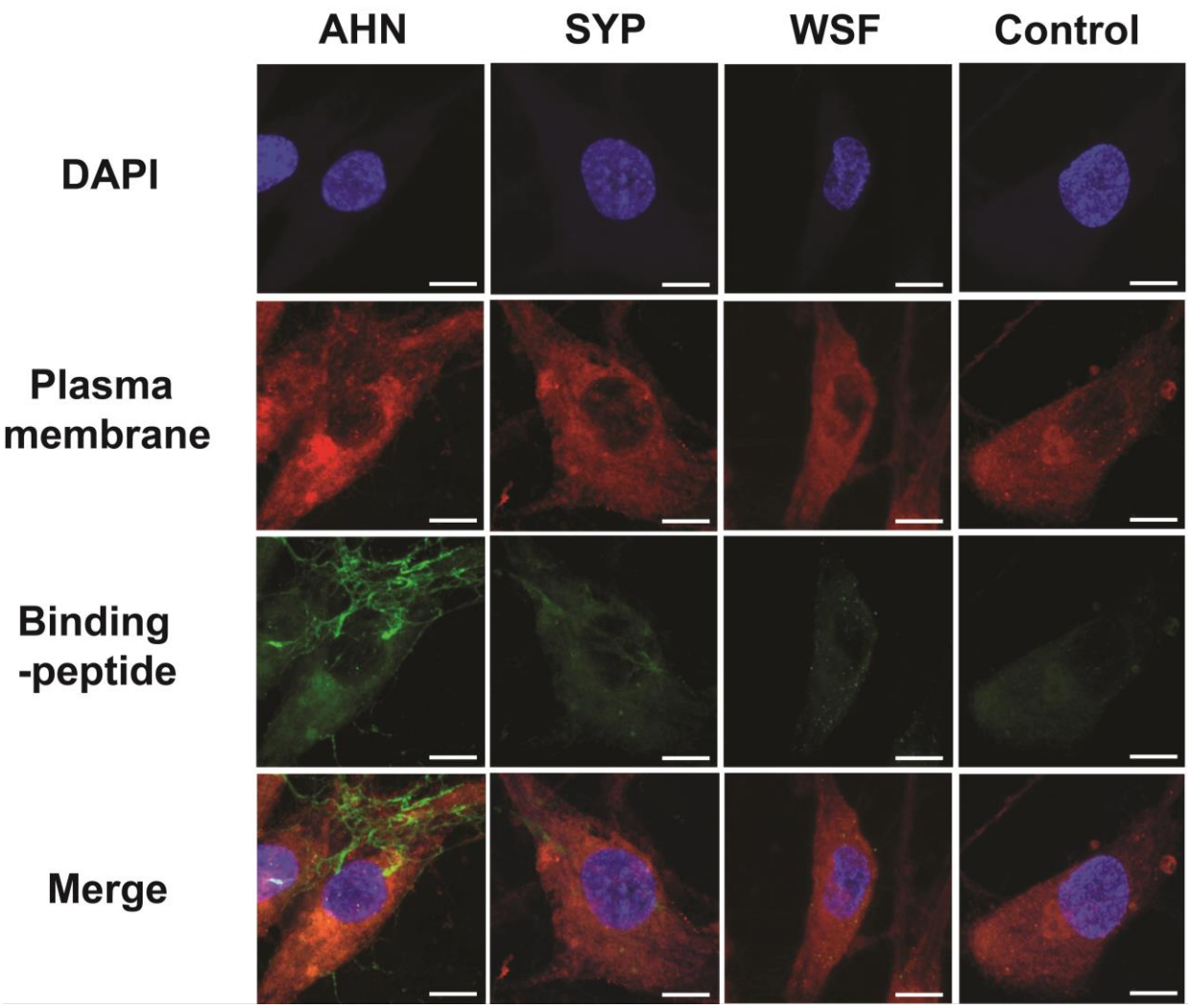

Figure 11. Single cell images of the HDF-binding peptides. The AHN has the highest fluorescence intensity among the 3 selected peptides. The fibrous structure appears at the cell junctions in the AHN group. Scale bar: 10 μm.

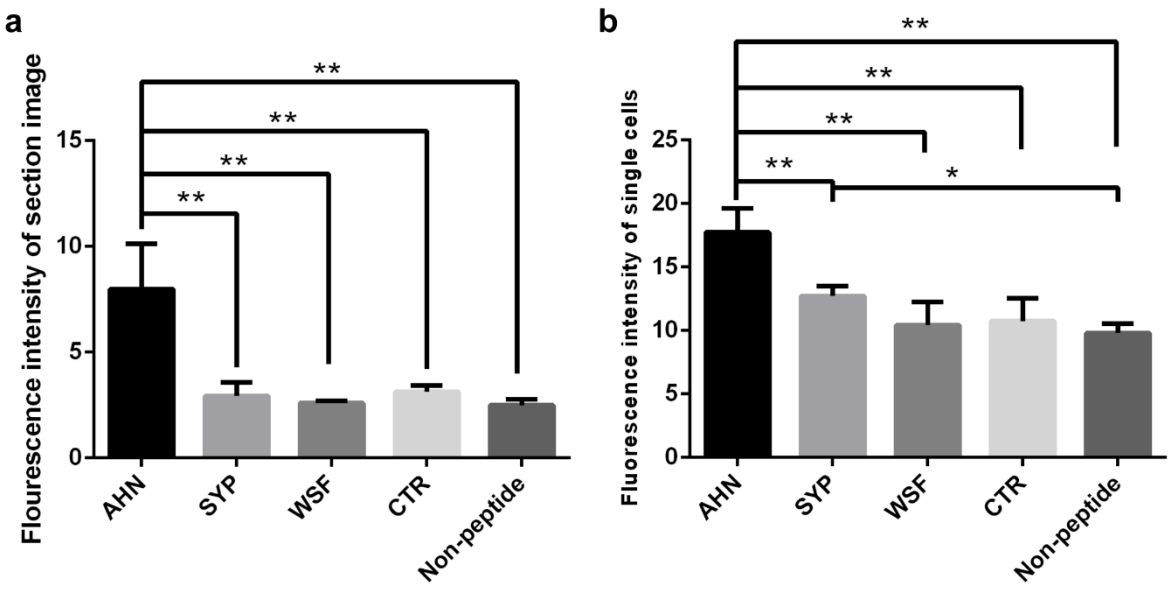

Figure 12. Fluorescence intensity of HDFs-targeting peptides. a) Fluorescence intensity on section images with multiple cells. The square tool was used to define the measured areas, where 6 cells were randomly selected based on their nucleus positions. Both intracellular and extracellular fluorescence intensity were measured on section images. The AHN had the highest binding affinity to the HDFs. The SYP and WSF didn't have significant differences compared to the control group and the non-peptide group. b) Fluorescence intensity on individual HDF cells based on single cell confocal images. The fluorescence intensity of the AHN peptide was significantly higher than other groups, which indicated a higher affinity in the target binding process. The results from both section and single cell images all suggested that the AHN was the best HDF-binding peptides among them all. **: $p<0.01$; *: $p<0.05$.

The section fluorescence intensity was measured based on the nucleus position of HDFs. It contained the cell body intensity and the fluorescence signal in the extracellular matrix. The final goal of this project was to use lipid-based nanoparticles (LBN) to deliver reprogramming

genes into the HDFs. The cell-surface binding of the peptides may improve the chance of endocytosis. However, the most important process of gene delivery was dependent on the successful internalization of the targeting peptides into the cells. To further confirm that the AHN peptide is the strongest internalizing peptide, the images of single HDF cells were taken and the fluorescence intensity within the cells was measured.

In single cell level, AHN still had the best binding affinity to the HDFs both visually and quantitatively (Figures 11, 12b). The fluorescence intensity of the AHN group was about 1.5-2 folds higher than other groups (Figure 12b). Besides, there was also a remarkable difference between the SYP group and the non-peptide group, but the SYP failed to show distinctly higher expression compared to the control peptide. In summary, AHN was the best HDF-binding peptides among 3 selected binding peptides and had a significant affinity difference from the control group and non-peptide group. Both AHN and SYP peptide were detected with extracellular binding at the junction of two neighboring cells (Figure 11). To further confirm that the fibrous structure was induced by specific binding between the HDFs and targeting peptides, rather than through peptide self-assembly, a drop of AHN-FITC solution was dropped on the glass slide and incubated for an hour. No fibrous structure was observed under the fluorescent microscope. This indicates that the AHN peptide couldn't self-assemble. The extracellular fibrous structures in AHN and SYP group appeared near the cell-cell junctions and the cell pseudopodia (Figure 10). The fibrous structure became more condensed in the areas where cells were contacting each other or trying to reach the adjacent cells with their pseudopodia. These junctions have been reported in the extracellular connection.[142]

In order to get a better understanding of the HDF-AHN extracellular and intracellular binding sites, the confocal images were used to generate a 3D image (Figure 13). It can be clearly seen that the peptide bound to a fibrous structure that existed both inside and outside of the cell. The fibrous structure went through the cell plasma and stretched along the long axis of the cell, which overlaps with the location of the cytoskeleton. It also grew along the edges of the cell body and connected to the adjacent cells. In Figure 13, it seems that some of the fiber has gone through the nucleus. To further observe the AHN binding sites around the nucleus, a video was made with multiple layered confocal images (Video 1). In the video, from the side view, the green fibrous structure didn't go through the nucleus, instead, it was on the surface of the nucleus and existed in cell plasma. Because the HDF cell was very thin (about 5 μm thick) under the confocal microscope, it looked like the AHN binding site was in the nucleus, however, it was very close to nucleus but still in cell plasma.

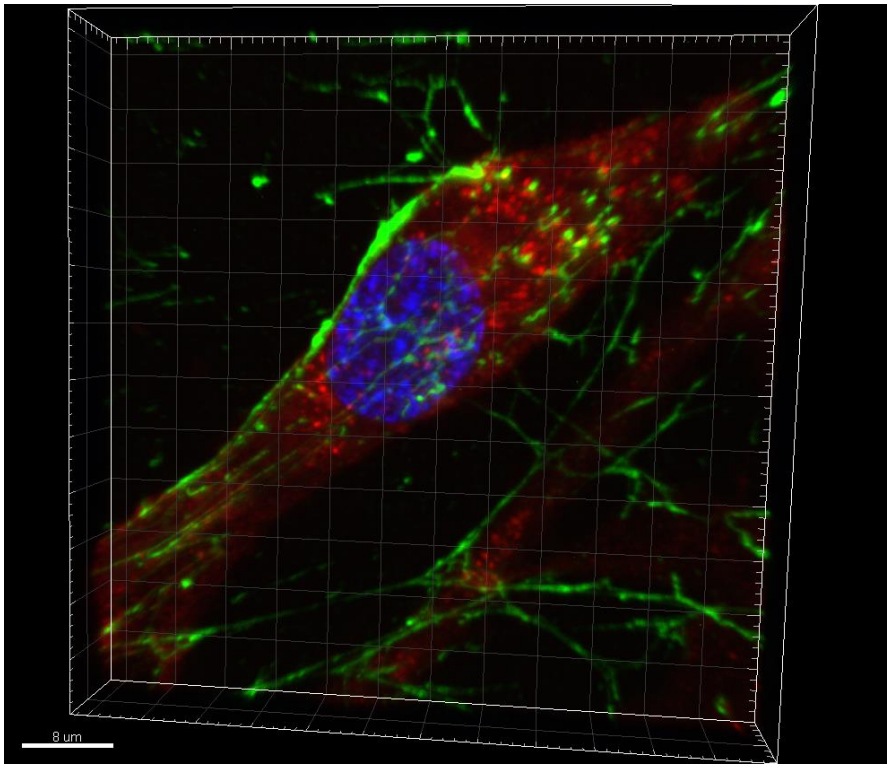

Figure 13. 3D confocal image showing HDF-AHN binding. Green fluorescence was FITC labeled AHN peptide. Red fluorescence was cell plasma membrane. DAPI was in blue. The fibrous shaped structure went through the cell body and parallel to the long axis of the cell. It existed inside the cell, along the cell membrane and connected two adjacent cells. Scale bar: 8 μm.

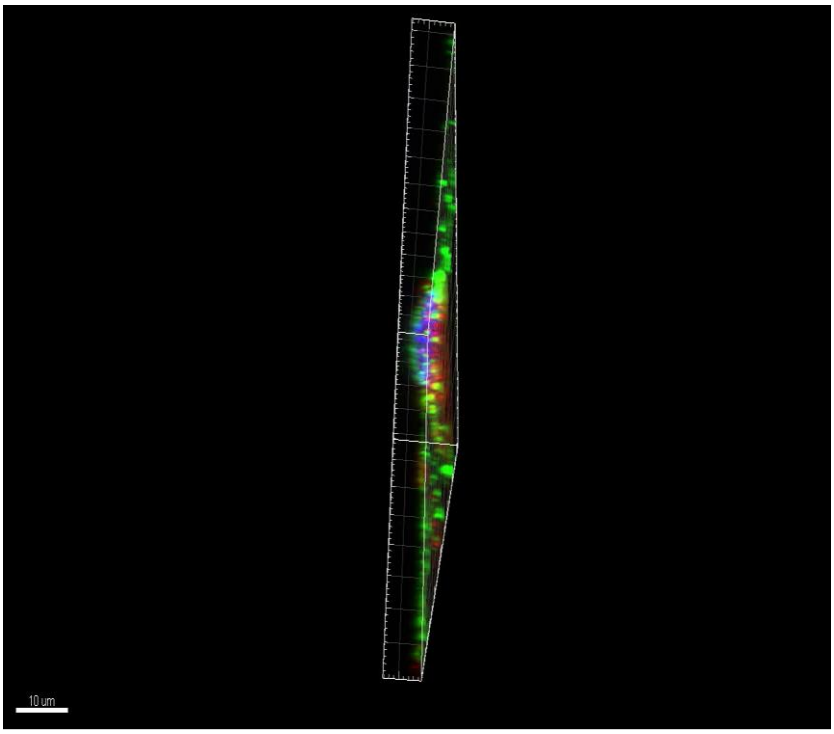

Video 1. Video showing the ANH peptide binding sites on HDFs. Please double click on the picture to play the video.

The specificity of the AHN peptide was also tested with multiple cell lines. MCF-7 cancer cell was used as a control cell to identify the binding specificity of AHN. The same amount of the AHN peptide was incubated with HDF and MCF-7 using the same protocol. In the control MCF-7 group, we didn't see any of the non-specific binding signals (Figure 14), which proved that the

biopanning selection process enabled screening for a highly specific binding process.These figures also proved that the AHN peptide didn't self assembly into filament structures. They bound to the proteins that secreated by HDFs.

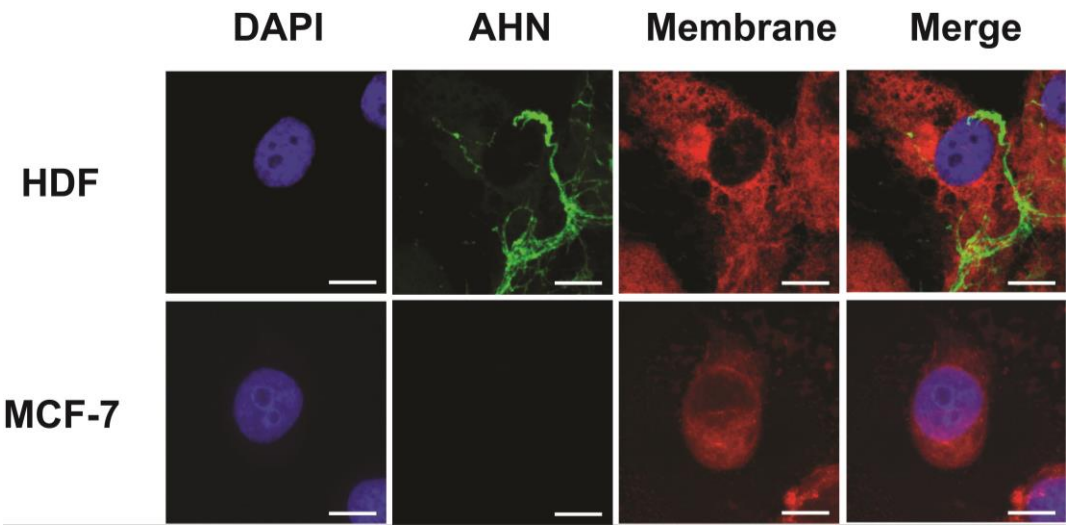

Figure 14. AHN peptide specificity test. The AHN peptide was strongly bound to HDFs and barely bound to MCF-7 cells, which indicated a high specificity of the HDF-targeting biopanning process. the Scale bar: 10 μm.

2.5 Conclusion

In summary, we discovered 3 HDF-internalizing peptides (SYPSNALSLHKY, AHNHTPIKQKYL, WSFGLPHSPQHL) via biopanning, tested whether these peptides were selected based on affinity or amplification advantages by RELIC, and then, identified the binding

affinity and specificity of these peptides via fluorescent images. The best targeting peptide we identified is AHNHTPIKQKYL. It has the highest affinity to HDFs among these 3 selected peptides and can only specifically target to HDFs.

In the future, I will chemically conjugate the AHNHTPIKQKYL peptide to the surface of a lipid-based nanoparticle. This peptide labeled nanoparticle will work as a carrier to deliver the CRISPR/Cas9 gene editing system and reprogram the HDFs into hiPSCs.

Chapter 3. Nanoridge-In-Microridge: A New Hierarchical Ordered Structure Assembled from Phage Nanofibers for Inducing Bidirectional Neural Differentiation of Stem Cells

3.1 Abstract

Hierarchically assembled nanomaterials can find a variety of applications in medicine, energy, and electronics. Here, an automatically controlled dip-pulling method is developed and optimized to generate an unprecedented ordered nano-to-micro hierarchical nanoridge-in-microridge (NiM) structure from a bacteria-specific human-safe virus, the filamentous phage with or without genetically displaying a foreign peptide. The NiM structure is pictured as a window blind with each lath (the microridge) made of parallel phage bundles (the nanoridges). It is independent of the substrate materials supporting it. Surprisingly, it can induce the bidirectional differentiation of stem cells into neurons and astrocytes within a short time frame (only 8 d) not seen before, which is highly desired because both neurons and astrocytes are needed simultaneously in treating neurodegenerative diseases. Since phages can direct tissue regeneration,

template materials formation, sense molecules, and build electrodes, the NiM structures displaying different peptides and on varying materials hold promise in many technologically important fields.

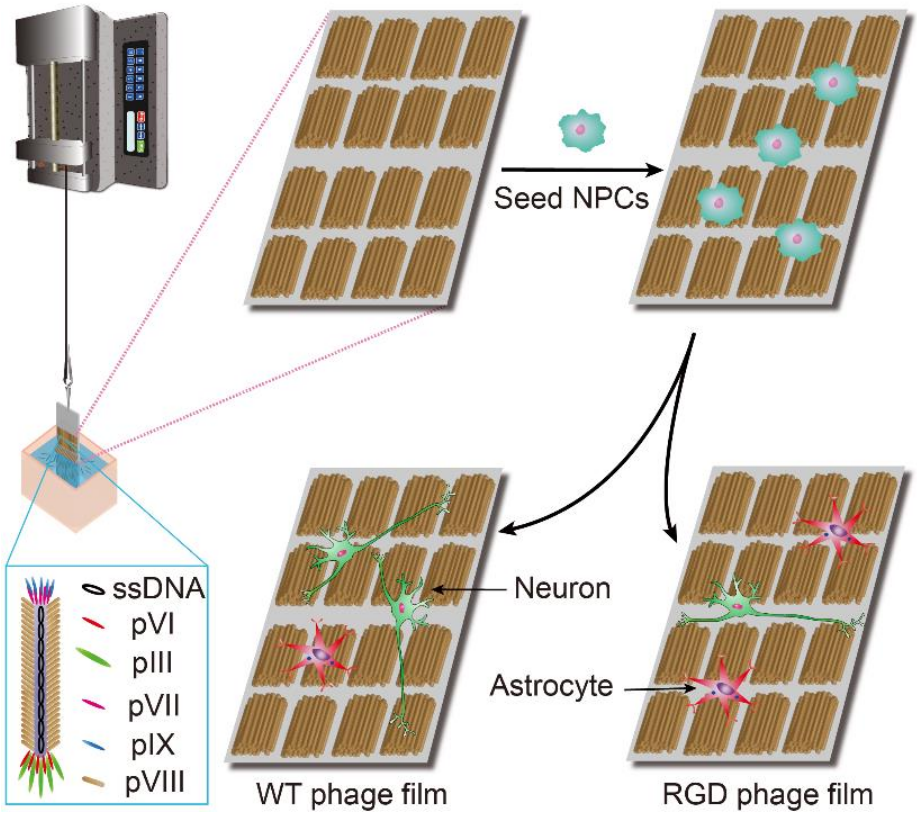

Figure 15. HiPSC-derived NPCs differentiated on NiM phage film structure. A dip-pulling method is developed to form a highly ordered hierarchical phage film with an unprecedented nanoridge-in-microridge structure on the substrate.This phage structure is found to induce the stem cells to differentiate into neurons and astrocytes without additional inducers.

3.2 Introduction

Hierarchically assembled nanomaterials can find a variety of applications in medicine, energy and electronics. Here an automatically-controlled dip-pulling method was developed and optimized to generate an unprecedented ordered nano-to-micro hierarchical nanoridge-in-microridge (NiM) structure from a bacteria-specific human-safe virus, the filamentous phage with or without genetically displaying a foreign peptide. The NiM structure is pictured as a window blind with each lath (the microridge) made of parallel phage bundles (the nanoridges). It was independent of the substrate materials supporting it. Surprisingly, it could induce the bidirectional differentiation of stem cells into neurons and astrocytes within a short timeframe (only 8 days) not seen before, which is highly desired because both neurons and astrocytes are needed simultaneously in treating neurodegenerative diseases. Since phages can direct tissue regeneration, template materials formation, sense molecules, and build electrodes, the NiM structures displaying different peptides and on varying materials hold promise in many technologically important fields.

Hierarchical structures, either natural or artificial, can find potential applications in medicine, energy and electronics.[143] Nature has produced biological materials with nano-to-micro hierarchical structures such as diatoms and bone.[143] However, it is still a daunting challenge to fabricate nano-to-micro hierarchical structures in the laboratory. Hence, we aimed to develop an unprecedented hierarchical structure and demonstrated one of its applications in serving as a matrix to induce the bidirectional neural differentiation of stem cells. The bidirectional neural differentiation of stem cells into neurons and astrocytes is desired because both neurons and

astrocytes are the building blocks of the human brain and thus are needed simultaneously in treating neurodegenerative diseases (NDDs) such as Parkinson's disease (PD) and Alzheimer's disease (AD).

Hence, there is a pressing need to simultaneously regenerate both neurons and astrocytes to advance the NDD treatment[144] and to generate a coculture model for studying the interactions between both cells.[145-147] Computational digital implementation modeling[148] and neuron-astrocyte coculture[145, 147] were used to study the neuron-astrocyte interactions. So far, there have been very limited studies on the use of nanomaterials to generate a neuron-astrocyte coculture model.[149, 150] Moreover, these studies used rodent cells to generate the neuron-astrocyte co-culture. Though the rodent cells functioned similar to human cells, human cells should be more reliable when it comes to developing seed cells for treating the NDDs. There are some coculture methods involved in rodent astrocytes and human neuronal cells.[145] However, those cells are from different sources[151] and may cause incompatibility. Thus, generating neurons and astrocytes from the same human cell source will facilitate the development of NDD treatment strategies.

Stem cells have the ability to differentiate into many types of cells. They can be used to solve the problem associated with the species difference in the traditional coculture method[151, 152] and are a new promising cell source to cure NDD.[153, 154] Stem cells such as neural stem cells (NSCs) or neural progenitor cells (NPCs) are the direct source for neural differentiation, but the only tissue source for NSCs or NPCs is human fetal brain tissue. Thus using the tissue source to generate neurons and astrocytes presented ethical issue.[155] Human induced pluripotent stem cells

(hiPSCs) or NPCs derived from them are the new cell sources for tissue regeneration.[11, 153] They can differentiate into all types of cells and thus used to develop patient-specific stem cell therapy while bypassing the ethical issues. Nowadays, hiPSCs based stem cell therapy has become one of the most promising NDD treatments. The behaviors of hiPSCs, especially their differentiation,[97] were strongly influenced by their microenvironment.[156] A material can serve as a matrix for providing a microenvironment to modulate their differentiation. However, so far, a material has only been used to generate either neurons[157] or astrocytes[158] from a single cell source. To the best of our knowledge, almost no study has been dedicated to the use of a material to achieve the regeneration of both neurons and astrocytes from a human cell source such as NPCs derived from hiPSCs although both cells are needed for treating NDDs.[159, 160]

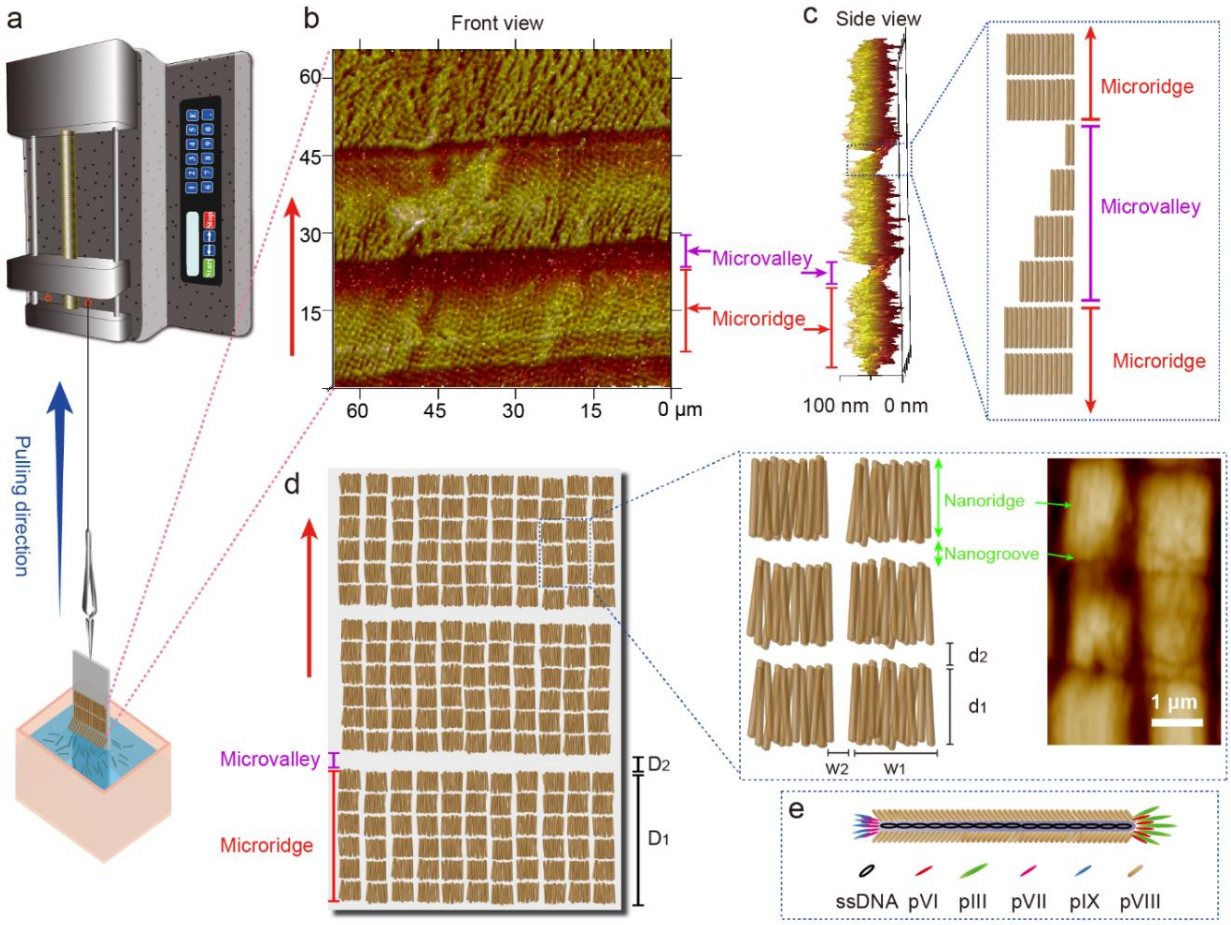

Figure 16. Self-assembly of phages into hierarchical nanoridge-in-microridge (NiM) structures by a dip-pulling method. a) Schematic illustration of the dip-pulling method. In this method, a substrate (e.g., glass slide) coated with positively charged polylysine was dipped into a phage solution and then vertically pulled out of the solution at a certain speed by a syringe pump. Under certain conditions (phage solution concentrations, pulling speeds, evaporation rates, pH values, and salt concentrations), this method generated a phage film with a nanoridge-in-microridge (NiM) structure. In the NiM, phages were parallel to the pulling force direction and became ordered into the parallel-aligned nanoridges that were further hierarchically assembled into the parallel microridges. The nanoridges (with a length of *d*1) were separated by nanogrooves (with a width of *d*2) and as wide as the length of phages (≈1.2 μm for wild-type phage and ≈550 nm for

engineered phage). b) Front view and c) side view of the NiM phage film structure by AFM imaging. The side view (c) of the NiM shows the presence of a microvalley in between microridges with the microvalley made of phage layers of decreasing thickness. d) Schematic of the NiM structures by dip-pulling method and high magnification of the nanoridge and nanogroove structure by AFM image. *D*1 and *D*2 are the width of microridges and microvalleys, respectively. *d*1 and *w*1 are the length and width of the nanoridges, respectively. *d*2 and *w*2 are the size of the nanogrooves between the nanoridges along and perpendicular to the pulling direction, respectively. The nanoridges were organized into microridges separated by the microvalleys. Each nanoridge is just a bundle formed by parallel-aligned phages, and thus *d*1 should be theoretically the length of a phage nanofiber. e) schematic of a single phage. Red arrows denoted the pulling force direction. The AFM images show that the NiM film was assembled from wild-type phages with a concentration of 1×10^{14} pfu/ml by the dip-pulling method at pulling speeds of 1.5 μm/s (c) and 0.5 μm/s (b,d).

Hence, we proposed to develop a nano-to-micro hierarchical structure (termed nanoridge-in-microridge, NiM, Figure 16b-d) from filamentous M13 phage, by a novel method termed dip-pulling (Figure 16a), and then employed the NiM structures to induce the bidirectional differentiation of hiPSC-derived NPCs into both neurons and astrocytes (Figure 16). It should be noted that hiPSCs didn't adhere to the phage films (probably due to the formation of suspended cell clusters called embryonic bodies during their differentiation into NPCs). However, the NPCs derived from them did not form the suspended clusters but adhered well to the phage films. Thus, the NPCs were first derived from hiPSCs (Figure 17) and then cultured on the NIM structures to achieve the bidirectional differentiation of NPCs in the absence of additional differentiation

inducers, because the NIM structures presented unique nanotopography. Moreover, we found that the NiM structures could be formed virtually on any type of material.

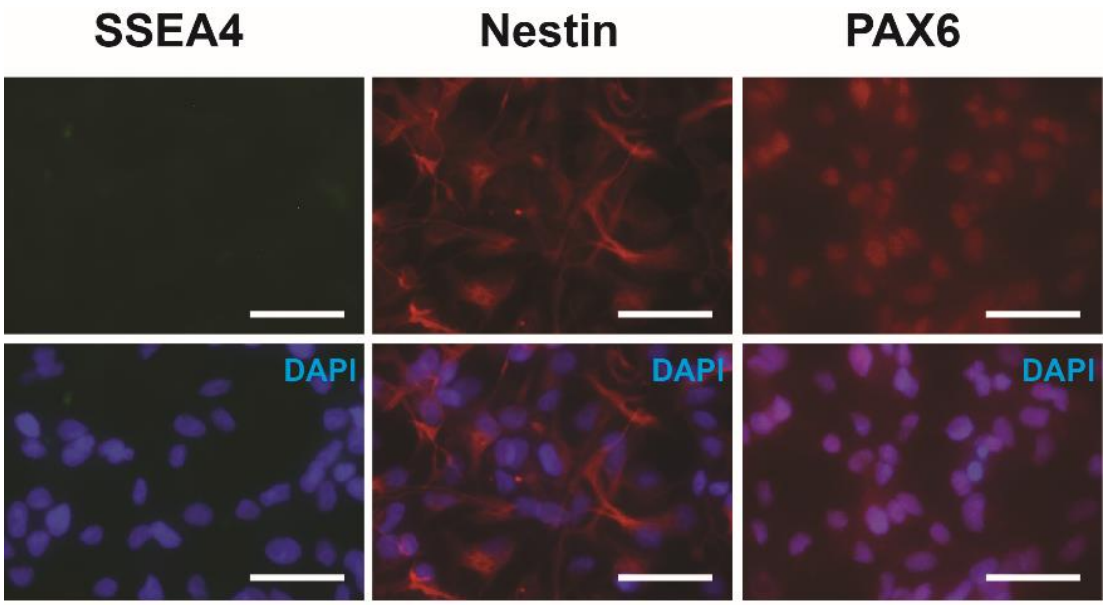

Figure 17. Confirmation of conversion of hiPSCs into NPCs. After 21 days of culture in Neural induction medium (Stemcell Tech.), hiPSCs were successfully differentiated into NPCs. SSEA4 is a pluripotent marker, and Nestin and PAX6 are NPC markers. Scale bar: 50 μm.

3.3 Materials and Methods

3.3.1 Phage amplification and purification

The E. coli K12 ER2738 (NEB) strain and its engineered strain were used to produce both WT-phage and RGD-phage, respectively. The bacteria were incubated at 37°C with overnight shaking. The M13KO7 helper phage (NEB) was added into the overnight bacteria solution and incubated for 1 h. Then the mixture of phage and bacteria was transferred into a small flask and shaken for 3 h to allow phage to infect bacteria. Chloramphenicol antibiotics (50 μg/ml) was used to select the RGD-phage in this step. The product was subsequently transferred into 1 L LB broth and shaken for 24 h at 37°C. Kanamycin (70 μg/ml) was used to select the phage infected bacteria and IPTG was used to induce RGD phagemid expression. The resultant RGD-phage or WT-phage was separated from bacteria by centrifugation. The PEG-NaCl solution (16.7% PEG/3.3 M NaCl) was added to the supernatant to induce phage precipitation at 4°C overnight. Water was added to resuspend the precipitated phages. The above precipitation and suspension steps were repeated one more time for phage purification. The final phage solution was dialyzed against ddH2O overnight for further use. A nanophotometer was used to detect the phage concentration.

3.3.2 Phage film fabrication by dip-pulling

The polylysine coated glass slides or coverslips were dipped into dialyzed phage solution and pulled from the solution at different speeds, which was controlled by a syringe pump (Stoelting). In evaporation change experiment, the normal evaporation rate was under room

temperature and the fast evaporation rate was applied in the chemical fume hood. Salt concentrations of the phage solutions were adjusted by adding NaCl solution. The pH values of the phage solutions were controlled by using buffers of different pH values (Table 4). The surface structures of the resultant phage films were confirmed by an Atomic Force Microscope (Bruker) and Optical Microscope (Nikon).

Table 4. Buffers used for achieving different pH values.

pH value	Buffer
5.0	HAc-NaAc
6.0	Na_2HPO_3-NaH_2PO_3
9.0	Na_2CO_3-$NaHCO_3$
10.0	Na_2CO_3-$NaHCO_3$
11.0	Na_2CO_3

3.3.3 Polylysine treatment on different substrates

Flat substrates of gold, titanium and stainless steel were dipped in polylysine solution (0.01%) for 10 min at room temperature (RT), whereas polycarbonate plastic slide and silicon were

incubated in 0.01% polylysine solution overnight at RT to form polylysine coatings. Phage film fabrication steps were the same as glass slides.

3.3.4 Cell culture

HiPSCs (ALSTEM, Inc.) were cultured using a reported feeder-free protocol.[161] Firstly, Matrigel (corning) was used to prepare a feeder layer. Matrigel was diluted into 10 mg/ml in knockout-DMEM/F12 medium (Thermo fisher) and the diluted solution was added to the cell culture plates to form feeder layer, which were incubated at 37 °C for 1 h. The hiPSCs were seeded on the plates or films and the mTeSR1 medium (Stemcell tech) was changed daily to maintain their pluripotency. They were differentiated into NPCs according to the company's (Stemcell Tech) monolayer culture protocol. Briefly, the hiPSCs were dissociated into single cells, seeded on Matrigel-coated plates with a density of 1 $x10^6$ cells/mL and incubated at 37 °C with 5% CO_2. The STEMdiff™ Neural Induction Medium (Stemcell Tech) was changed daily to differentiate hiPSCs into NPCs. After 3 passages, the NPCs were maintained in the STEMdiff™ Neural Progenitor Medium (Stemcell Tech) for further use.

3.3.5 Cell culture on phage films

Phage films were exposed to UV light for 4-6 h for sterilization. The sterilized phage films were pre-treated with laminin at 37 °C for 1 h to form laminin coating. The hiPSCs-derived NPCs were seeded on the laminin coated-phage films and cultured in the STEMdiff™ Neural Progenitor medium. The medium was changed on the daily basis.

3.3.6 RT-qPCR

The NPCs on the phage films were harvested at different time points (10 coverslips for each group). They were digested by accutase and then resuspended in cold PBS. Cells (10^5 cells) were counted as a separate bio-repeat. The Power SYBR Green Cells-to-Ct Kit (Thermo fisher) was used to perform the RT-qPCR. Briefly, the harvested cells were lysed by lysis solution for 5 min at RT first. The lysate was then used for reverse transcription in the thermal cycler according to Table 5. The reverse transcript cDNAs were use as templates in the real-time PCR step. In real-time quantitative PCR, 5 genes were tested: Nestin, TBB3, MAP2, GFAP and Olig2. However, there is no obvious expression in Olig2. Primers for each gene were listed in Table 6. 3-4 bio-repeats were used at different time points for cells cultured on the WT-phage films, RGD-phage films and control substrate (no phage).

Table 5. Steps for reverse transcription

Step	Temperature	Time
Reverse transcription	37 °C	60 min
Enzyme inactivation	95 °C	5 min
Hold	4 °C	forever

Table 6. Primers for RT-qPCR.

Gene	Primer sequence
Nestin	Forward: 5'-GCTCCAAGACTTCCCTCAGC-3'
	Reverse: 5'-TGGCACAGGTGTCTCAAGG-3'
TBB3	Forward: 5'-TGGAGAACACGGATGAGACC-3'
	Reverse: 5'-GGCATGAAGAAGTGCAGGC-3'
MAP2	Forward: 5'-CTGACAGAGAAACAGCAGAGG-3'
	Reverse: 5'-ACAGTCTGTTCTGAGGCAGG-3'
GFAP	Forward: 5'-CTGGAACAGCAAAACAAGG-3'
	Reverse: 5'-GATTGTCCCTCTCAACCTCC-3'
Olig2	Forward: 5'- CAAGCTTTCCAAGATCGCC-3'
	Reverse: 5'-GATTGTCCCTCTCAACCTCC-3'

3.3.7 Immunofluorescent staining and intensity analysis

Paraformaldehyde (4%) was used to fix the cells for 20 min at RT after PBS washing (3 times) steps. The cells were treated with Triton X-100 (0.3%) at RT for 5 min to allow for the penetration of the cell membrane. After penetration, BSA (10%) was used for blocking for 1 h at

RT. Then, the cells were incubated with the primary antibody specific for Nestin (1:200 dilution), MAP2 (1:500 dilution), GFAP (1:5000 dilution) (Abcam) and βIII-Tubulin (1:500 dilution) (Thermofisher) overnight in BSA (3%) solution. The secondary antibodies (Goat Anti-Mouse IgG H&L, Goat Anti-Chicken IgY H&L, Goat Anti-Rabbit IgG H&L*)* were labeled with Alexa Fluor® 488 and Alexa Fluor® 555 (Abcam). DAPI was incubated with the cells to stain the nucleus for 15 min at RT. The stained cells were fluorescently imaged. The average immunofluorescent intensity of the cells was analyzed by Image J, which was based on randomly selected ten cells in about 5 images.

3.3.8 Statistical analysis

One-way ANOVA and Tukey's test were adopted to perform statistical analysis. Different substrate groups were compared with a p value less than 0.05, 0.01, 0.001, or 0.0001 considered significantly different.

3.4 Results and discussion

Filamentous M13 phage is a human-safe bacteria-specific viral nanofiber (Figure 16e) that is made of a sheath of coat proteins encapsulating a circular ssDNA.[162] The side wall of the nanofiber is assembled from ~3000 copies of a major coat protein (termed p8). We used two types of M13 phage in this work, one is the wild-type phage (termed WT-phage) and another is the engineered phage (termed RGD-phage) with the side wall displaying RGD (through fusion of RGD

to N-terminal of p8 by genetic means reported by us previously).[162] Both WT-phage and RGD-phage are nanofibers (~7 nm wide) with a negatively charged protein shell.

3.4.1 Discovering nanoridge-in-microridge (NiM) phage film structures

To establish and optimize the dip-pulling method, we employed WT-phage simply because WT-phage could be amplified by infecting bacteria more efficiently than RGD-phage and both phages do not show difference in phage assembly in the dip-pulling. It should be noted that WT-phage (~1.2 μm long) is longer than RGD-phage (~550 nm long). It is known that displaying a peptide on the side wall of M13 phage shortens the phage.[163] Our dip-pulling method was designed as a one-step operation (one dipping & one pulling) under automatic control to avoid the irreproducibility commonly seen in manual or multi-step operation. Namely, a glass slide pre-coated with positively charged poly-lysine was dipped into a monodisperse phage solution, and then vertically pulled out of the solution at a stable speed controlled by a syringe pump (and thus avoiding manual operation).

During the dip-pulling process, the positively charged poly-lysine coated glass slide attracted negatively charged phages to its surface and the phages were parallelly aligned into a unique hierarchical NiM structure along the pulling direction (Figure 16b-d). Such NiM structure has never been reported before and is significantly different from reported alignment of bionanofibers.[97, 164-167] The nanoridged pattern in the hierarchical structure looked like a window blind with each lath (the microridge) made of nanoridges (assembled from parallel-aligned phages). The NiM showed a periodic pattern at both nano- and micro- structure. At the microscale,

microridges were parallel to each other with microvalleys in between the neighboring ones. The microvalleys were made of phage bundles with decreasing thickness along the pulling direction (Figure 16c). At the nanoscale, each microridge is made of many parallel nanoridges separated by nanogrooves (Figure 16d). Each nanoridge is assembled from parallel phages and is as wide as the length of an individual phage. In such structure, phage nanofibers are always aligned along the pulling force direction, probably because they have the smallest hydrodynamic interactions with fluid in the shear force direction.[168] We found that the NiM structure was only formed under certain conditions after we carried out a series of experiments optimizing these conditions, including the pulling speeds, phage concentrations, salt concentrations and pH values. Although we have not fully understood the NiM formation mechanism, we believe that it is related to the solvent evaporation at the meniscus of air-fluid-solid interface moving along the pulling force. It is very likely that the phage solution reaches a concentration higher than the critical concentration (4 x 10^{15} pfu/ml) for forming a smectic liquid crystal phase at the meniscus.[169]

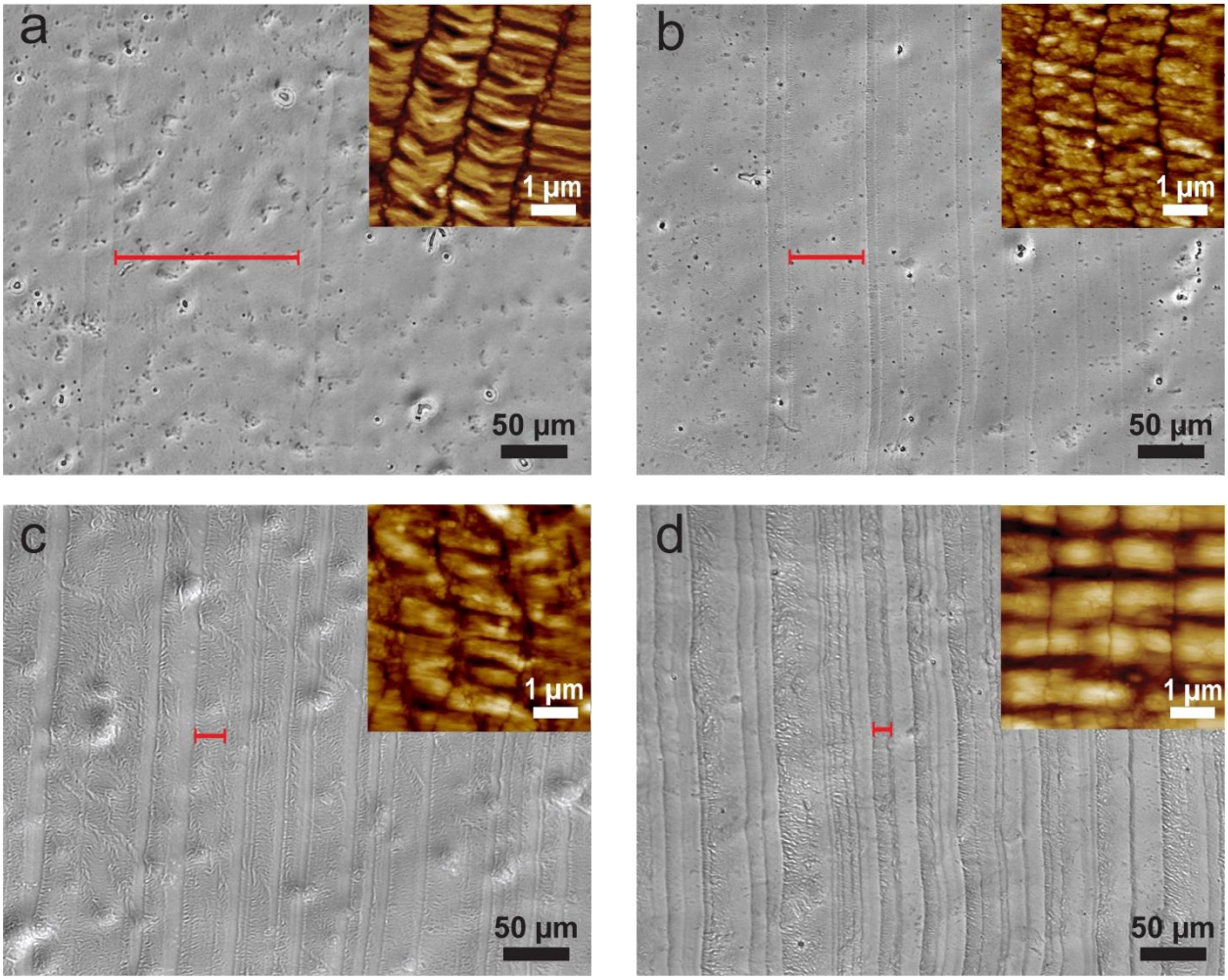

Figure 18. Surface morphologies of ordered phage films assembled from a phage solution (1×10^{14} pfu/ml) at different pulling speeds by the dip-pulling method. The surface morphologies were observed by a bright field optical microscopy imaging at a low magnification and by AFM imaging at a high magnification (shown as insets). a–d) The optical imaging of the film structures at different pulling speeds: a) 10 μm/s; b) 4 μm/s; c) 1.5 μm/s; d) 0.5 μm/s). The red bar on the images indicated the average width (D1) of the microridges at different speeds. As the speed decreased, the width (D1) of the microridges became smaller.

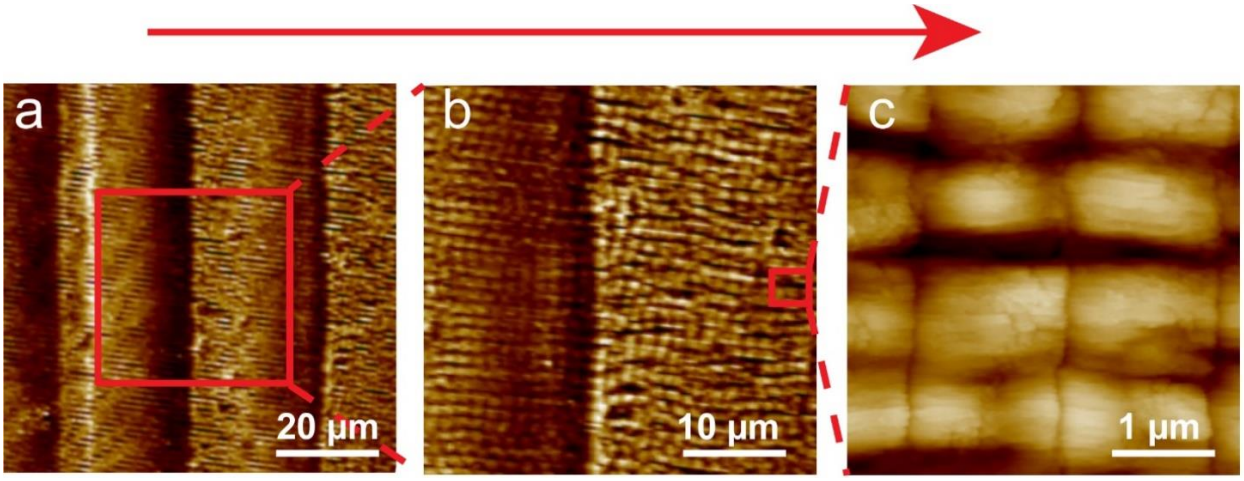

Figure 19. AFM images of a NiM structure at different magnifications showing the microridges/microvalleys and nanoridges/nanogrooves (schematically shown in Figure 3.2d). The red arrow denotes the pulling force direction.

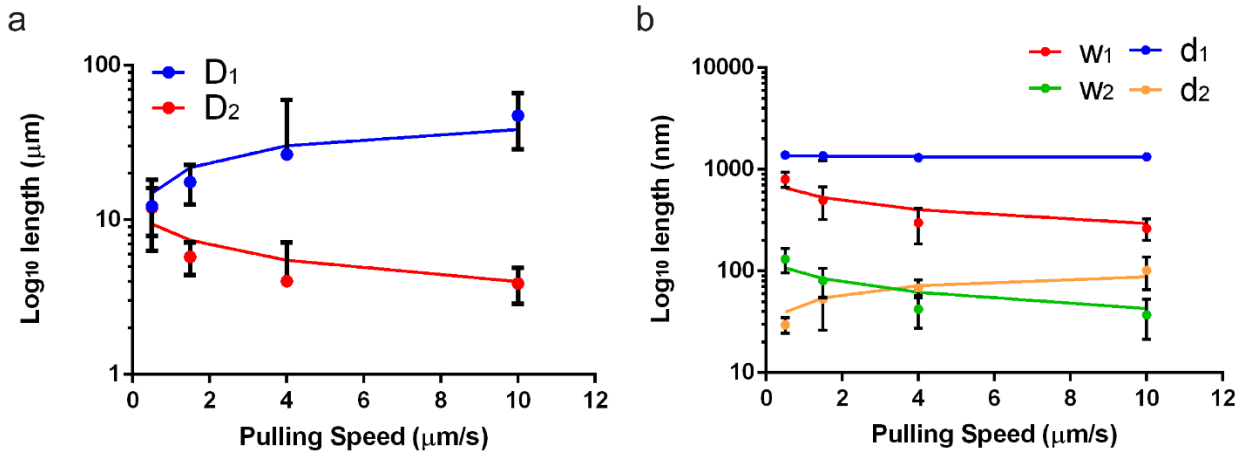

Figure 20. Relationship between the pulling speed and the six size parameters of the NiM (D1, D2, w1, w2, d1, d2). The length of d1 didn't change with the speeds because it reflects the phage length, while the other five factors showed an increase (D1, d2) or a decrease (D2, w1, w2).

3.4.2 NiM structure under different conditions

NiM structures were consistently formed at different pulling speeds (10 μm/s, 4 μm/s, 1.5 μm/s, and 0.5 μm/s, with 1 x 10^{14} pfu/ml phage solution), as confirmed by AFM (Figure 18 & 19). However, some size parameters of the nanoridges/microridges and the nanogrooves/microvalleys are different. To better understand the effect of pulling speeds on these size parameters, we define six size parameters as shown in Scheme 1, which were determined by a combination of 3 AFM images for each speed. D_1 and D_2 are the width of the microridges and microvalleys, respectively. d_1 and w_1 are the length and width of the nanoridges, respectively. d_2 and w_2 are the size of the nanogrooves between the nanoridges along and perpendicular to the pulling direction, respectively (Figure 16d). Because each nanoridge is actually just a bundle formed by lateral aggregation of parallel-aligned phages, d_1 should be the length of a phage nanofiber. This is confirmed by our finding that d_1 was nearly constant and independent from the pulling speed change (Figure 20b). However, with the increase in the pulling speed, D_1 and d_2 were increasing whereas D_2, w_1 and w_2 were decreasing (Figure 20). The effect of periodic pulling speeds (10 μm/s and 0.5 μm/s) on the phage film formation was also studied (Figure 21). We found that d_1, w_1, and w_2 were nearly not affected by the periodic speed change. However, D_1 and d_2 still followed our predictied trend in Figure 3-6 under both speeds; their values on the higher speed side are larger than those on the lower speed side (Figure 21). On the speed bundary line, we can see a sudden change on the nanostructures when a speed was changed to another one (Figure 21c). On the fast speed side (10

μm/s), the nanoridges tended to become bent along the pulling direction, while on the slow speed side (0.5 μm/s), the nanoridges appeared to be straighter.

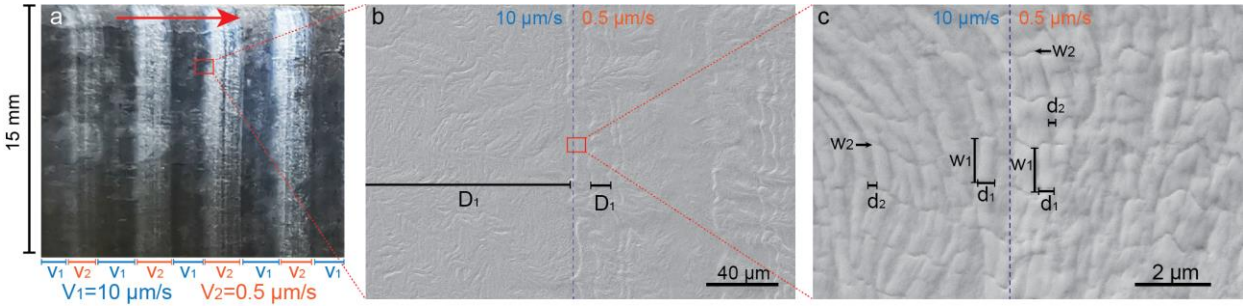

Figure 21. Optical and SEM image of RGD-phage film formation under periodic pulling speeds. (a) Optical image of the film formed when a polylysine treated glass slide was vertically pulled out of the phage solution under periodic pulling speeds (10 μm/s and 0.5 μm/s). (b) SEM image of the highlighted area in the rectangle in (a). (c) SEM image of the highlighted area in the rectangle in (b). Both (a) and (b) showed that the width of the microridges (D1) and nanogrooves (d2) increased with the speed increase while other size parameters were nearly unaffected by the speed changes. It should be noted that in some areas of the low speed side, d2 (the nanogroove size) became very small, making two neighboring nanoridges seem to be nearly linked. Blue lines indicated the speed boundaries. Red arrow indicated the pulling direction (Phage concentration, 1 x 10^{14} pfu/ml).

We then investigated the effect of evaporation rates on the phage film formation. We found that the best evaporation condition for NiM structure formation was the normal room condition at the room temperature. When the dip-pulling was operated inside a chemical fume hood to

accelerate the evaporation, we found that the NiM structure was disturbed at the microscales (Figure 22). Comparing to the normal room evaporation, the distribution of the microridges and microgrooves was not uniform under the fast evaporation. Moreover, under the fast evaporation, microridge width D_1 significantly decreased. However, the nanoridge structures stayed the same under different evaporation conditions.

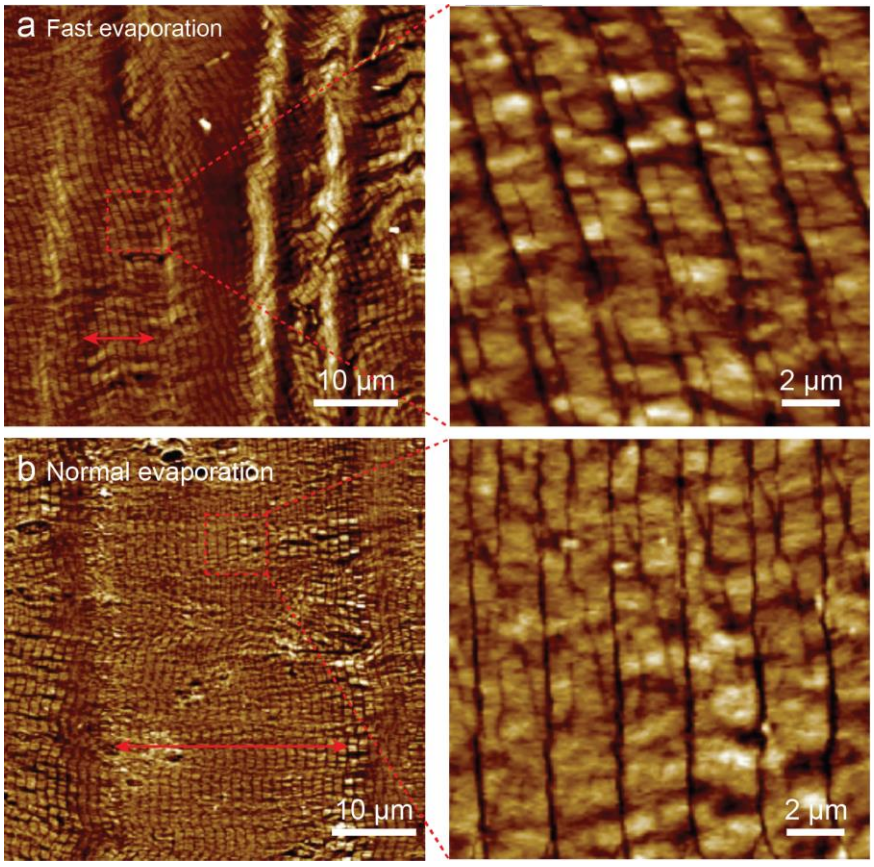

Figure 22. Surface morphologies of phage films assembled from wild-type phages at different evaporation rates by the dip-pulling method. (a) Phage film structure formed under the fast evaporation

rate in a chemical fume hood. (b) Phage film structure formed under the normal room condition. Red arrows indicated the microridge width D_1. (Phage concentration, 1 x 10^{14} pfu/ml; pulling speed, 1.5 μm/s).

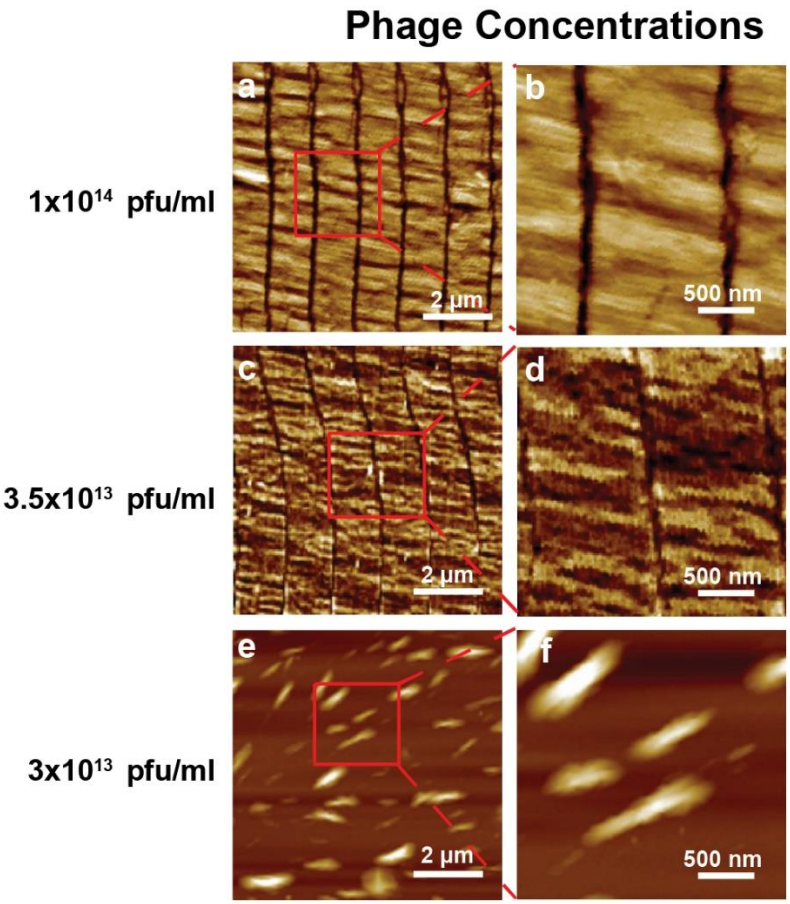

Figure 23. Surface morphologies of wild-type phage films assembled from wild-type phages at different phage concentrations by the dip-pulling method. Phage concentration manipulates the phage film formation. The phages were assembled into similar ordered nanoridged patterns when

their concentration was higher than 3.5×10^{13} pfu/mL, below which such patterns were not formed. Pulling speed, 1.5 μm/s.

We then studied the effect of the phage concentrations on the NiM structure formation. Different concentrations of phage solutions, ranging from 1 x 10^{13} pfu/ml to 2 x 10^{14} pfu/ml, were proved to *a*ffect the phage film structures at a pulling speed of 1.5 μm/s. The concentration changes of the phage solutions didn't disturb the NiM structure and the six sizes parameters (D_1, D_2, w_1, w_2, d_1, d_2) when their concentration was higher than 3.5 x 10^{13} pfu/ml (Figure 23a-d). When the phage concentrations were below 3.5 x 10^{13} pfu/ml, the NiM structure could not be formed (Figure 23e-f). These data suggest that the formation of NiM only occurred when the phage concentration was above a critical concentration, further indicating that the NiM structure was probably driven by the aforementioned liquid crystal phase formation at the moving meniscus of air-fluid-solid interface when the glass slide was being pulled.

To understand the effect of ionic strengths on the formation of NiM structures, we studied the NiM structure formation under different NaCl concentrations in the phage solution with a certain phage concentration (7 x 10^{13} pfu/ml) and pulling speed (1.5 μm/s). We found that the NaCl concentrations significantly affected the NiM structure formation and generally lower NaCl concentrations benefited the formation of the NiM structures (Figure 24). When NaCl concentrations were higher than 0.01 M, phages could not be assembled into NiM structures, but only formed non-parallel, crossed patterns. When the NaCl concentrations were increased from

0.02 to 0.05 M, the crossed patterns became more disordered. When the NaCl concentrations reached 0.1 M, the phages were assembled into a completely disordered structure. Thus, overall a higher NaCl concentration tended to result in a more disordered phage film.

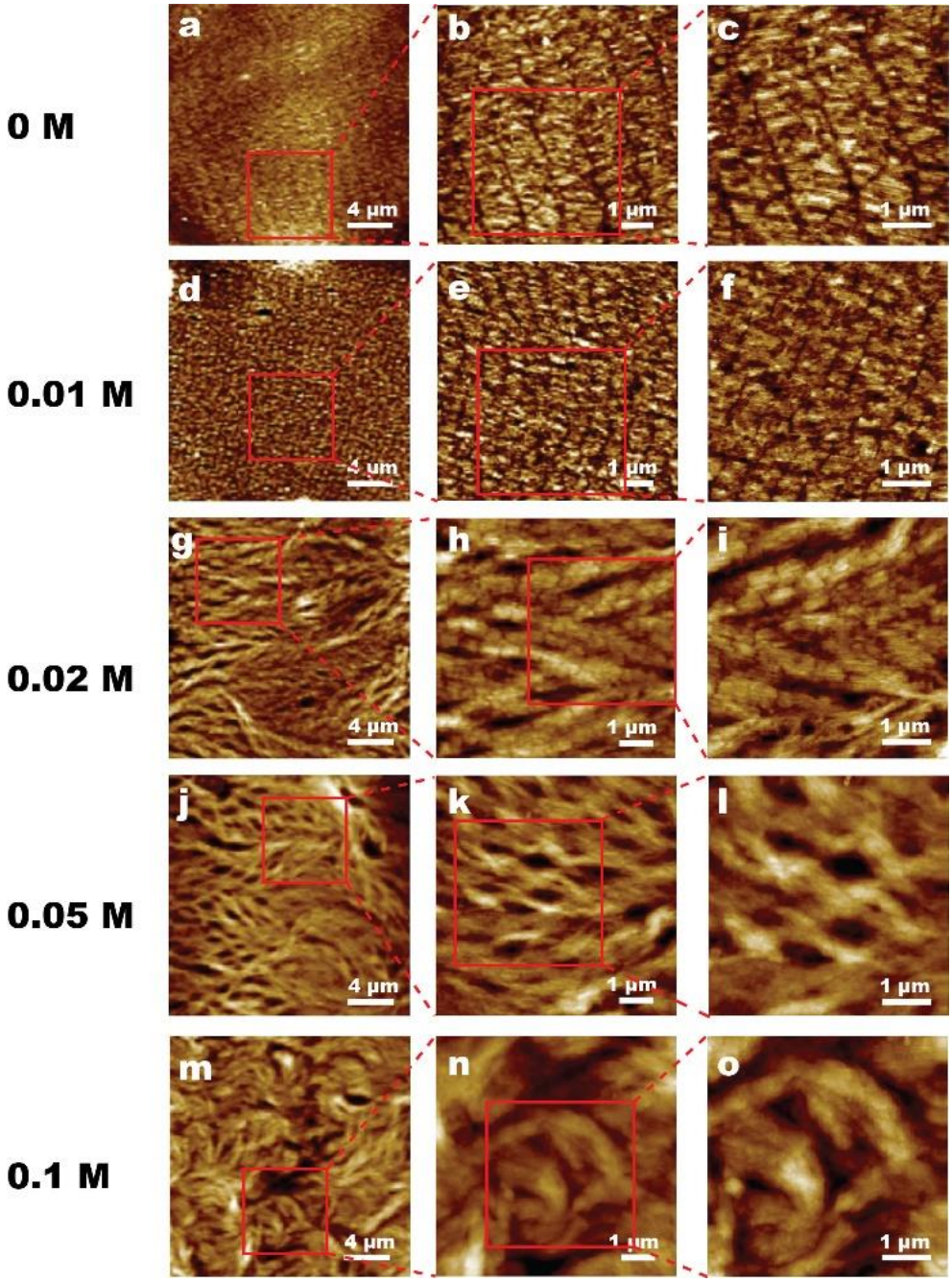

Figure 24. Self-assembly of wild-type phages at different salt (NaCl) concentrations into films by the dip-pulling method. The salt concentrations were found to tremendously influence the structure of the phage assemblies. When the salt concentration was higher than 0.01 M, the phages were

assembled into a cross-linking pattern instead of the parallel-aligned nanoridge pattern. (Phage concentration, 7 x 10^{13} pfu/ml; pulling speed, 1.5 μm/s).

Finally, we investigated the effect of pH values of the phage solutions on the NiM structure formation when the salt concentration was 0.01 M, the phage concentration was 5 x 10^{13} pfu/ml and the pulling speed was 1.5 μm/s. The isoelectric point (pI) of M13 phage is 4.5.[170] The pH of phage solutions was 7-8. Phages could stay in pH 3-11 for 20 min without losing their infectivity.[171] Thus, we studied the effect of pH values when the pH values of the phage solutions were buffered from pH 3 to 11 (Table 4). When the pH value was between 6 to 11, the NiM structures were still formed. When the pH value was higher than 11 or lower than 6, the NiM structures could not be formed (Figure 25a-f).

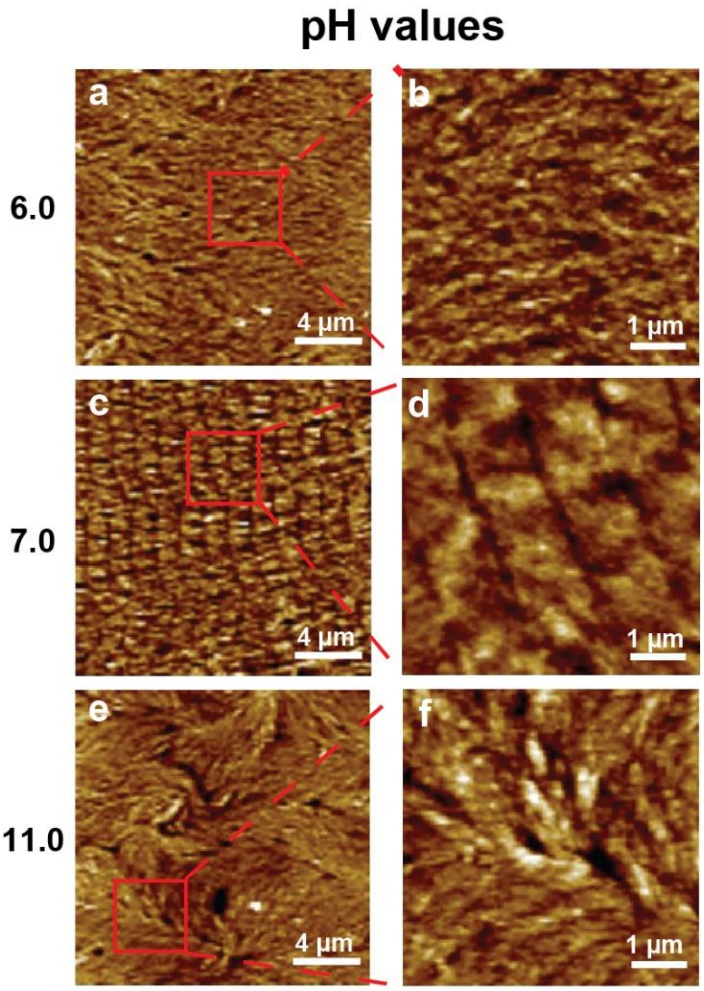

Figure 25. Surface morphologies of wild-type phage films assembled from wild-type phages at different pH values by the dip-pulling method. a–f) pH value of the phage solution manipulates the phage film formation. When the pH was between 6 and 11, the parallel-aligned nanoridged pattern could be seen under the AFM. When the pH was out of this range, such pattern was not formed. (Phage concentration, 5×10^{13} pfu/mL; pulling speed, 1.5 μm/s).

Our method can be extended to the formation of ordered phage structures on a variety of substrates including amorphous materials (e.g., glass and silicon oxide on a silicon wafer), crystalline inorganic materials (e.g., gold, titanium, stainless steel), and organic materials (e.g., polycarbonate plastics) (Figure 26). The key is that these substrates should be pre-treated by being dipped into a polylysine solution to form a polylysine coating. We found that phages could be assembled into NiM structures once these substrates were pre-treated with polylysine. However, such structures were usually not formed on the non-treated substrates (Figure 26). For example, less organized phage structures were formed on the non-treated glass and gold substrates, and phages could not be assembled on the non-coated substrates of titanium, silicon, plastic and stainless steel. Namely, only after the polylysine pre-treatment, could phages be assembled into highly ordered NiM structures on all of substrates with inherently different compositions and crystallinities. It should be noted that surface treatment by only polylysine did not lead to the formation of NiM structures (Figure 27).

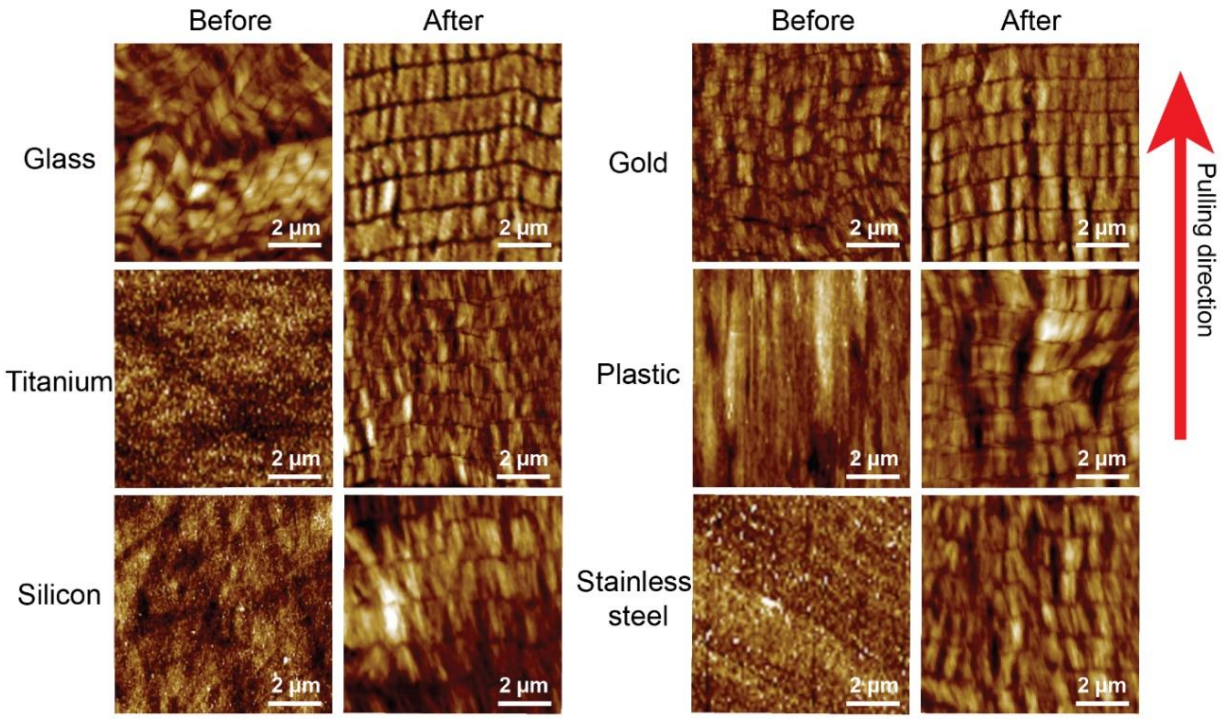

Figure 26. Phage structures on a variety of substrates before and after polylysine treatment. Before polylysine treatment, M13 phages are assembled into nanoridges and nanogrooves on glass and gold substrate with less organized structure, whereas no phage patterns were found on titanium, silicon, plastic, and stainless steel substrate. After the polylysine pretreatment, phages formed highly ordered NiM structures on all of substrates. Red arrow indicated the pulling direction.

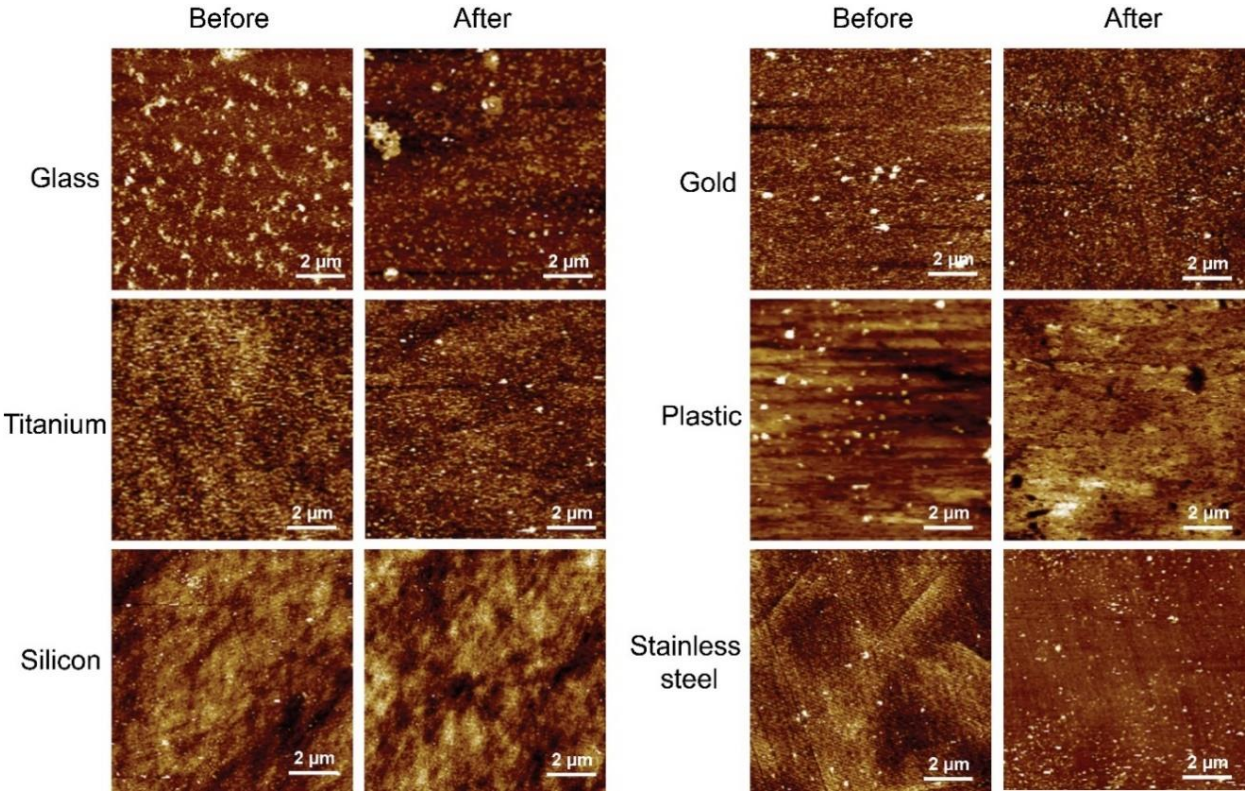

Figure 27. AFM imaging of a variety of substrates before and after polylysine treatment. Different substrates were coated with 0.01% polylysine before the formation of the phage films. None of the pre-treated substrates showed the NiM structure.

3.4.3 Neural differentiation on NiM strucuture

We used the optimized conditions (phage concentration, 1 x 10^{14} pfu/ml; NaCl concentration, 0 M; pH, 7; pulling speed, 1.5 µm/s) to prepare phage films with the NiM structures of WT-phage or RGD-phage. Thus, we had three substrate groups, WT-phage, RGD-phage (Figure 28) and control (the polylysine-coated glass slide without phage), in testing the bidirectional

differentiation of iPSC-derived NPCs into neurons and astrocytes in the absence of differentiation inducers in the culture medium. hiPSC-derived NPCs were seeded on the three substrates in a non-differentiation medium. We observed obvious differences in cell morphology on different substrates. Starting from Day 2 after cell seeding, the cells on the phage films showed an elongated morphology but those on the control substrate were not elongated (Figure 29). The elongated cells on the WT-phage film trended to form clusters without preferential orientation, whereas those on the RGD-phage film, either isolated or clustered, were preferentially aligned along the length direction of microridges (Figure 29b & 30a). Surprisingly, we found that the NiM structures of both WT-phage and RGD-phage could induce the bidirectional differentiation of NPCs into neurons and astrocytes (Figure 30).

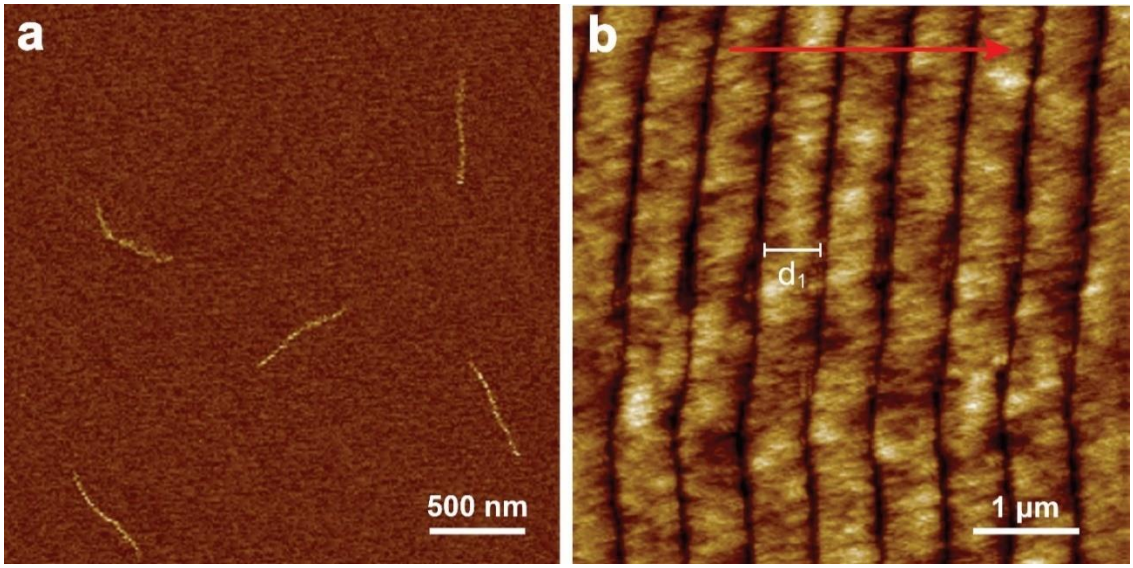

Figure 28. AFM imaging of individual RGD-phage nanofibers and the films assembled from them by the dip-pulling method (Phage concentration, 1 x 10^{14} pfu/ml; pulling speed, 1.5 μm/s.). An RGD-engineered phage is about 550 nm in length. The size d_1 (along the pulling direction, highlighted as a red arrow) of the parallel-aligned nanoridge pattern of the RGD-phage film equals to the length of the RGD-phage.

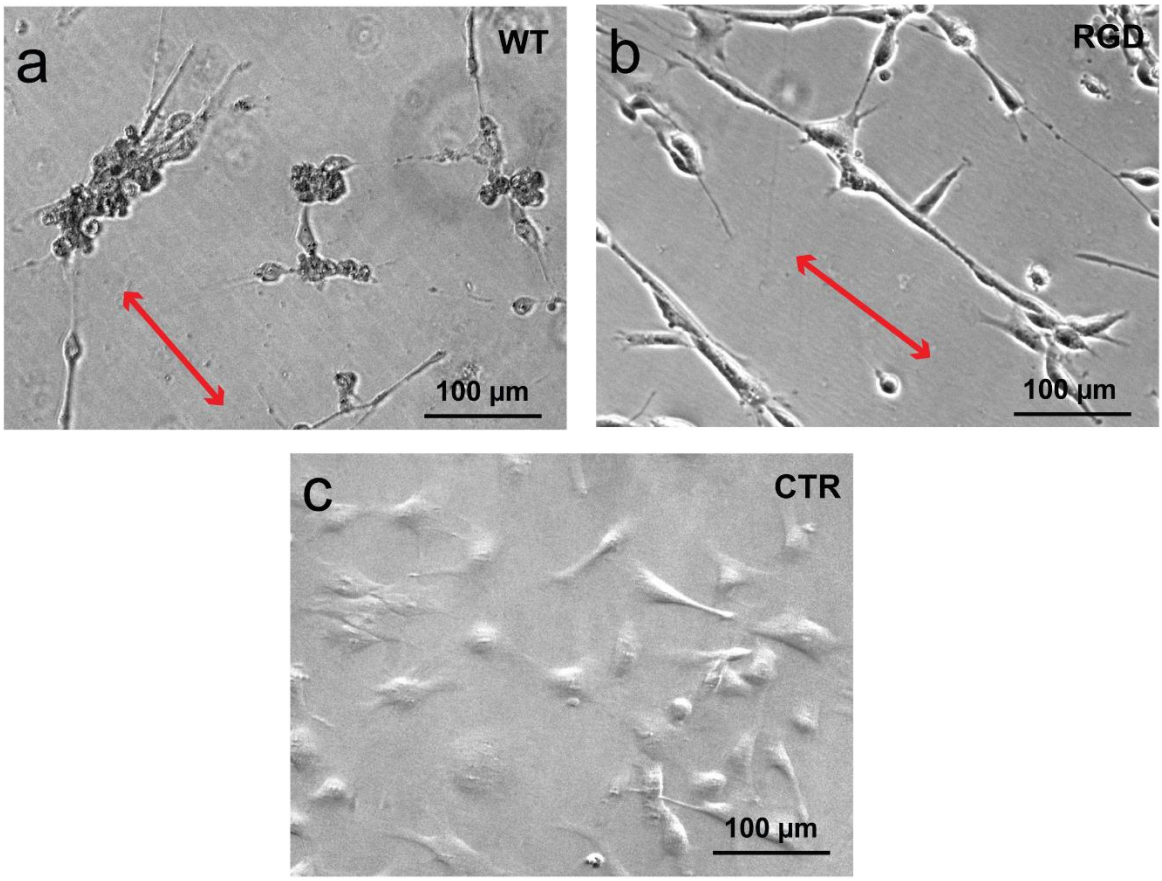

Figure 29. Morphologies of the cells on the different phage substrates formed under the same conditions (Phage concentration, 1 x 10^{14} pfu/ml; pulling speed, 1.5 µm/s.). HiPSC-derived NPCs were seeded onto different substrates, including WT-phage films, RGD-phage films and bare control substrate (CTR, the polylysine-coated glass slides) without phages. Optical images of the cells on different substrates on Day 5. Compared to the control group (c), the cells grew on the phage films (a-b) showed different morphologies on Day 5. The NPCs were grown into clusters on WT phage films (a), but were aligned parallel to the microridge length direction on the RGD-phage films (b). Red arrows denoted the microridge length direction.

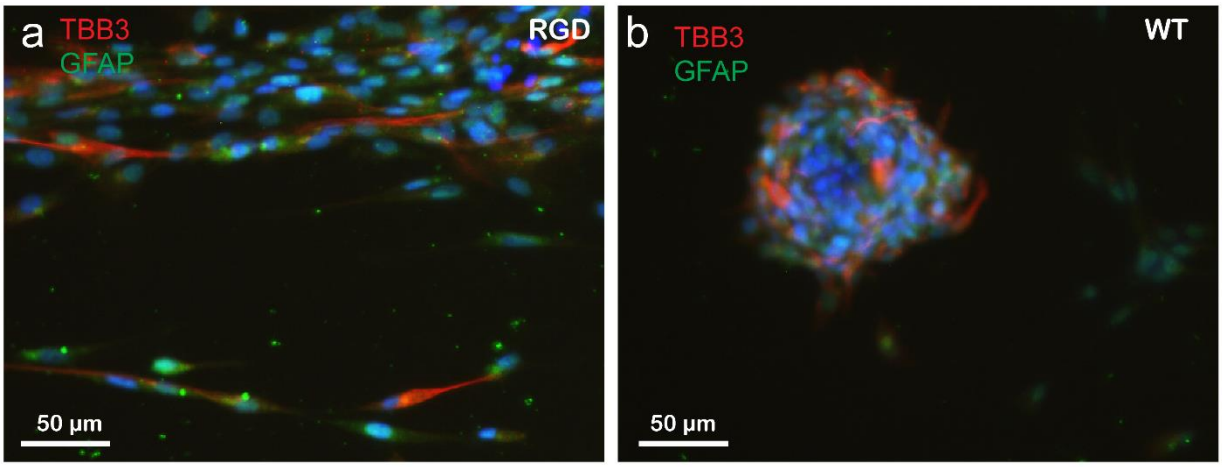

Figure 30. Bidirectional differentiation of the cells on the different phage substrates formed under the same conditions (Phage concentration, 1 x 10^{14} pfu/ml; pulling speed, 1.5 µm/s.). The NPCs on RGD-phage film (a) and WT phage film (b) were bidirectionally differentiated into neurons and astrocytes by phage films only on Day 8. TBB3 is a neuron marker (red) and GFAP is an astrocyte marker (green).

In order to verify that the phage films induced the intended bidirectional differentiation, we tested the possible neural differentiation of NPCs into neurons, astrocytes or oligodendrocytes by detecting their corresponding cellular markers (Figure 30-33). The mRNA and protein expression levels of different markers were tested by RT-qPCR (Figure 31) and immunofluorescence (Figure 32), respectively, on the cells cultured on the phage groups at two time points (Day 4 and 8) (Figure 31-34). It should be noted that Nestin is an NPC marker, βIII-Tubulin (also known as TBB3) and MAP2 are an early and late stage neuron marker, GFAP as astrocyte marker, and Olig2 as an oligodendrocyte marker. The results from the phage film groups

were normalized to those of the control group. We could detect NPC markers for all groups. However, compared to the control group, we could detect a significantly high level of the markers for both neurons and astrocytes, but could not detect the markers for oligodendrocytes, indicating that the phage films could only induce hiPSC-derived NPCs to differentiate into both neurons and astrocytes, but not oligodendrocytes. Moreover, at the two time points, the cells on the WT-phage films showed a higher expression level of the early stage (TBB3) and late stage (MAP2) neuron markers than those on the RGD-phage films at the both mRNA (Figure 31) and protein level (Figure 32-34). On the other hand, at both time points, the cells on the RGD-phage films presented a higher expression level of astrocyte marker (GFAP) than those on the WT-phage films. Therefore, although both WT-phage and RGD-phage films induced the bidirectional differentiation of NPCs into both neurons and astrocytes, the former and latter more favored the differentiation into neurons and astrocytes, respectively (Figure 31-34).

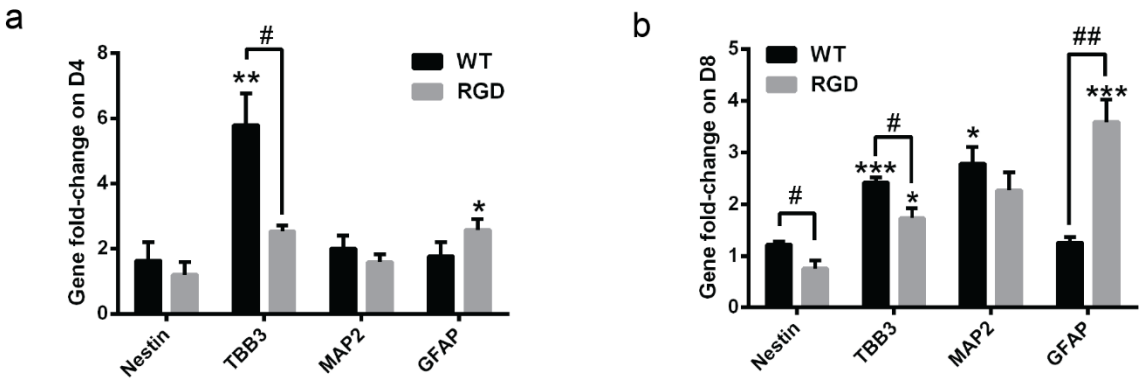

Figure 31. RT-qPCR results on neural differentiation of NPCs on phage films prepared by the dip-pulling method under the same conditions (Phage concentration, 1×10^{14} pfu/mL; pulling speed, 1.5 μm/s.). mRNA expression on markers for NPCs, neurons and astrocytes on: a) Day 4 and b)

Day 8. These results indicate that WT-phage and RGD-phage films more efficiently induced the differentiation of NPCs into neurons and astrocytes, respectively. (* or #, $P < 0.05$; ** or ##, $P < 0.01$; *** or ###, $P < 0.001$; **** or ####, $P < 0.0001$. * indicates the significant difference between WT/RGD and CTR, # indicates the significant difference between WT and RGD).

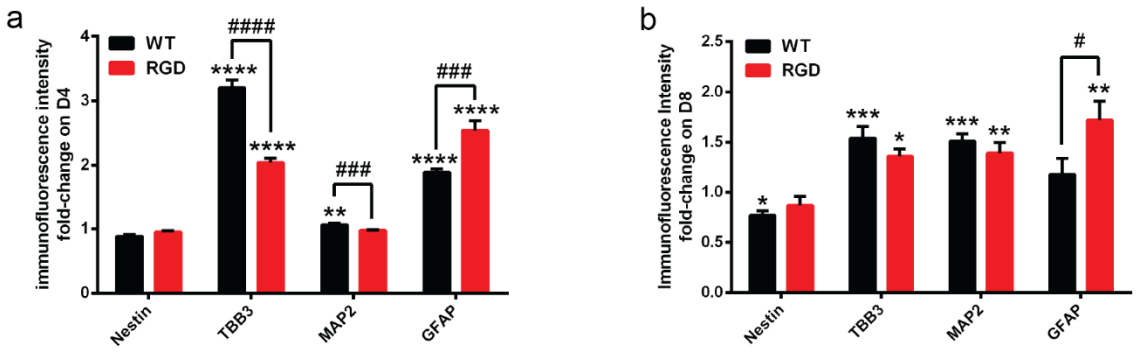

Figure 32. Immunofluorescent intensity fold change on neural differentiation of NPCs on phage films prepared by the dip-pulling method under the same conditions (Phage concentration, 1×10^{14} pfu/mL; pulling speed, 1.5 μm/s.). Protein expression on markers for NPCs, neurons and astrocytes on: a) Day 4 and b) Day 8. Generated by analysis of multiple immunofluorescence images for each marker using image J. The immuno-fluorescent intensity level of each marker in CTR (nonphage control group) were set to 1. The black columns indicate WT/CTR fluorescent intensity ratio and the red columns indicate RGD/CTR fluorescent intensity ratio. These results indicate that WT-phage and RGD-phage films more efficiently induced the differentiation of NPCs into neurons and astrocytes, respectively. (* or #, $P < 0.05$; ** or ##, $P < 0.01$; *** or ###, $P < 0.001$; **** or ####, $P < 0.0001$. * indicates the significant difference between WT/RGD and CTR, # indicates the significant difference between WT and RGD).

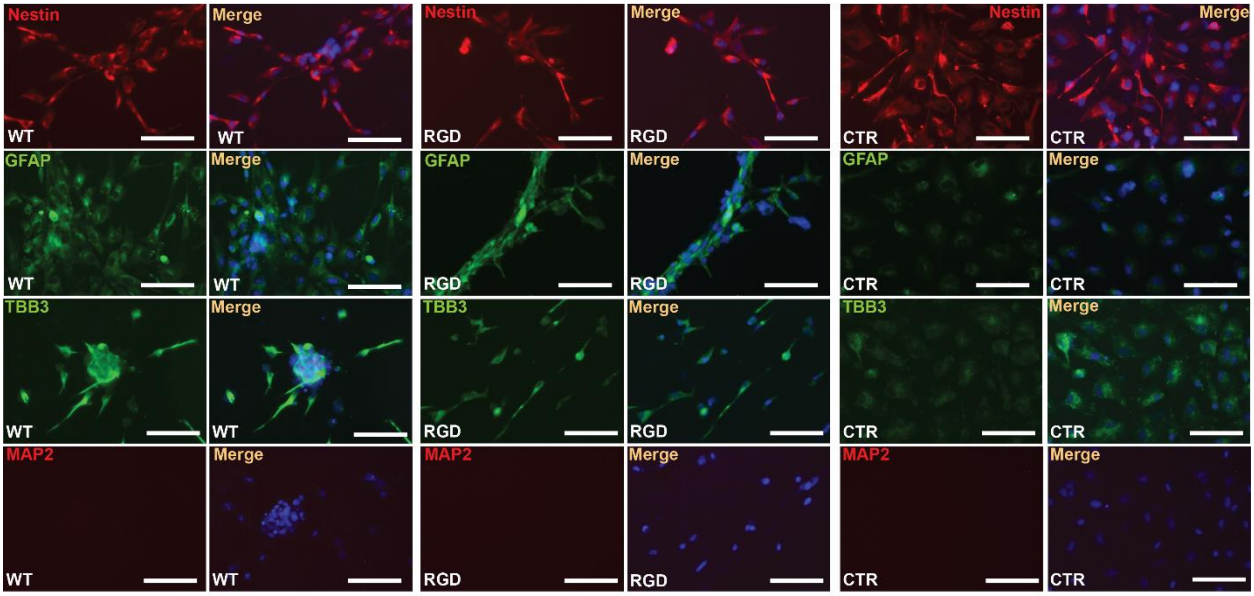

Figure 33. Immunofluorescence imaging results of the markers for the neural differentiation of the NPCs on Day 4. Nestin is an NPC marker. TBB3 and MAP2 are early and late stage neuron markers, respectively. GFAP is an astrocyte marker. The NPCs on the WT-phage films showed higher expression levels of TBB3 and MAP2 marker, while the cells on the RGD-phage films showed a higher expression level of GFAP. Cells on the WT-phage films had a higher expression level of TBB3 marker, while those on the RGD-phage films showed a higher expression level of GFAP marker. Scale bar: 100 μm.

On Day 4, the expression level of the NPC marker (Nestin) was similar in each group, but the expression level of TBB3 and GFAP was significantly increased in both WT-phage and RGD-phage film groups compared to the control group. Compared to the control group, the cells on the WT-phage film expressed a 3.2-fold and 1.9-fold higher fluorescent intensity of TBB3 and GFAP,

respectively, while those on the RGD-phage film showed a 2-fold and 2.5-fold fluorescent intensity increase in TBB3 and GFAP, respectively (Figure 32). On Day 4, the cells on the WT-phage films showed 5-fold higher mRNA expression of TBB3 than the control group (Figure 31 a). These results collectively indicated that the unique phage film structure could induce bidirectional differentiation of hiPSC-derived NPCs within 4 days.

From Day 4 to Day 8, the level of TBB3 expression dropped, but the level of MAP2 expression increased, indicating that the neurons were mature within 8 days (Figure 31 & 32). It usually took more than 2 weeks for NPCs to become mature neurons.[152] However, our phage films achieved the differentiation of NPCs into mature neurons in 8 days, suggesting that our phage films could guide and accelerate the neuron maturation of the hiPSC-derived NPCs due to their unique nanotopographies.

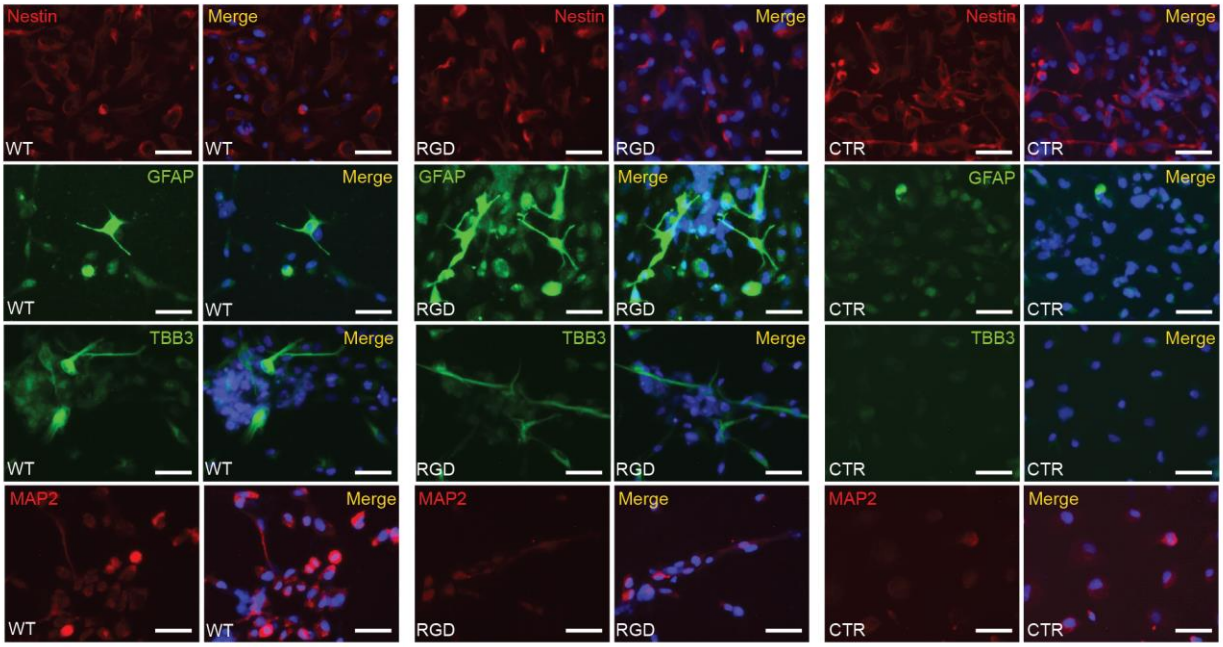

Figure 34. Immunofluorescent images of hiPSC-derived NPCs on different substrates on Day 8. Cells on the WT-phage films had a higher expression level of TBB3 and MAP2 marker, while those on the RGD-phage films showed a higher expression level of GFAP marker. The CTR showed a higher expression level of Nestin marker. Compared to the CTR (without phage) group, the NPCs showed a neural differentiation tendency on the phage films with the WT-phage and RGD-phage film presenting a better induction capability towards neurons and astrocytes, respectively. Scale bar, 50 μm.

Synthetic topography cues greatly influenced the stem cell fate.[51, 54] Anisotropic patterns (such as gratings and grooves) and isotropic patterns (such as pillars and wells) of the substrates were reported to favor neuronal and glial differentiation, respectively.[51, 54] Grating structures were considered to provide stem cells with a stronger support in connecting adjacent cells and promote

the neurite growth and neuronal cell polarization.[55] In comparison to the non-patterned group, gratings were reported to enhance bidirectional differntiation in stem cell culture.[51, 54] The grating size proved to induce neural differentiation ranged from hundreds of nanometers to a few micrometers.[51, 54, 57-59] Thus, we believe that microridges and microgrooves would have a stronger effect on neural differentiation of the hiPSC-derived NPCs than the nanoridges and nanorgrooves in our NiM structures. On the other hand, nanofibers were reported to induce astrocyte differentiation[172] and manipulate the astrocyte activation.[173] Nanofibrous polymers are one of the mostly used materials to induce the bidirectional differentiation.[43, 159, 160] They can be arranged into nanogratings by nano-imprinting[43] or form nanofibers by electrospinning[160]. Our phage films exhibited the topographical features of both anisotropic grating and nanofibers. Hence, such unique topographies induced the bidirectional differentiation of NPCs into neurons and astrocytes without neural differentiation inducers in the culture medium. On the basis of the unique morphology of phages, the peptides displayed on them are the secondary factor that can fine tune the bidirectional differentiation. For instance, in this work we found that both WT-phage and RGD-phage could induce the differentiation of stem cells into both neurons and astrocytes but with a different target cell ratio. Therefore, this work, along with our earlier studies where phages were only assembled into nanoridges, collectively showed that the unique morphology of filamentous phages endowed them to bear the ability to direct stem cell differentiation, although their different self-assembly patterns led to different target cells.[97, 99]

Indeed, we found that in a very short duration (within 8 days) the WT-phage films highly induced the hiPSC-derived NPCs to express neuron markers whereas the RGD-phage films had a

higher induction in astrocyte formation. Generation of neurons through neuronal differentiation from NPCs using neuronal induction media usually need more than 2 weeks.[152, 174] Generation of astrocytes from NPCs or NSCs by using astrocyte induction medium usually needs more than 30 days.[175] Thus, the unique NiM structure of the phage films largely shortened the neural differentiation duration and provided us a way to study the relationship between neurons and astrocytes in tissue regeneration in the future.

In this work, a simple pretreatment of different substrates by polylysine consistently led to the formation of same NiM structures. This suggests that our dip-pulling method is a universal one for the formation of NiM structures on a variety of different substrates. This also further confirms that the electrostatic interaction between phages and the polylysine is one of the driving forces for the assembly of phages into NiM structures on the substrates. Since phages can be used to direct tissue regeneration,[97] template functional materials formation,[176] sense molecules,[103] and build battery materials,[177] the capability of forming NiM phage structures on different materials holds promise in finding versatile applications in many technologically important fields such medicine, energy and electronics.

Although we have not fully understood the mechanism of NiM structure formation, we hypothesize that different experimental parameters affect the structure formation by influencing the liquid crystal behavior of M13 phage at the liquid-air-solid interface. M13 phage becomes highly concentrated to favor liquid crystal formation on the newly exposed solid substrate area that just leaves the liquid phase at the interface during the dip-pulling. The concentration and speed

changes directly affect the critical concentration for liquid crystal formation at the liquid-air-solid interface, and liquid crystal phase change might occur at different critical concentrations.[169] A change in the salt concentration and pH values can alter the surface charge of single phages, which in turn changes the electrostatic interaction in the phage solution.[178] In addition, it is known that electrostatic interaction is the main factor for directing liquid crystal phase transitions[179]. These known influences on the liquid crystal formation by the parameters (concentrations, puling speeds, salt concentration and pH value) shed light into the possible mechanisms by which these parameters control the structure formation of phage films observed in our study and indicate an optimal combination of these parameters leads to the formation of NiM structures.

3.5 Conclusion

In summary, we developed a new dip-pulling method for the assembly of both WT-phage and RGD-phage into a unique unprecedented NiM structure. This method could be extended to the other substrates by a simple polylysine pretreatment before the dip-pulling process. We also identified the best conditions for forming the NiM structure. The key conditions included the pulling speeds, the phage concentrations, the NaCl concentrations, and the pH values. We also found that the resultant NiM structures could induce the bidirectional differentiation of hiPSC-derived NPCs into both neurons and astrocytes in the absence of any differentiation inducer in the culture medium. The NiM structures could induce the bidirectional differentiation within 8 days and thus are significantly faster than the reported methods (more than 2 weeks).[152, 174, 175] When RGD peptide was displayed on the WT-phage to form RGD-phage, the resultant NiM structures

could lead to the formation of more astrocytes in the bidirectional differentiation. Both neurons and astrocytes are building blocks in a healthy CNS. Hence, the neurons and astrocytes generated by our NiM structures can not only be used for treating NDDs but also establish a neuron-astrocyte coculture model for studying their interactions to gain insights for treating NDDs.

Conclusion

In this thesis, we discussed the potential application of hiPSCs in disease treatment and tissue regeneration. We are trying to solve the 2 major questions in hiPSCs derivation and differentiation using bacteriophage-based biomaterials. To improve the efficiency of HDF reprogramming into hiPSCs, we selected an HDF-targeting peptide using a phage display library. This peptide has been proved to bind both outside and inside of the HDFs, which will help with the endocytosis process. To control the differentiation direction of hiPSC-derived NPCs, we used bacteriophage to fabricate a novel 2D nanoridge-in-microridge (NiM) structure. This structure contains grooves and ridges patterns that have been reported to induce the neural differentiation of stem cells, especially have advantages in neuron formation. The hiPSC-derived NPCs were seeded on to this NiM structure and differentiated towards both neurons and astrocytes. With an RGD peptide surface decoration on the NiM structure, we found that the ratio of neurons: astrocytes changed. The RGD NiM structure benefited the astrocyte formation, while non-peptide decorated NiM structure benefited the neuron formation. It's a good model to study the interaction between neurons and astrocytes. We also explore the formation condition of this NiM structure and found that this structure can be applied to multiple materials with a simple polylysine pre-treatment.

In the future, we will continue to study the approaches of cell reprogramming, that can maximize the HDF-targeting peptide function and study the signaling pathway changes in the materials induced neural differentiation.

Reference

1. Gurdon, J. B., The developmental capacity of nuclei taken from intestinal epithelium cells of feeding tadpoles. *J. Embryol. Exp. Morphol.* **1962,** *10,* 622-40.

2. Evans, M. J.; Kaufman, M. H., Establishment in culture of pluripotential cells from mouse embryos. *Nature* **1981,** *292* (5819), 154-6.

3. Martin, G. R., Isolation of a pluripotent cell line from early mouse embryos cultured in medium conditioned by teratocarcinoma stem cells. *Proc. Natl. Acad. Sci. U.S.A.* **1981,** *78* (12), 7634-8.

4. Thomson, J. A.; Itskovitz-Eldor, J.; Shapiro, S. S.; Waknitz, M. A.; Swiergiel, J. J.; Marshall, V. S.; Jones, J. M., Embryonic stem cell lines derived from human blastocysts. *Science* **1998,** *282* (5391), 1145-7.

5. Wilmut, I.; Schnieke, A. E.; McWhir, J.; Kind, A. J.; Campbell, K. H. S., Viable offspring derived from fetal and adult mammalian cells (vol 385, pg 810, 1997). *Nature* **1997,** *386* (6621), 200-200.

6. Schneuwly, S.; Klemenz, R.; Gehring, W. J., Redesigning the Body Plan of Drosophila by Ectopic Expression of the Homeotic Gene Antennapedia. *Nature* **1987,** *325* (6107), 816-818.

7. Davis, R. L.; Weintraub, H.; Lassar, A. B., Expression of a Single Transfected Cdna Converts Fibroblasts to Myoblasts. *Cell* **1987,** *51* (6), 987-1000.

8. Smith, A. G.; Heath, J. K.; Donaldson, D. D.; Wong, G. G.; Moreau, J.; Stahl, M.; Rogers, D., Inhibition of Pluripotential Embryonic Stem-Cell Differentiation by Purified Polypeptides. *Nature* **1988,** *336* (6200), 688-690.

9. Takahashi, K.; Yamanaka, S., Induction of pluripotent stem cells from mouse embryonic and adult fibroblast cultures by defined factors. *Cell* **2006,** *126* (4), 663-76.

10. Takahashi, K.; Tanabe, K.; Ohnuki, M.; Narita, M.; Ichisaka, T.; Tomoda, K.; Yamanaka, S., Induction of pluripotent stem cells from adult human fibroblasts by defined factors. *Cell* **2007,** *131* (5), 861-872.

11. Yamanaka, S., Induced pluripotent stem cells: past, present, and future. *Cell Stem Cell* **2012,** *10* (6), 678-84.

12. Puri, M. C.; Nagy, A., Concise review: Embryonic stem cells versus induced pluripotent stem cells: the game is on. *Stem Cells* **2012,** *30* (1), 10-4.

13. Feng, Q.; Lu, S. J.; Klimanskaya, I.; Gomes, I.; Kim, D.; Chung, Y.; Honig, G. R.; Kim, K. S.; Lanza, R., Hemangioblastic derivatives from human induced pluripotent stem cells exhibit limited expansion and early senescence. *Stem Cells* **2010,** *28* (4), 704-12.

14. Hu, B. Y.; Weick, J. P.; Yu, J.; Ma, L. X.; Zhang, X. Q.; Thomson, J. A.; Zhang, S. C., Neural differentiation of human induced pluripotent stem cells follows developmental principles but with variable potency. *Proc. Natl. Acad. Sci. U.S.A.* **2010,** *107* (9), 4335-40.

15. Hanna, J.; Wernig, M.; Markoulaki, S.; Sun, C. W.; Meissner, A.; Cassady, J. P.; Beard, C.; Brambrink, T.; Wu, L. C.; Townes, T. M.; Jaenisch, R., Treatment of sickle cell anemia mouse model with iPS cells generated from autologous skin. *Science* **2007,** *318* (5858), 1920-3.

16. Stadtfeld, M.; Hochedlinger, K., Induced pluripotency: history, mechanisms, and applications. *Genes Dev.* **2010,** *24* (20), 2239-63.

17. Ross, C. A.; Akimov, S. S., Human-induced pluripotent stem cells: potential for neurodegenerative diseases. *Hum. Mol. Genet.* **2014,** *23* (R1), R17-26.

18. Schlaeger, T. M., Nonintegrating Human Somatic Cell Reprogramming Methods. *Adv. Biochem. Eng. Biotechnol.* **2018,** *163*, 1-21.

19. Pichon, C.; Billiet, L.; Midoux, P., Chemical vectors for gene delivery: uptake and intracellular trafficking. *Curr. Opin. Biotechnol.* **2010,** *21* (5), 640-5.

20. Lundstrom, K.; Boulikas, T., Viral and non-viral vectors in gene therapy: technology development and clinical trials. *Technol. Cancer Res. Treat.* **2003,** *2* (5), 471-86.

21. Hotta, A.; Ellis, J., Retroviral vector silencing during iPS cell induction: an epigenetic beacon that signals distinct pluripotent states. *J. Cell. Biochem.* **2008,** *105* (4), 940-8.

22. Aoi, T.; Yae, K.; Nakagawa, M.; Ichisaka, T.; Okita, K.; Takahashi, K.; Chiba, T.; Yamanaka, S., Generation of pluripotent stem cells from adult mouse liver and stomach cells. *Science* **2008,** *321* (5889), 699-702.

23. Shao, L.; Wu, W. S., Gene-delivery systems for iPS cell generation. *Expert Opin. Biol. Ther.* **2010,** *10* (2), 231-42.

24. Andargie, A.; Tadesse, F.; Shibbiru, T., Review on Cel Reprogramming: Methods and Applications. *Journal of Medicine, Physiology and Biophysycs* **2016,** *25*, 83-91.

25. Cattoglio, C.; Facchini, G.; Sartori, D.; Antonelli, A.; Miccio, A.; Cassani, B.; Schmidt, M.; von Kalle, C.; Howe, S.; Thrasher, A. J.; Aiuti, A.; Ferrari, G.; Recchia, A.; Mavilio, F., Hot spots of retroviral integration in human CD34+ hematopoietic cells. *Blood* **2007,** *110* (6), 1770-8.

26. Papapetrou, E. P.; Tomishima, M. J.; Chambers, S. M.; Mica, Y.; Reed, E.; Menon, J.; Tabar, V.; Mo, Q.; Studer, L.; Sadelain, M., Stoichiometric and temporal requirements of Oct4, Sox2, Klf4, and c-Myc expression for efficient human iPSC induction and differentiation. *Proc. Natl. Acad. Sci. U.S.A.* **2009,** *106* (31), 12759-64.

27. Wold, W. S.; Toth, K., Adenovirus vectors for gene therapy, vaccination and cancer gene therapy. *Curr. Gene Ther.* **2013,** *13* (6), 421-33.

28. Morodomi, Y.; Inoue, M.; Hasegawa, M.; Okamoto, T.; Maehara, Y.; Yonemitsu, Y., Sendai Virus-Based Oncolytic Gene Therapy. In *Novel Gene Therapy Approaches*, Wei, M.; Good, D., Eds. InTech: 2013; pp 183-194.

29. Masaki, I.; Yonemitsu, Y.; Komori, K.; Ueno, H.; Nakashima, Y.; Nakagawa, K.; Fukumura, M.; Kato, A.; Hasan, M. K.; Nagai, Y.; Sugimachi, K.; Hasegawa, M.; Sueishi, K., Recombinant Sendai virus-mediated gene transfer to vasculature: a new class of efficient gene transfer vector to the vascular system. *FASEB J.* **2001,** *15* (7), 1294-6.

30. Nishimura, K.; Sano, M.; Ohtaka, M.; Furuta, B.; Umemura, Y.; Nakajima, Y.; Ikehara, Y.; Kobayashi, T.; Segawa, H.; Takayasu, S.; Sato, H.; Motomura, K.; Uchida, E.; Kanayasu-Toyoda, T.; Asashima, M.; Nakauchi, H.; Yamaguchi, T.; Nakanishi, M., Development of defective and persistent Sendai virus vector: a unique gene delivery/expression system ideal for cell reprogramming. *J. Biol. Chem.* **2011,** *286* (6), 4760-71.

31. Long, J.; Kim, H.; Kim, D.; Lee, J. B.; Kim, D. H., A biomaterial approach to cell reprogramming and differentiation. *J Mater Chem B* **2017,** *5* (13), 2375-2379.

32. Lee, W. S.; Kim, Y. K.; Zhang, Q.; Park, T. E.; Kang, S. K.; Kim, D. W.; Cho, C. S.; Choi, Y. J., Polyxylitol-based gene carrier improves the efficiency of gene transfer through enhanced endosomal osmolysis. *Nanomed.* **2014,** *10* (3), 525-34.

33. Zhang, R.; Zheng, N.; Song, Z.; Yin, L.; Cheng, J., The effect of side-chain functionality and hydrophobicity on the gene delivery capabilities of cationic helical polypeptides. *Biomaterials* **2014,** *35* (10), 3443-54.

34. Wu, P.; Chen, H.; Jin, R.; Weng, T.; Ho, J. K.; You, C.; Zhang, L.; Wang, X.; Han, C., Non-viral gene delivery systems for tissue repair and regeneration. *J. Transl. Med.* **2018,** *16* (1), 29.

35. Yates, J.; Warren, N.; Reisman, D.; Sugden, B., A cis-acting element from the Epstein-Barr viral genome that permits stable replication of recombinant plasmids in latently infected cells. *Proc. Natl. Acad. Sci. U.S.A.* **1984,** *81* (12), 3806-10.

36. Yu, J.; Hu, K.; Smuga-Otto, K.; Tian, S.; Stewart, R.; Slukvin, II; Thomson, J. A., Human induced pluripotent stem cells free of vector and transgene sequences. *Science* **2009,** *324* (5928), 797-801.

37. Warren, L.; Manos, P. D.; Ahfeldt, T.; Loh, Y. H.; Li, H.; Lau, F.; Ebina, W.; Mandal, P. K.; Smith, Z. D.; Meissner, A.; Daley, G. Q.; Brack, A. S.; Collins, J. J.; Cowan, C.; Schlaeger, T. M.; Rossi, D. J., Highly efficient reprogramming to pluripotency and directed differentiation of human cells with synthetic modified mRNA. *Cell Stem Cell* **2010,** *7* (5), 618-30.

38. Schlaeger, T. M.; Daheron, L.; Brickler, T. R.; Entwisle, S.; Chan, K.; Cianci, A.; DeVine, A.; Ettenger, A.; Fitzgerald, K.; Godfrey, M.; Gupta, D.; McPherson, J.; Malwadkar, P.; Gupta, M.; Bell, B.; Doi, A.; Jung, N.; Li, X.; Lynes, M. S.; Brookes, E.; Cherry, A. B.; Demirbas, D.; Tsankov, A. M.; Zon, L. I.; Rubin, L. L.; Feinberg, A. P.; Meissner, A.; Cowan, C. A.; Daley, G. Q., A comparison of non-integrating reprogramming methods. *Nat. Biotechnol.* **2015,** *33* (1), 58-63.

39. Malik, N.; Rao, M. S., A review of the methods for human iPSC derivation. *Methods Mol. Biol.* **2013,** *997*, 23-33.

40. Abagnale, G.; Sechi, A.; Steger, M.; Zhou, Q.; Kuo, C. C.; Aydin, G.; Schalla, C.; Muller-Newen, G.; Zenke, M.; Costa, I. G.; van Rijn, P.; Gillner, A.; Wagner, W., Surface Topography Guides Morphology and Spatial Patterning of Induced Pluripotent Stem Cell Colonies. *Stem Cell Reports* **2017,** *9* (2), 654-666.

41. Zhang, X. Q.; Zhang, S. C., Differentiation of neural precursors and dopaminergic neurons from human embryonic stem cells. *Methods Mol. Biol.* **2010,** *584*, 355-66.

42. Pimpin, A. a. S., W, Review on Micro- and Nanolithography Techniques and their Applications. *Eng. J.* **2012,** *16* (1), 37-56.

43. Moe, A. A.; Suryana, M.; Marcy, G.; Lim, S. K.; Ankam, S.; Goh, J. Z.; Jin, J.; Teo, B. K.; Law, J. B.; Low, H. Y.; Goh, E. L.; Sheetz, M. P.; Yim, E. K., Microarray with micro- and nano-topographies enables identification of the optimal topography for directing the differentiation of primary murine neural progenitor cells. *Small* **2012,** *8* (19), 3050-61.

44. Kolind, K.; Leong, K. W.; Besenbacher, F.; Foss, M., Guidance of stem cell fate on 2D patterned surfaces. *Biomaterials* **2012,** *33* (28), 6626-33.

45. Rajnicek, A.; Britland, S.; McCaig, C., Contact guidance of CNS neurites on grooved quartz: influence of groove dimensions, neuronal age and cell type. *J. Cell Sci.* **1997,** *110 (Pt 23)*, 2905-13.

46. Johansson, F.; Carlberg, P.; Danielsen, N.; Montelius, L.; Kanje, M., Axonal outgrowth on nano-imprinted patterns. *Biomaterials* **2006,** *27* (8), 1251-8.

47. Mahoney, M. J.; Chen, R. R.; Tan, J.; Saltzman, W. M., The influence of microchannels on neurite growth and architecture. *Biomaterials* **2005,** *26* (7), 771-8.

48. Yang, T. C.; Chuang, J. H.; Buddhakosai, W.; Wu, W. J.; Lee, C. J.; Chen, W. S.; Yang, Y. P.; Li, M. C.; Peng, C. H.; Chen, S. J., Elongation of Axon Extension for Human iPSC-Derived Retinal Ganglion Cells by a Nano-Imprinted Scaffold. *Int. J. Mol. Sci.* **2017,** *18* (9).

49. Mattotti, M.; Alvarez, Z.; Ortega, J. A.; Planell, J. A.; Engel, E.; Alcantara, S., Inducing functional radial glia-like progenitors from cortical astrocyte cultures using micropatterned PMMA. *Biomaterials* **2012,** *33* (6), 1759-1770.

50. Recknor, J. B.; Sakaguchi, D. S.; Mallapragada, S. K., Directed growth and selective differentiation of neural progenitor cells on micropatterned polymer substrates. *Biomaterials* **2006,** *27* (22), 4098-108.

51. Ankam, S.; Suryana, M.; Chan, L. Y.; Moe, A. A.; Teo, B. K.; Law, J. B.; Sheetz, M. P.; Low, H. Y.; Yim, E. K., Substrate topography and size determine the fate of human embryonic stem cells to neuronal or glial lineage. *Acta Biomater.* **2013,** *9* (1), 4535-45.

52. Yim, E. K.; Ankam, S.; Moe, A.; Chan, L. In *Effect of spatial arrangement of substrate topography on neuronal differentiation of stem cells*, The 15th International Conference on Biomedical Engineering, Springer: 2014; pp 60-63.

53. Tan, K. K. B.; Tann, J. Y.; Sathe, S. R.; Goh, S. H.; Ma, D. L.; Goh, E. L. K.; Yim, E. K. F., Enhanced differentiation of neural progenitor cells into neurons of the mesencephalic dopaminergic subtype on topographical patterns. *Biomaterials* **2015,** *43*, 32-43.

54. Yang, K.; Jung, K.; Ko, E.; Kim, J.; Park, K. I.; Kim, J.; Cho, S. W., Nanotopographical manipulation of focal adhesion formation for enhanced differentiation of human neural stem cells. *ACS Appl. Mater. Interfaces* **2013,** *5* (21), 10529-40.

55. Song, L.; Wang, K.; Li, Y.; Yang, Y., Nanotopography promoted neuronal differentiation of human induced pluripotent stem cells. *Colloids Surf. B. Biointerfaces* **2016,** *148*, 49-58.

56. Yang, K.; Jung, H.; Lee, H. R.; Lee, J. S.; Kim, S. R.; Song, K. Y.; Cheong, E.; Bang, J.; Im, S. G.; Cho, S. W., Multiscale, Hierarchically Patterned Topography for Directing Human Neural Stem Cells into Functional Neurons. *ACS Nano* **2014,** *8* (8), 7809-7822.

57. Pan, F.; Zhang, M.; Wu, G. M.; Lai, Y. K.; Greber, B.; Scholer, H. R.; Chi, L. F., Topographic effect on human induced pluripotent stem cells differentiation towards neuronal lineage. *Biomaterials* **2013,** *34* (33), 8131-8139.

58. Chan, L. Y.; Birch, W. R.; Yim, E. K.; Choo, A. B., Temporal application of topography to increase the rate of neural differentiation from human pluripotent stem cells. *Biomaterials* **2013,** *34* (2), 382-92.

59. Lee, M. R.; Kwon, K. W.; Jung, H.; Kim, H. N.; Suh, K. Y.; Kim, K.; Kim, K. S., Direct differentiation of human embryonic stem cells into selective neurons on nanoscale ridge/groove pattern arrays. *Biomaterials* **2010,** *31* (15), 4360-4366.

60. Hwang, Y. S.; Chung, B. G.; Ortmann, D.; Hattori, N.; Moeller, H. C.; Khademhosseini, A., Microwell-mediated control of embryoid body size regulates embryonic stem cell fate via differential expression of WNT5a and WNT11. *Proc. Natl. Acad. Sci. U.S.A.* **2009,** *106* (40), 16978-83.

61. Chen, W.; Villa-Diaz, L. G.; Sun, Y.; Weng, S.; Kim, J. K.; Lam, R. H.; Han, L.; Fan, R.; Krebsbach, P. H.; Fu, J., Nanotopography influences adhesion, spreading, and self-renewal of human embryonic stem cells. *ACS Nano* **2012,** *6* (5), 4094-103.

62. Lyu, Z. L.; Wang, H. W.; Wang, Y. Y.; Ding, K. G.; Liu, H.; Yuan, L.; Shi, X. J.; Wang, M. M.; Wang, Y. W.; Chen, H., Maintaining the pluripotency of mouse embryonic stem cells on gold nanoparticle layers with nanoscale but not microscale surface roughness. *Nanoscale* **2014,** *6* (12), 6959-6969.

63. Chen, W.; Han, S.; Qian, W.; Weng, S.; Yang, H.; Sun, Y.; Villa-Diaz, L. G.; Krebsbach, P. H.; Fu, J., Nanotopography regulates motor neuron differentiation of human pluripotent stem cells. *Nanoscale* **2018,** *10* (7), 3556-3565.

64. Varelas, X.; Sakuma, R.; Samavarchi-Tehrani, P.; Peerani, R.; Rao, B. M.; Dembowy, J.; Yaffe, M. B.; Zandstra, P. W.; Wrana, J. L., TAZ controls Smad nucleocytoplasmic shuttling and regulates human embryonic stem-cell self-renewal. *Nat. Cell Biol.* **2008,** *10* (7), 837-48.

65. Chua, J. S.; Chng, C. P.; Moe, A. A.; Tann, J. Y.; Goh, E. L.; Chiam, K. H.; Yim, E. K., Extending neurites sense the depth of the underlying topography during neuronal differentiation and contact guidance. *Biomaterials* **2014,** *35* (27), 7750-61.

66. Migliorini, E.; Grenci, G.; Ban, J.; Pozzato, A.; Tormen, M.; Lazzarino, M.; Torre, V.; Ruaro, M. E., Acceleration of neuronal precursors differentiation induced by substrate nanotopography. *Biotechnol. Bioeng.* **2011,** *108* (11), 2736-46.

67. Engler, A. J.; Sen, S.; Sweeney, H. L.; Discher, D. E., Matrix elasticity directs stem cell lineage specification. *Cell* **2006,** *126* (4), 677-89.

68. Evans, N. D.; Minelli, C.; Gentleman, E.; LaPointe, V.; Patankar, S. N.; Kallivretaki, M.; Chen, X.; Roberts, C. J.; Stevens, M. M., Substrate stiffness affects early differentiation events in embryonic stem cells. *Eur. Cell. Mater.* **2009,** *18*, 1-13; discussion 13-4.

69. Yang, C.; Tibbitt, M. W.; Basta, L.; Anseth, K. S., Mechanical memory and dosing influence stem cell fate. *Nat. Mater.* **2014,** *13* (6), 645-52.

70. Engler, A. J.; Griffin, M. A.; Sen, S.; Bonnemann, C. G.; Sweeney, H. L.; Discher, D. E., Myotubes differentiate optimally on substrates with tissue-like stiffness: pathological implications for soft or stiff microenvironments. *J. Cell Biol.* **2004,** *166* (6), 877-87.

71. Georges, P. C.; Miller, W. J.; Meaney, D. F.; Sawyer, E. S.; Janmey, P. A., Matrices with compliance comparable to that of brain tissue select neuronal over glial growth in mixed cortical cultures. *Biophys. J.* **2006,** *90* (8), 3012-3018.

72. Previtera, M. L.; Langhammer, C. G.; Firestein, B. L., Effects of substrate stiffness and cell density on primary hippocampal cultures. *J. Biosci. Bioeng.* **2010,** *110* (4), 459-70.

73. Ali, S.; Wall, I. B.; Mason, C.; Pelling, A. E.; Veraitch, F. S., The effect of Young's modulus on the neuronal differentiation of mouse embryonic stem cells. *Acta Biomater.* **2015,** *25*, 253-267.

74. Maldonado, M.; Luu, R. J.; Ico, G.; Ospina, A.; Myung, D.; Shih, H. P.; Nam, J., Lineage- and developmental stage-specific mechanomodulation of induced pluripotent stem cell differentiation. *Stem Cell. Res. Ther.* **2017,** *8* (1), 216.

75. Zhang, Q. Y.; Zhang, Y. Y.; Xie, J.; Li, C. X.; Chen, W. Y.; Liu, B. L.; Wu, X. A.; Li, S. N.; Huo, B.; Jiang, L. H.; Zhao, H. C., Stiff substrates enhance cultured neuronal network activity. *Sci Rep* **2014,** *4*, 6215.

76. Leipzig, N. D.; Shoichet, M. S., The effect of substrate stiffness on adult neural stem cell behavior. *Biomaterials* **2009,** *30* (36), 6867-78.

77. Ma, Q.; Yang, L.; Jiang, Z.; Song, Q.; Xiao, M.; Zhang, D.; Ma, X.; Wen, T.; Cheng, G., Three-Dimensional Stiff Graphene Scaffold on Neural Stem Cells Behavior. *ACS Appl. Mater. Interfaces* **2016,** *8* (50), 34227-34233.

78. Musah, S.; Wrighton, P. J.; Zaltsman, Y.; Zhong, X. F.; Zorn, S.; Parlato, M. B.; Hsiao, C.; Palecek, S. P.; Chang, Q.; Murphy, W. L.; Kiessling, L. L., Substratum-induced differentiation of human pluripotent stem cells reveals the coactivator YAP is a potent regulator of neuronal specification. *Proc. Natl. Acad. Sci. U.S.A.* **2014,** *111* (38), 13805-13810.

79. Musah, S.; Morin, S. A.; Wrighton, P. J.; Zwick, D. B.; Jin, S.; Kiessling, L. L., Glycosaminoglycan-binding hydrogels enable mechanical control of human pluripotent stem cell self-renewal. *ACS Nano* **2012,** *6* (11), 10168-77.

80. Qi, L.; Li, N.; Huang, R.; Song, Q.; Wang, L.; Zhang, Q.; Su, R.; Kong, T.; Tang, M.; Cheng, G., The effects of topographical patterns and sizes on neural stem cell behavior. *PLoS One* **2013,** *8* (3), e59022.

81. Yang, K.; Park, E.; Lee, J. S.; Kim, I. S.; Hong, K.; Park, K. I.; Cho, S. W.; Yang, H. S., Biodegradable Nanotopography Combined with Neurotrophic Signals Enhances Contact Guidance and Neuronal Differentiation of Human Neural Stem Cells. *Macromol. Biosci.* **2015,** *15* (10), 1348-56.

82. Li, Z.; Wang, W.; Kratz, K.; Kuchler, J.; Xu, X.; Zou, J.; Deng, Z.; Sun, X.; Gossen, M.; Ma, N.; Lendlein, A., Influence of surface roughness on neural differentiation of human induced pluripotent stem cells. *Clin. Hemorheol. Microcirc.* **2016,** *64* (3), 355-366.

83. Smeal, S. W.; Schmitt, M. A.; Pereira, R. R.; Prasad, A.; Fisk, J. D., Simulation of the M13 life cycle I: Assembly of a genetically-structured deterministic chemical kinetic simulation. *Virology* **2017,** *500*, 259-274.

84. Krag, D. N.; Shukla, G. S.; Shen, G. P.; Pero, S.; Ashikaga, T.; Fuller, S.; Weaver, D. L.; Burdette-Radoux, S.; Thomas, C., Selection of tumor-binding ligands in cancer patients with phage display libraries. *Cancer Res.* **2006,** *66* (15), 7724-33.

85. Smith, G. P.; Petrenko, V. A., Phage Display. *Chem. Rev.* **1997,** *97* (2), 391-410.

86. Moon, J. S.; Kim, W. G.; Kim, C.; Park, G. T.; Heo, J.; Yoo, S. Y.; Oh, J. W., M13 Bacteriophage-Based Self-Assembly Structures and Their Functional Capabilities. *Mini-Rev. Org. Chem.* **2015,** *12* (3), 271-281.

87. Smith, G. P., Filamentous Fusion Phage - Novel Expression Vectors That Display Cloned Antigens on the Virion Surface. *Science* **1985,** *228* (4705), 1315-1317.

88. Gao, C.; Mao, S.; Kaufmann, G.; Wirsching, P.; Lerner, R. A.; Janda, K. D., A method for the generation of combinatorial antibody libraries using pIX phage display. *Proc. Natl. Acad. Sci. U.S.A.* **2002,** *99* (20), 12612-6.

89. Nam, K. T.; Wartena, R.; Yoo, P. J.; Liau, F. W.; Lee, Y. J.; Chiang, Y. M.; Hammond, P. T.; Belcher, A. M., Stamped microbattery electrodes based on self-assembled M13 viruses. *Proc. Natl. Acad. Sci. U.S.A.* **2008,** *105* (45), 17227-31.

90. Huang, W.; Petrosino, J.; Palzkill, T., Display of functional beta-lactamase inhibitory protein on the surface of M13 bacteriophage. *Antimicrob. Agents Chemother.* **1998,** *42* (11), 2893-7.

91. Lee, S. K.; Yun, D. S.; Belcher, A. M., Cobalt ion mediated self-assembly of genetically engineered bacteriophage for biomimetic Co-Pt hybrid material. *Biomacromolecules* **2006,** *7* (1), 14-7.

92. Hufton, S. E.; Moerkerk, P. T.; Meulemans, E. V.; de Bruine, A.; Arends, J. W.; Hoogenboom, H. R., Phage display of cDNA repertoires: the pVI display system and its applications for the selection of immunogenic ligands. *J. Immunol. Methods* **1999,** *231* (1-2), 39-51.

93. Qi, H.; Lu, H. Q.; Qiu, H. J.; Petrenko, V.; Liu, A. H., Phagemid Vectors for Phage Display: Properties, Characteristics and Construction. *J. Mol. Biol.* **2012,** *417* (3), 129-143.

94. Bazan, J.; Calkosinski, I.; Gamian, A., Phage display-A powerful technique for immunotherapy 2. Vaccine delivery. *Hum. Vacc. Immunother.* **2012,** *8* (12), 1829-1835.

95. Wu, C. H.; Liu, I. J.; Lu, R. M.; Wu, H. C., Advancement and applications of peptide phage display technology in biomedical science. *J. Biomed. Sci.* **2016,** *23*, 8.

96. Cao, B. R.; Yang, M. Y.; Mao, C. B., Phage as a Genetically Modifiable Supramacromolecule in Chemistry, Materials and Medicine. *Acc. Chem. Res.* **2016,** *49* (6), 1111-1120.

97. Wang, J.; Wang, L.; Yang, M.; Zhu, Y.; Tomsia, A.; Mao, C., Untangling the effects of peptide sequences and nanotopographies in a biomimetic niche for directed differentiation of iPSCs by assemblies of genetically engineered viral nanofibers. *Nano Lett.* **2014,** *14* (12), 6850-6.

98. Zhou, N. Y.; Li, Y.; Loveland, C. H.; Wilson, M. J.; Cao, B. R.; Qiu, P. H.; Yang, M. Y.; Mao, C. B., Hierarchical Ordered Assembly of Genetically Modifiable Viruses into Nanoridge-in-Microridge Structures. *Adv. Mater.* **2019**, DOI: 10.1002/adma.201905577.

99. Wang, J.; Wang, L.; Li, X.; Mao, C., Virus activated artificial ECM induces the osteoblastic differentiation of mesenchymal stem cells without osteogenic supplements. *Sci Rep* **2013,** *3*, 1242.

100. Cao, B.; Xu, H.; Mao, C., Transmission electron microscopy as a tool to image bioinorganic nanohybrids: the case of phage-gold nanocomposites. *Microsc. Res. Tech.* **2011,** *74* (7), 627-35.

101. Mao, C.; Wang, F.; Cao, B., Controlling nanostructures of mesoporous silica fibers by supramolecular assembly of genetically modifiable bacteriophages. *Angew. Chem. Int. Ed. Engl.* **2012,** *51* (26), 6411-5.

102. Xu, H.; Cao, B.; George, A.; Mao, C., Self-assembly and mineralization of genetically modifiable biological nanofibers driven by beta-structure formation. *Biomacromolecules* **2011,** *12* (6), 2193-9.

103. Wang, Y.; Ju, Z.; Cao, B.; Gao, X.; Zhu, Y.; Qiu, P.; Xu, H.; Pan, P.; Bao, H.; Wang, L.; Mao, C., Ultrasensitive rapid detection of human serum antibody biomarkers by biomarker-capturing viral nanofibers. *ACS Nano* **2015,** *9* (4), 4475-4483.

104. Ngweniform, P.; Abbineni, G.; Cao, B.; Mao, C., Self-assembly of drug-loaded liposomes on genetically engineered target-recognizing M13 phage: a novel nanocarrier for targeted drug delivery. *Small* **2009,** *5* (17), 1963-9.

105. Watson, L. M.; Wong, M. M.; Becker, E. B., Induced pluripotent stem cell technology for modelling and therapy of cerebellar ataxia. *Open biology* **2015,** *5* (7), 150056.

106. Bilic, J.; Izpisua Belmonte, J. C., Concise review: Induced pluripotent stem cells versus embryonic stem cells: close enough or yet too far apart? *Stem Cells* **2012,** *30* (1), 33-41.

107. Narsinh, K. H.; Plews, J.; Wu, J. C., Comparison of human induced pluripotent and embryonic stem cells: fraternal or identical twins? *Mol. Ther.* **2011,** *19* (4), 635-8.

108. Lu, X.; Zhao, T., Clinical therapy using iPSCs: hopes and challenges. *Genomics Proteomics Bioinformatics* **2013,** *11* (5), 294-8.

109. Ebert, A. D.; Yu, J.; Rose, F. F., Jr.; Mattis, V. B.; Lorson, C. L.; Thomson, J. A.; Svendsen, C. N., Induced pluripotent stem cells from a spinal muscular atrophy patient. *Nature* **2009,** *457* (7227), 277-80.

110. Liu, G. H.; Barkho, B. Z.; Ruiz, S.; Diep, D.; Qu, J.; Yang, S. L.; Panopoulos, A. D.; Suzuki, K.; Kurian, L.; Walsh, C.; Thompson, J.; Boue, S.; Fung, H. L.; Sancho-Martinez, I.; Zhang, K.; Yates, J., 3rd; Izpisua Belmonte, J. C., Recapitulation of premature ageing with iPSCs from Hutchinson-Gilford progeria syndrome. *Nature* **2011,** *472* (7342), 221-5.

111. Schwartz, R. E.; Trehan, K.; Andrus, L.; Sheahan, T. P.; Ploss, A.; Duncan, S. A.; Rice, C. M.; Bhatia, S. N., Modeling hepatitis C virus infection using human induced pluripotent stem cells. *Proc. Natl. Acad. Sci. U.S.A.* **2012,** *109* (7), 2544-8.

112. Trounson, A.; Shepard, K. A.; DeWitt, N. D., Human disease modeling with induced pluripotent stem cells. *Curr. Opin. Genet. Dev.* **2012,** *22* (5), 509-16.

113. Wu, S. M.; Hochedlinger, K., Harnessing the potential of induced pluripotent stem cells for regenerative medicine. *Nat. Cell Biol.* **2011,** *13* (5), 497-505.

114. Tiscornia, G.; Vivas, E. L.; Izpisua Belmonte, J. C., Diseases in a dish: modeling human genetic disorders using induced pluripotent cells. *Nat. Med.* **2011,** *17* (12), 1570-6.

115. Liu, G. H.; Qu, J.; Suzuki, K.; Nivet, E.; Li, M.; Montserrat, N.; Yi, F.; Xu, X.; Ruiz, S.; Zhang, W.; Wagner, U.; Kim, A.; Ren, B.; Li, Y.; Goebl, A.; Kim, J.; Soligalla, R. D.; Dubova, I.; Thompson, J.; Yates, J., 3rd; Esteban, C. R.; Sancho-Martinez, I.; Izpisua Belmonte, J. C., Progressive degeneration of human neural stem cells caused by pathogenic LRRK2. *Nature* **2012,** *491* (7425), 603-7.

116. Moretti, A.; Bellin, M.; Welling, A.; Jung, C. B.; Lam, J. T.; Bott-Flugel, L.; Dorn, T.; Goedel, A.; Hohnke, C.; Hofmann, F.; Seyfarth, M.; Sinnecker, D.; Schomig, A.; Laugwitz, K. L., Patient-specific induced pluripotent stem-cell models for long-QT syndrome. *N. Engl. J. Med.* **2010,** *363* (15), 1397-409.

117. Okano, H.; Nakamura, M.; Yoshida, K.; Okada, Y.; Tsuji, O.; Nori, S.; Ikeda, E.; Yamanaka, S.; Miura, K., Steps toward safe cell therapy using induced pluripotent stem cells. *Circ. Res.* **2013,** *112* (3), 523-33.

118. Wang, L.; Cao, J.; Wang, Y.; Lan, T.; Liu, L.; Wang, W.; Jin, N.; Gong, J.; Zhang, C.; Teng, F.; Yan, G.; Li, C.; Li, J.; Wan, H.; Hu, B.; Li, W.; Zhao, X.; Qi, Z.; Zhao, T.; Zhou, Q., Immunogenicity and functional evaluation of iPSC-derived organs for transplantation. **2015,** *1*, 15015.

119. Sourisseau, M.; Goldman, O.; He, W.; Gori, J. L.; Kiem, H. P.; Gouon-Evans, V.; Evans, M. J., Hepatic cells derived from induced pluripotent stem cells of pigtail macaques support hepatitis C virus infection. *Gastroenterology* **2013,** *145* (5), 966-969 e7.

120. Schwartz, S. D.; Hubschman, J. P.; Heilwell, G.; Franco-Cardenas, V.; Pan, C. K.; Ostrick, R. M.; Mickunas, E.; Gay, R.; Klimanskaya, I.; Lanza, R., Embryonic stem cell trials for macular degeneration: a preliminary report. *Lancet* **2012,** *379* (9817), 713-20.

121. Schmidt, R.; Plath, K., The roles of the reprogramming factors Oct4, Sox2 and Klf4 in resetting the somatic cell epigenome during induced pluripotent stem cell generation. *Genome Biol.* **2012,** *13* (10), 251.

122. Sanges, D.; Cosma, M. P., Reprogramming cell fate to pluripotency: the decision-making signalling pathways. *Int. J. Dev. Biol.* **2010,** *54* (11-12), 1575-87.

123. Masui, S.; Nakatake, Y.; Toyooka, Y.; Shimosato, D.; Yagi, R.; Takahashi, K.; Okochi, H.; Okuda, A.; Matoba, R.; Sharov, A. A.; Ko, M. S.; Niwa, H., Pluripotency governed by Sox2 via regulation of Oct3/4 expression in mouse embryonic stem cells. *Nat. Cell Biol.* **2007,** *9* (6), 625-35.

124. Hawkins, K.; Joy, S.; McKay, T., Cell signalling pathways underlying induced pluripotent stem cell reprogramming. *World J. Stem Cells* **2014,** *6* (5), 620-8.

125. Miyoshi, N.; Ishii, H.; Nagano, H.; Haraguchi, N.; Dewi, D. L.; Kano, Y.; Nishikawa, S.; Tanemura, M.; Mimori, K.; Tanaka, F.; Saito, T.; Nishimura, J.; Takemasa, I.; Mizushima, T.; Ikeda, M.; Yamamoto, H.; Sekimoto, M.; Doki, Y.; Mori, M., Reprogramming of mouse and human cells to pluripotency using mature microRNAs. *Cell Stem Cell* **2011,** *8* (6), 633-8.

126. Lin, T.; Wu, S., Reprogramming with Small Molecules instead of Exogenous Transcription Factors. *Stem Cells Int.* **2015,** *2015*, 794632.

127. Somers, A.; Jean, J. C.; Sommer, C. A.; Omari, A.; Ford, C. C.; Mills, J. A.; Ying, L.; Sommer, A. G.; Jean, J. M.; Smith, B. W., Generation of transgene-free lung disease-specific human induced pluripotent stem cells using a single excisable lentiviral stem cell cassette. *Stem Cells* **2010,** *28* (10), 1728-1740.

128. Park, I. H.; Zhao, R.; West, J. A.; Yabuuchi, A.; Huo, H. G.; Ince, T. A.; Lerou, P. H.; Lensch, M. W.; Daley, G. Q., Reprogramming of human somatic cells to pluripotency with defined factors. *Nature* **2008,** *451* (7175), 141-U1.

129. Mali, P.; Yang, L.; Esvelt, K. M.; Aach, J.; Guell, M.; DiCarlo, J. E.; Norville, J. E.; Church, G. M., RNA-guided human genome engineering via Cas9. *Science* **2013,** *339* (6121), 823-6.

130. Ran, F. A.; Hsu, P. D.; Wright, J.; Agarwala, V.; Scott, D. A.; Zhang, F., Genome engineering using the CRISPR-Cas9 system. *Nat. Protoc.* **2013,** *8* (11), 2281-308.

131. Li, L.; He, Z. Y.; Wei, X. W.; Gao, G. P.; Wei, Y. Q., Challenges in CRISPR/CAS9 Delivery: Potential Roles of Nonviral Vectors. *Hum. Gene Ther.* **2015,** *26* (7), 452-62.

132. Park, H. Y.; Noh, E. H.; Chung, H. M.; Kang, M. J.; Kim, E. Y.; Park, S. P., Efficient generation of virus-free iPS cells using liposomal magnetofection. *PLoS One* **2012,** *7* (9), e45812.

133. Ma, K.; Wang, D. D.; Lin, Y. Y.; Wang, J. L.; Petrenko, V.; Mao, C. B., Synergetic Targeted Delivery of Sleeping-Beauty Transposon System to Mesenchymal Stem Cells Using LPD Nanoparticles Modified with a Phage-Displayed Targeting Peptide. *Adv. Funct. Mater.* **2013,** *23* (9), 1172-1181.

134. Wang, D. D.; Yang, M.; Zhu, Y.; Mao, C., Reiterated Targeting Peptides on the Nanoparticle Surface Significantly Promote Targeted Vascular Endothelial Growth Factor Gene Delivery to Stem Cells. *Biomacromolecules* **2015,** *16* (12), 3897-903.

135. Michon, I. N.; Hauer, A. D.; von der Thusen, J. H.; Molenaar, T. J.; van Berkel, T. J.; Biessen, E. A.; Kuiper, J., Targeting of peptides to restenotic vascular smooth muscle cells using phage display in vitro and in vivo. *Biochim. Biophys. Acta* **2002,** *1591* (1-3), 87-97.

136. McGuire, M. J.; Li, S.; Brown, K. C., Biopanning of phage displayed peptide libraries for the isolation of cell-specific ligands. *Methods Mol. Biol.* **2009,** *504*, 291-321.

137. Oyama, T.; Sykes, K. F.; Samli, K. N.; Minna, J. D.; Johnston, S. A.; Brown, K. C., Isolation of lung tumor specific peptides from a random peptide library: generation of diagnostic and cell-targeting reagents. *Cancer Lett.* **2003,** *202* (2), 219-230.

138. Yoo, M. K.; Kang, S. K.; Choi, J. H.; Park, I. K.; Na, H. S.; Lee, H. C.; Kim, E. B.; Lee, N. K.; Nah, J. W.; Choi, Y. J.; Cho, C. S., Targeted delivery of chitosan nanoparticles to Peyer's patch using M cell-homing peptide selected by phage display technique. *Biomaterials* **2010,** *31* (30), 7738-47.

139. Elayadi, A. N.; Samli, K. N.; Prudkin, L.; Liu, Y. H.; Bian, A.; Xie, X. J.; Wistuba, II; Roth, J. A.; McGuire, M. J.; Brown, K. C., A peptide selected by biopanning identifies the integrin alphavbeta6 as a prognostic biomarker for nonsmall cell lung cancer. *Cancer Res.* **2007,** *67* (12), 5889-95.

140. Mandava, S.; Makowski, L.; Devarapalli, S.; Uzubell, J.; Rodi, D. J., RELIC - A bioinformatics server for combinatorial peptide analysis and identification of protein-ligand interaction sites. *Proteomics* **2004,** *4* (5), 1439-1460.

141. Tracy, L. E.; Minasian, R. A.; Caterson, E. J., Extracellular Matrix and Dermal Fibroblast Function in the Healing Wound. *Adv Wound Care (New Rochelle)* **2016,** *5* (3), 119-136.

142. Bershadsky, A. D.; Vaisberg, E. A.; Vasiliev, J. M., Pseudopodial Activity at the Active Edge of Migrating Fibroblast Is Decreased after Drug-Induced Microtubule Depolymerization. *Cell Motil. Cytoskelet.* **1991,** *19* (3), 152-158.

143. Yao, H. B.; Fang, H. Y.; Wang, X. H.; Yu, S. H., Hierarchical assembly of micro-/nano-building blocks: bio-inspired rigid structural functional materials. *Chem. Soc. Rev.* **2011,** *40* (7), 3764-85.

144. Maragakis, N. J.; Rothstein, J. D., Mechanisms of Disease: astrocytes in neurodegenerative disease. *Nat. Clin. Pract. Neurol.* **2006,** *2* (12), 679-89.

145. Johnson, M. A.; Weick, J. P.; Pearce, R. A.; Zhang, S. C., Functional neural development from human embryonic stem cells: accelerated synaptic activity via astrocyte coculture. *J. Neurosci.* **2007,** *27* (12), 3069-77.

146. Allen, N. J.; Eroglu, C., Cell Biology of Astrocyte-Synapse Interactions. *Neuron* **2017,** *96* (3), 697-708.

147. Allaman, I.; Gavillet, M.; Belanger, M.; Laroche, T.; Viertl, D.; Lashuel, H. A.; Magistretti, P. J., Amyloid-beta aggregates cause alterations of astrocytic metabolic phenotype: impact on neuronal viability. *J. Neurosci.* **2010,** *30* (9), 3326-38.

148. Nazari, S.; Faez, K.; Amiri, M.; Karami, E., A digital implementation of neuron-astrocyte interaction for neuromorphic applications. *Neural Netw.* **2015,** *66*, 79-90.

149. Blumenthal, N. R.; Hermanson, O.; Heimrich, B.; Shastri, V. P., Stochastic nanoroughness modulates neuron-astrocyte interactions and function via mechanosensing cation channels. *Proc. Natl. Acad. Sci. U.S.A.* **2014,** *111* (45), 16124-9.

150. Chapman, C. A. R.; Chen, H.; Stamou, M.; Biener, J.; Biener, M. M.; Lein, P. J.; Seker, E., Nanoporous Gold as a Neural Interface Coating: Effects of Topography, Surface Chemistry, and Feature Size. *ACS Appl. Mater. Interfaces* **2015,** *7* (13), 7093-7100.

151. Kuijlaars, J.; Oyelami, T.; Diels, A.; Rohrbacher, J.; Versweyveld, S.; Meneghello, G.; Tuefferd, M.; Verstraelen, P.; Detrez, J. R.; Verschuuren, M.; De Vos, W. H.; Meert, T.; Peeters, P. J.; Cik, M.; Nuydens, R.; Brone, B.; Verheyen, A., Sustained synchronized neuronal network activity in a human astrocyte co-culture system. *Sci Rep* **2016,** *6*, 36529.

152. Gunhanlar, N.; Shpak, G.; Van Der Kroeg, M.; Gouty-Colomer, L.; Munshi, S. T.; Lendemeijer, B.; Ghazvini, M.; Dupont, C.; Hoogendijk, W.; Gribnau, J., A simplified protocol

for differentiation of electrophysiologically mature neuronal networks from human induced pluripotent stem cells. *Mol. Psychiatry* **2017**.

153. Weissman, I. L., Translating stem and progenitor cell biology to the clinic: barriers and opportunities. *Science* **2000,** *287* (5457), 1442-6.

154. Lindvall, O.; Kokaia, Z., Stem cells in human neurodegenerative disorders--time for clinical translation? *J. Clin. Invest.* **2010,** *120* (1), 29-40.

155. Uchida, N.; Buck, D. W.; He, D.; Reitsma, M. J.; Masek, M.; Phan, T. V.; Tsukamoto, A. S.; Gage, F. H.; Weissman, I. L., Direct isolation of human central nervous system stem cells. *Proc. Natl. Acad. Sci. U.S.A.* **2000,** *97* (26), 14720-5.

156. Li, Y.; Liu, M.; Yan, Y.; Yang, S. T., Neural differentiation from pluripotent stem cells: The role of natural and synthetic extracellular matrix. *World J. Stem Cells* **2014,** *6* (1), 11-23.

157. Sun, Y.; Yong, K. M.; Villa-Diaz, L. G.; Zhang, X.; Chen, W.; Philson, R.; Weng, S.; Xu, H.; Krebsbach, P. H.; Fu, J., Hippo/YAP-mediated rigidity-dependent motor neuron differentiation of human pluripotent stem cells. *Nat. Mater.* **2014,** *13* (6), 599-604.

158. Julia, T. C. W.; Wang, M. H.; Pimenova, A. A.; Bowles, K. R.; Hartley, B. J.; Lacin, E.; Machlovi, S. I.; Abdelaal, R.; Karch, C. M.; Phatnani, H.; Slesinger, P. A.; Zhang, B.; Goate, A. M.; Brennand, K. J., An Efficient Platform for Astrocyte Differentiation from Human Induced Pluripotent Stem Cells. *Stem Cell Reports* **2017,** *9* (2), 600-614.

159. Que, R. A.; Arulmoli, J.; Da Silva, N. A.; Flanagan, L. A.; Wang, S. W., Recombinant collagen scaffolds as substrates for human neural stem/progenitor cells. *J. Biomed. Mater. Res. A* **2018,** *106* (5), 1363-1372.

160. Lin, C. K.; Liu, C.; Zhang, L. M.; Huang, Z.; Zhao, P. P.; Chen, R. Q.; Pang, M.; Chen, Z. X.; He, L. M.; Luo, C. X.; Rong, L. M.; Liu, B., Interaction of iPSC-derived neural stem cells on poly(L-lactic acid) nanofibrous scaffolds for possible use in neural tissue engineering. *Int. J. Mol. Med.* **2018,** *41* (2), 697-708.

161. Xu, C.; Inokuma, M. S.; Denham, J.; Golds, K.; Kundu, P.; Gold, J. D.; Carpenter, M. K., Feeder-free growth of undifferentiated human embryonic stem cells. *Nat. Biotechnol.* **2001,** *19* (10), 971-974.

162. Cao, B. R.; Yang, M. Y.; Mao, C. B., Phage as a Genetically Modifiable Supramacromolecule in Chemistry, Materials and Medicine. *Acc. Chem. Res.* **2016,** *49* (6), 1111-1120.

163. Mao, C.; Flynn, C. E.; Hayhurst, A.; Sweeney, R.; Qi, J.; Georgiou, G.; Iverson, B.; Belcher, A. M., Viral assembly of oriented quantum dot nanowires. *Proc. Natl. Acad. Sci. U.S.A.* **2003,** *100* (12), 6946-51.

164. Rong, J.; Lee, L. A.; Li, K.; Harp, B.; Mello, C. M.; Niu, Z.; Wang, Q., Oriented cell growth on self-assembled bacteriophage M13 thin films. *Chem. Commun.* **2008,** (41), 5185-7.

165. Chung, W. J.; Oh, J. W.; Kwak, K.; Lee, B. Y.; Meyer, J.; Wang, E.; Hexemer, A.; Lee, S. W., Biomimetic self-templating supramolecular structures. *Nature* **2011,** *478* (7369), 364-368.

166. Seuring, C.; Ayyer, K.; Filippaki, E.; Barthelmess, M.; Longchamp, J. N.; Ringler, P.; Pardini, T.; Wojtas, D. H.; Coleman, M. A.; Dorner, K.; Fuglerud, S.; Hammarin, G.; Habenstein, B.; Langkilde, A. E.; Loquet, A.; Meents, A.; Riek, R.; Stahlberg, H.; Boutet, S.; Hunter, M. S.; Koglin, J.; Liang, M.; Ginn, H. M.; Millane, R. P.; Frank, M.; Barty, A.; Chapman, H. N., Femtosecond X-ray coherent diffraction of aligned amyloid fibrils on low background graphene. *Nat. Commun.* **2018,** *9* (1), 1836.

167. Yang, G.; Li, X. L.; He, Y.; Ma, J. K.; Ni, G. L.; Zhou, S. B., From nano to micro to macro: Electrospun hierarchically structured polymeric fibers for biomedical applications. *Prog. Polym. Sci.* **2018,** *81*, 80-113.

168. He, C.; Ye, T.; Teng, W.; Fang, Z.; Ruan, W. S.; Liu, G.; Chen, H.; Sun, J.; Hui, L.; Sheng, F.; Pan, D.; Yang, C.; Zheng, Y.; Luo, M. B.; Yao, K.; Wang, B., Bioinspired Shear-Flow-Driven Layer-by-Layer in Situ Self-Assembly. *ACS Nano* **2019,** *13* (2), 1910-1922.

169. Dogic, Z.; Fraden, S., Ordered phases of filamentous viruses. *Curr. Opin. Colloid Interface Sci.* **2006,** *11* (1), 47-55.

170. Branston, S.; Stanley, E.; Keshavarz-Moore, E.; Ward, J., Precipitation of filamentous bacteriophages for their selective recovery in primary purification. *Biotechnol. Prog.* **2012,** *28* (1), 129-136.

171. Branston, S. D.; Stanley, E. C.; Ward, J. M.; Keshavarz-Moore, E., Determination of the survival of bacteriophage M13 from chemical and physical challenges to assist in its sustainable bioprocessing. *Biotechnol. Bioprocess Eng.* **2013,** *18* (3), 560-566.

172. Patel, B. B.; Sharifi, F.; Stroud, D. P.; Montazami, R.; Hashemi, N. N.; Sakaguchi, D. S., 3D Microfibrous Scaffolds Selectively Promotes Proliferation and Glial Differentiation of Adult Neural Stem Cells: A Platform to Tune Cellular Behavior in Neural Tissue Engineering. *Macromol. Biosci.* **2019,** *19* (2), 1800236.

173. Tiryaki, V. M.; Ayres, V. M.; Ahmed, I.; Shreiber, D. I., Differentiation of reactive-like astrocytes cultured on nanofibrillar and comparative culture surfaces. *Nanomed.* **2015,** *10* (4), 529-45.

174. Li, X. J.; Du, Z. W.; Zarnowska, E. D.; Pankratz, M.; Hansen, L. O.; Pearce, R. A.; Zhang, S. C., Specification of motoneurons from human embryonic stem cells. *Nat. Biotechnol.* **2005,** *23* (2), 215-21.

175. Shaltouki, A.; Peng, J.; Liu, Q.; Rao, M. S.; Zeng, X., Efficient generation of astrocytes from human pluripotent stem cells in defined conditions. *Stem Cells* **2013,** *31* (5), 941-52.

176. Mao, C.; Solis, D. J.; Reiss, B. D.; Kottmann, S. T.; Sweeney, R. Y.; Hayhurst, A.; Georgiou, G.; Iverson, B.; Belcher, A. M., Virus-based toolkit for the directed synthesis of magnetic and semiconducting nanowires. *Science* **2004,** *303* (5655), 213-7.

177. Nam, K. T.; Kim, D. W.; Yoo, P. J.; Chiang, C. Y.; Meethong, N.; Hammond, P. T.; Chiang, Y. M.; Belcher, A. M., Virus-enabled synthesis and assembly of nanowires for lithium ion battery electrodes. *Science* **2006,** *312* (5775), 885-8.

178. Dogic, Z.; Fraden, S., Smectic phase in a colloidal suspension of semiflexible virus particles. *Phys. Rev. Lett.* **1997,** *78* (12), 2417-2420.

179. Purdy, K. R.; Fraden, S., Influence of charge and flexibility on smectic phase formation in filamentous virus suspensions. *Phys. Rev. E Stat. Nonlin. Soft Matter Phys.* **2007,** *76* (1), 011705.

Appendix: List of Copyrights and Permissions

ELSEVIER LICENSE
TERMS AND CONDITIONS
Mar 20, 2020

This Agreement between University of Oklahoma -- Ningyun Zhou ("You") and Elsevier ("Elsevier") consists of your license details and the terms and conditions provided by Elsevier and Copyright Clearance Center.

License Number	4793371435719
License date	Mar 20, 2020
Licensed Content Publisher	Elsevier
Licensed Content Publication	Cell Stem Cell
Licensed Content Title	Induced Pluripotent Stem Cells: Past, Present, and Future
Licensed Content Author	Shinya Yamanaka
Licensed Content Date	Jun 14, 2012
Licensed Content Volume	10
Licensed Content Issue	6
Licensed Content Pages	7
Start Page	678
End Page	684
Type of Use	reuse in a thesis/dissertation
Portion	figures/tables/illustrations
Number of figures/tables/illustrations	2
Format	electronic
Are you the author of this Elsevier article?	No
Will you be translating?	No

Title	Graduate student
Institution name	University of Oklahoma
Expected presentation date	Apr 2020
Portions	Figure 1, figure2
Requestor Location	University of Oklahoma 101 Stephenson Parkway NORMAN, OK 73019 United States Attn: University of Oklahoma
Publisher Tax ID	98-0397604

JOHN WILEY AND SONS LICENSE TERMS AND CONDITIONS

Mar 21, 2020

This Agreement between University of Oklahoma -- Ningyun Zhou ("You") and John Wiley and Sons ("John Wiley and Sons") consists of your license details and the terms and conditions provided by John Wiley and Sons and Copyright Clearance Center.

License Number	4793440541073
License date	Mar 21, 2020
Licensed Content Publisher	John Wiley and Sons
Licensed Content Publication	Small
Licensed Content Title	Microarray with Micro- and Nano-topographies Enables Identification of the Optimal Topography for Directing the Differentiation of Primary Murine Neural Progenitor Cells
Licensed Content Author	Evelyn K. F. Yim, Michael P. Sheetz, Eyleen L. K. Goh, et al
Licensed Content Date	Jul 16, 2012
Licensed Content Volume	8
Licensed Content Issue	19
Licensed Content Pages	12
Type of use	Dissertation/Thesis
Requestor type	University/Academic
Format	Electronic
Portion	Figure/table
Number of figures/tables	1

Original Wiley figure/table number(s)	Figure 2
Will you be translating?	No
Title of your thesis / dissertation	Graduate student
Expected completion date	Apr 2020
Expected size (number of pages)	1
Requestor Location	University of Oklahoma 101 Stephenson Parkway NORMAN, OK 73019 United States Attn: University of Oklahoma
Publisher Tax ID	EU826007151

JOHN WILEY AND SONS LICENSE TERMS AND CONDITIONS

Mar 21, 2020

This Agreement between University of Oklahoma -- Ningyun Zhou ("You") and John Wiley and Sons ("John Wiley and Sons") consists of your license details and the terms and conditions provided by John Wiley and Sons and Copyright Clearance Center.

License Number	4793440702765
License date	Mar 21, 2020
Licensed Content Publisher	John Wiley and Sons
Licensed Content Publication	Advanced Materials
Licensed Content Title	Hierarchical Ordered Assembly of Genetically Modifiable Viruses into Nanoridge-in-Microridge Structures
Licensed Content Author	Chuanbin Mao, Mingying Yang, Penghe Qiu, et al
Licensed Content Date	Nov 18, 2019
Licensed Content Volume	31
Licensed Content Issue	52
Licensed Content Pages	9
Type of use	Dissertation/Thesis
Requestor type	Author of this Wiley article
Format	Electronic
Portion	Full article
Will you be translating?	No
Title of your thesis / dissertation	Graduate student
Expected completion date	Apr 2020
Expected size (number of pages)	1

Requestor Location	University of Oklahoma 101 Stephenson Parkway NORMAN, OK 73019 United States Attn: University of Oklahoma
Publisher Tax ID	EU826007151

Phage as a Genetically Modifiable Supramacromolecule in Chemistry, Materials and Medicine

Author: Binrui Cao, Mingying Yang, Chuanbin Mao
Publication: Accounts of Chemical Research
Publisher: American Chemical Society
Date: Jun 1, 2016

PERMISSION/LICENSE IS GRANTED FOR YOUR ORDER AT NO CHARGE

This type of permission/license, instead of the standard Terms & Conditions, is sent to you because no fee is being charged for your order. Please note the following:

- Permission is granted for your request in both print and electronic formats, and translations.
- If figures and/or tables were requested, they may be adapted or used in part.
- Please print this page for your records and send a copy of it to your publisher/graduate school.
- Appropriate credit for the requested material should be given as follows: "Reprinted (adapted) with permission from (COMPLETE REFERENCE CITATION). Copyright (YEAR) American Chemical Society." Insert appropriate information in place of the capitalized words.
- One-time permission is granted only for the use specified in your request. No additional uses are granted (such as derivative works or other editions). For any other uses, please submit a new request.

If credit is given to another source for the material you requested, permission must be obtained from that source.